



GNSS Based Attitude Determination for Small Unmanned Aerial Vehicles

A thesis submitted for the degree of
Doctor of Philosophy
in
Mechanical Engineering

March 2011

Author:

James T Pinchin

Supervisors:

Prof. XiaoQi Chen

Dr. David Park

'If you want truly to understand something, try to change it.'

Kurt Lewin, 1890-1947

ABSTRACT

This thesis is concerned with determining the orientation of small Unmanned Aerial Vehicles (UAVs). To make commercial use of these aircraft in aerial surveying markets their attitude needs to be determined accurately and precisely throughout a survey flight.

Traditionally inertial sensors have been used on larger aircraft to estimate both position and orientation in combination with Global Navigation Satellite Systems (GNSS). High quality inertial sensors have many downsides when used on the small UAV. They are expensive, power hungry and often heavy. Inertial sensors are vulnerable to vibration, high acceleration, high rotation rate and jerk. All of these are present on the small UAV. This thesis identifies GNSS attitude determination as a potentially suitable alternative to inertial techniques.

Carrier phase GNSS attitude determination uses three or more GNSS receivers with antennas separated by a short baseline to estimate the orientation of the UAV. This technique offers low cost, high accuracy and drift-free attitude estimates. To be successfully used it requires removal of the biases present in the received GNSS signals and estimation of the integer cycle ambiguity present in the carrier phase measurement.

This thesis presents and examines the state of the art techniques for removing these biases and estimating an integer cycle ambiguity using *a priori* measurement of the inter-antenna distance. In this work a novel method is developed which uses this *a priori* baseline measurement to validate estimates of the carrier phase ambiguities.

In order to test these methods data has been gathered using low cost, commercially available GNSS receivers and antennas. This is the first work in which modern, low cost, GNSS equipment has been tested for use in attitude determination. It is found that the state of the art carrier phase GNSS attitude determination methods can provide an accurate attitude estimate for every set of measurements from the GNSS receivers.

However, a real UAV flight indicates that the low cost GNSS equipment does not track the GNSS signals throughout the flight. Signal outages, cycle slips and half cycle ambiguous carrier phase measurements occur due to rapid UAV manoeuvres. Having identified this problem this work goes on to replicate and quantify it through the use of a GNSS hardware simulator. Algorithms are then devised to increase the availability of the GNSS attitude solution throughout the tracking difficulties.

Complete GNSS signal tracking failures are overcome through the innovative use of kinematic and dynamic attitude models. Both types of model give an attitude solution throughout GNSS signal tracking problems without adding significant cost or weight to the system. When tracking of the GNSS carrier phase signal is possible, novel use of the carrier phase triple difference observable allows the attitude rate to be estimated even when the carrier phase measurements are half cycle ambiguous. It is shown that integer and half integer cycle slips can be removed from the measurement through the combination of the modelling and triple difference techniques.

The attitude output of both modelling and triple difference methods is used to resolve half cycle ambiguities and make full use of half cycle ambiguous data where previously it could not have been used. Success rates of up to 99.6% have been achieved for half cycle ambiguity resolution. As a result precise and accurate GNSS attitude solutions are available at nearly every epoch for which a carrier phase measurement is output by the GNSS receivers. When no measurement is available the attitude solution gracefully degrades over time.

This work makes reliable, accurate, low cost attitude determination possible on mini-UAVs.

Table of Contents

Table of Contents		i
List of Figures		v
List of Tables		vii
Contributions & Publications		viii
Acknowledgements		xii
List of Acronyms		xiii
1 Introduction		1
1.1 Background		1
1.1.1 Problem Statement		3
1.1.2 GNSS Attitude		3
1.1.3 Alternatives		6
1.1.4 Summary		7
1.2 Research Aims and Objectives		8
1.3 Methodology		8
1.4 Thesis Overview		9
2 GNSS Principles		12
2.1 Introduction		12
2.2 Global Navigation Satellite Systems (GNSS)		13

2.2.1	Overview	13
2.2.2	Global Position System (GPS)	15
2.2.3	The GPS L1 Signal	16
2.3	GPS Signal Acquisition and Observables	17
2.3.1	C/A Code Signal Acquisition	17
2.3.2	Code Signal Tracking	18
2.3.3	The Carrier Phase Observable	19
2.3.4	Carrier Phase Tracking	21
2.3.5	Doppler	22
2.4	Error Sources & Mitigation	23
2.4.1	Ephemeris Error	23
2.4.2	Atmospheric Bias	23
2.4.3	Multipath	24
2.4.4	Antenna Phase Centre Variation	26
2.4.5	Carrier Phase Cycle Slips	27
2.4.6	Receiver Control Loop Performance	27
2.5	The GNSS Observation Equations	28
2.5.1	Code Pseudorange	28
2.5.2	Carrier Phase Pseudorange	29
2.6	Differential Positioning	30
2.6.1	Single Differencing	30
2.6.2	Double Differencing	32
2.6.3	Triple Differencing	34
2.7	Estimators	35
2.7.1	Non-Linear Least Squares	35
2.7.2	Filters	38
2.8	Stochastic Models	39
2.8.1	Variance	39
2.8.2	Correlation	41
2.9	Integer Ambiguity Resolution	43
2.9.1	Rounding	44
2.9.2	Integer Bootstrapping	44
2.9.3	LAMBDA	46
2.9.4	Validation	48
2.10	Conclusion	49

3	GNSS Attitude	51
3.1	Introduction	51
3.2	The Principles of Attitude	52
3.2.1	Reference Frames	52
3.2.2	Rotation Representations	56
3.2.3	Transformations Between Reference Frames	62
3.3	Functional Models	64
3.3.1	The Spherical Polar Functional Model	64
3.3.2	The Constrained Functional Model	66
3.3.3	The Unconstrained Functional Model	66
3.4	Pre-Processing	69
3.4.1	Satellite Position Computation	69
3.4.2	Stochastic Model	70
3.5	The Float Solution	71
3.6	The Fixed Solution	72
3.7	The Choice of Baseline Length and Antenna Location	72
3.8	Using the Baseline Constraints	73
3.8.1	Baseline Constrained Float Solution	73
3.8.2	Baseline Constrained LAMBDA	76
3.8.3	Integer Ambiguity Validation	80
3.9	Conclusion	82
4	Testing GNSS Attitude Determination	84
4.1	Introduction	84
4.2	Experimental Setup	86
4.2.1	Zero Baseline Testing	86
4.2.2	Short Baseline Testing	86
4.2.3	Hardware Simulator Testing	87
4.2.4	UAV Flights	88
4.3	Zero Baseline Test Results	89
4.3.1	Solution Accuracy & Precision	89
4.3.2	Ambiguity Resolution	91
4.4	Short Baseline Test Results	93
4.4.1	Solution Accuracy and Precision	94
4.4.2	Ambiguity Resolution	96
4.4.3	Ambiguity Validation	98

4.5	UAV Flight Results	100
4.5.1	Discussion	103
4.6	Simulated UAV Flight	105
4.6.1	Discussion	107
4.7	Conclusion	108
5	Attitude Rate Modelling and Estimation	111
5.1	Introduction	111
5.2	Ambiguity Resolution	112
5.3	The Triple Difference Observable	113
5.3.1	Relative Attitude Estimation	114
5.3.2	Cycle Slip Correction Using the Triple Difference	115
5.3.3	Triple Difference Summary	116
5.4	Attitude Modelling	116
5.4.1	Kinematic Models	117
5.4.2	The Attitude Dynamics Model	118
5.4.3	Fundamentals and Assumptions	119
5.4.4	Equations of Motion	123
5.4.5	The Aerodynamic Model	125
5.4.6	Model Inputs	132
5.4.7	Time-Stamping and Datalogging	134
5.4.8	Attitude Modelling Summary	134
5.5	Algorithms	135
5.5.1	Bridging Signal Outages	135
5.5.2	Cycle Slip Correction	136
5.5.3	Using Half Cycle Ambiguous Carrier Phase	138
5.6	Conclusion	140
6	Algorithm Testing	142
6.1	Introduction	142
6.2	Angular Velocity Estimation Using the Triple Difference Observable . . .	143
6.2.1	Static Tests	143
6.2.2	Simulated UAV Flight	146
6.2.3	Discussion	147
6.3	Half Cycle Slip Correction	148
6.4	Kinematic and Dynamic Modelling	153

6.4.1	Rotation Rate & Control Input Measurement	153
6.4.2	Test Flight	155
6.4.3	Cycle Slip Correction	157
6.4.4	Bridging GNSS Signal Outages	159
6.4.5	Special Cases	163
6.4.6	Discussion	166
6.5	Half Cycle Ambiguity Resolution	168
6.5.1	Forwards Processing	168
6.5.2	Backwards Processing	170
6.5.3	Discussion	171
6.6	Conclusion	172
7	Conclusions & Future Work	175
7.1	Conclusion	175
7.2	Future Work	181
	Appendices	184
A	Civilian UAV Operations & The K70 System	185
B	Aerial Survey Using UAVs	188
	References	197

List of Figures

1.1	GNSS Attitude Layout on a mini-UAV	4
2.1	Antenna Groundplane in a Turn	25
3.1	The Body Frame	53
3.2	The Sensor Frame	53
3.3	The Local Level Frame	55
3.4	The ‘Search and Expand’ Approach.	79
4.1	Spirent GSS8000 Multi-GNSS Hardware Simulator	87
4.2	K70 mini-UAV	88
4.3	UAV Trial Flight Groundtrack	101
4.4	Full Cycle LLIs Observed During a UAV Flight	102
4.5	Half Cycle LLIs Observed During a UAV Flight	103
4.6	The Effects of UAV Acceleration in a Turn on Phase Tracking	106
4.7	The Effects of UAV Acceleration in a Turn on Code Tracking	107
5.1	The Relationship Between the Wind Frame and the Body Frame	120
5.2	Engine Torques	128
5.3	Use of the Dynamic Model	136
5.4	Cycle Slip Correction	138
5.5	Use of the Triple Difference Velocity (Forwards)	139
5.6	Use of the Triple Difference Velocity (Backwards)	140
6.1	Drift in the Attitude Derived from Triple Difference Angular Velocity Estimates	145
6.2	Error in the Triple Difference Velocity Estimates from the Simulated UAV Dataset	147
6.3	Circular Dataset, Triple Difference Observable	149

6.4	Circular Dataset, Triple Difference Observable Corrected for Angular Velocity.	150
6.5	Error in the Triple Difference Geometric Correction Which Arises from the Angular Error	151
6.6	Worst Case Error in the Triple Difference Geometric Correction which Arises from the Angular Error	152
6.7	Rotation Rate Measured by a Crossbow IMU440 Onboard a K70 mini-UAV.	156
6.8	Control Inputs to a K70 mini-UAV.	157
6.9	Relationship between model roll output and IMU for integration times up to 10seconds	160
6.10	Relationship between model pitch output and IMU for integration times up to 10seconds.	161
6.11	Relationship between model yaw output and IMU for integration times up to 10seconds.	162
6.12	Measured and modelled roll rate during rapid turns.	163
6.13	Measured and modelled yaw rates during level flight.	164
6.14	Measured and modelled pitch during landing.	165
B.1	Generalised Survey Payload Components	189
B.2	K70 Survey Payload Components	190
B.3	Level imaging sensor with lens and ground distortions removed.	192
B.4	Error in georeferencing due to an attitude error in pitch or roll.	193
B.5	The Variation of Georeferencing Error with Pitch and Roll Error.	194
B.6	The Variation of Georeferencing Error with Heading Error.	195
B.7	Representative georeferencing errors for a pitch or roll error.	196

List of Tables

4.1	Static Zero Baseline Results	89
4.2	Kinematic Zero Baseline Results	90
4.3	Simulated Static Zero Baseline Results	92
4.4	‘Real’ Static Zero Baseline Results	92
4.5	Simulated Kinematic Zero Baseline Results	92
4.6	Static Short Baseline Accuracy and Precision	94
4.7	Static Short Baseline Attitude Accuracy and Precision	94
4.8	Simulated Short Baseline Ambiguity Resolution Results	96
4.9	Short Baseline Ambiguity Resolution Results	96
4.10	Use of the Ratio Test with the Standard LAMBDA Process	98
4.11	Use of the Ratio Test with the Constrained LAMBDA Process	99
4.12	The <i>a priori</i> Baseline Length as a Validation Tool	99
6.1	Linear Velocity Estimates using the Carrier Phase Triple Difference (Hardware Simulator)	144
6.2	Rotational Velocity Estimates using the Carrier Phase Triple Difference (Hardware Simulator)	144
6.3	Linear Velocity Estimates using the Carrier Phase Triple Difference (‘Real World’)	144
6.4	Rotational Velocity Estimates using the Carrier Phase Triple Difference (‘Real World’)	145
6.5	Linear Velocity Estimates using the Carrier Phase Triple Difference, Simulated UAV Dataset	146
6.6	Crossbow IMU440 Inertial Measurement Unit	154
6.7	Modelled total attitude error 95% confidence limits (5Hz data rate).	158
6.8	Modelled total attitude error 95% confidence limits (1Hz data rate).	158
6.9	Half Cycle Ambiguity Resolution Using the Dynamic Model	169
6.10	Half Cycle Ambiguity Resolution Using the Triple Difference	171

CONTRIBUTIONS IN THIS RESEARCH

This research contains the following contributions and innovations;

- Identification of problems with high accuracy Unmanned Aerial Vehicle (UAV) attitude determination.
- Identification of GNSS attitude determination as a suitable alternative to traditional inertial techniques.
- Full testing of the GNSS attitude method with modern, non-dedicated, low cost GPS receivers.
- Developed & tested integer ambiguity validation technique using *a priori* baseline length knowledge.
- Identification of signal tracking problems through field work and a mini-UAV. In particular loss of signal tracking in high-g turns and half cycle ambiguous carrier phase data.
- Development of kinematic & dynamic attitude models to bridge signal outages & enable cycle slip correction down to half cycle slips. Novel integration of un-augmented UAV kinematic and dynamic modelling with the GNSS attitude technique.
- Comparison of attitude model performance with the rotation rate output from an Inertial Measurement Unit on a mini-UAV. Specification, integration and testing of suitable hardware for logging mini-UAV control inputs.
- Innovative use of the GNSS carrier phase triple difference observable for small cycle slip correction and rotation rate estimation.
- Development and testing of half integer ambiguity resolution using ‘float’ baselines from the dynamic model or triple difference observable.

As a result of this research, GNSS attitude determination is a viable and attractive technique for practical use on a fixed wing mini-UAV. This work is a key enabler for the commercial use of mini-UAV’s for high resolution remote sensing.

PUBLICATIONS

- GNSS Attitude & UAV Dynamics Modelling -

GNSS Attitude Determination on a Mini-UAV Aided By a Platform Dynamics Model, J. Pinchin, D. Park, X-Q. Chen, ION GNSS 2009, Savannah, USA, September 22-25, 2009. (Oral Presentation)

The use of Single Frequency GPS Attitude Determination on a mini-UAV, J Pinchin, RIN New Navigators Seminar 2009, London, June 17th, 2009. (Oral Presentation)

Integrated Flight Dynamics Modelling for Unmanned Aerial Vehicles, Q. Ou, X. Chen, D.Park, A.Marburg, J Pinchin, Mechatronic and Embedded Systems and Applications, MESA2008, Beijing, China, 12-15th October 2008.

Enhanced Integer Bootstrapping for Single Frequency GPS Attitude Determination, J Pinchin, ION GNSS 2008, Savannah, USA, September 16-19, 2008. (Sponsored Student Paper)

An Introduction to Low Cost Attitude Sensing Using Multiple GNSS Receivers, J Pinchin, C. Hide, D. Park and X. Chen, 4th Int. Conf. on Computational Intelligence, Robotics and Autonomous Systems. Palmerston North, NZ, 28th-30th November 2007.

Development and Testing of an Integrated GPS/INS for Low Cost UAVs, C. Hide, D. Park and J Pinchin, RIN NAV07, London, UK, 30th October - 1st November 2007.

Development of a Low Cost Multiple GPS Antenna Attitude System, C. Hide, J Pinchin, D. Park, ION GNSS 2007, Fort Worth, US, 25th-28th September 2007.

- Unmanned Aerial Vehicles and Remote Sensing -

Integrating GNSS, IMU and Imagery for Automatic Orthomosaic Generation, S.Mills, J Pinchin, C.Hide, ION GNSS 2009, Savannah, USA, September 22-25, 2009.

Precise Kinematic Positioning Using Low Cost GPS Receivers and an Integer Ambiguity Constraint, J Pinchin, C Hide, D Park and X Chen, IEEE/ION PLANS 2008, Monterey, USA, May 5-8, 2008.

Video and Photogrammetry Products from UAV Derived Data(Oral Presentation),D Park, S Mills and J Pinchin, ION GNSS 2007, Sydney, 4th-6th December 2007.

Point and Click Target Location from Georeferenced Video Streams(*Oral Presentation*) , *S Mills, C Hide and J Pinchin*, *IGNSS 2007, Sydney, 4th-6th December 2007.*

CryoSat-2 validation on land and sea ice in the western Ross Sea Region, Antarctica, based on near-surface remote sensing methods,*W Rack, C Haas, N Krtzmann, W Clavano, J Pinchin, A Gough, P Langhorn*, *EGU General Assembly 2010, Vienna, Austria, 2-7 May, 2010*

ACKNOWLEDGEMENTS

This PhD research has been sponsored by the Geospatial Research Centre (NZ) Ltd. They have been generous throughout with both financial support and access to resources. Their sponsorship and the guiding hand of my supervisors, Prof. XiaoQi Chen and Dr David Park have allowed me to freely explore my ideas, for which I will be forever grateful.

It has been a privilege to work with all of the staff at the Geospatial Research Centre (NZ) Ltd. In particular Dr Chris Hide and Dr Steve Mills have been extremely supportive and have offered me their time and patience. Dr Marcus Andreotti and Mr Barry Lennox have worked hard to develop bespoke hardware, without which this thesis would not have been possible.

I would also like to acknowledge the generosity of those at the IESSG, University of Nottingham, UK. By hosting me for six months during my studies they played a key part in enabling this work. In particular I would like to thank Prof. Terry Moore and Dr Chris Hill for allowing me access to the GNSS hardware simulator which has formed a key part of this thesis.

Finally the unwavering patience of my parents must be acknowledged. They have supported me throughout my travels and in every decision I have made. We often take for granted the very things that most deserve our gratitude, I dedicate this work to them.

List of Acronyms

DCM	Direction Cosine Matrix
DLL	Delay Lock Loop
ECEF	Earth Centre Earth Fixed
EKF	Extended Kalman Filter
GLONASS	Global'naya Navigatsionnaya Sputnikovaya Sistema
GNSS	Global Navigation Satellite System
GPS	Global Positioning System
ICD	Interface Control Document
IMU	Inertial Measurement Unit
INS	Inertial Navigation System
LLI	Loss of Lock Indicator
MEO	Medium Earth Orbit
PLL	Phase Lock Loop
PPM	Proportional Pulse Modulation
QEP	Quadratic Eigenvalue Problem
RINEX	Receiver INdependent EXchange
RMS	Root Mean Square
SNR	Signal to Noise Ratio
UAV	Unmanned Aerial Vehicle

Chapter 1

Introduction

1.1 Background

In recent years Unmanned Aerial Vehicles (UAVs) have been the subject of extensive research and development. The worldwide UAV market was estimated to be worth \$US4.9 billion in 2010 and is predicted to rise to \$US11.5 billion by 2020 (*Teal*, 2010).

UAVs offer cost effective access to airspace for long periods. They can operate in potentially dangerous environments without risk to human life. For these reasons the history of the UAV has been driven primarily by military users. A good overview of military UAVs, their history and a future vision can be found in the 'Unmanned Aircraft Systems Roadmap 2005-2030' published by the US Department of Defence (*USDoD*, 2005).

Increasingly UAVs are finding application in civilian environments. Their ability to offer low cost access to airspace at low risk to operators has meant they have found application in science, security and land management. Military UAV systems may be adapted to meet civilian roles or alternatively bespoke systems may be developed to meet a specific task.

This thesis forms part of a larger body of work on the use of UAVs for aerial survey applications. The advent of powerful electronics with low cost, small form factor and low

power requirements now mean that high accuracy survey with consumer grade equipment is a possibility. The cost of a complete UAV system with imaging equipment and an associated control system can now be as low as \$US1000. Such a system can offer survey images with a ground resolution of 2cm or better. This performance and cost opens commercial possibilities far beyond traditional military operations. For example such UAVs are attractive to developing nations with large areas of forest to manage. They can be safely used for science in polar regions where manned flight is dangerous. They also have applications in niche areas such as traffic management and disaster response.

The term UAV covers a wide range of aircraft configurations. Traditional fixed or rotary wing designs compete with 'lighter than air' craft and flapping wing designs which mimic bird flight. The lack of a human pilot means that the size of the UAV is driven only by the weight of its payload, command and control systems. UAVs which weigh tens of grams for indoor use have been developed alongside those which weigh many tons for long endurance and high altitude work.

For the purposes of the research surrounding this thesis the fixed wing mini-UAV has been selected as the survey platform. A fixed wing aircraft uses minimal fuel to carry a payload long distances. It is relatively simple and safe to operate when compared to rotary wing alternatives. For a given payload weight the fixed wing UAV can be smaller than its rotary wing counterpart and tends to expose the payload to less vibration. In order to carry a typical low cost aerial survey payload the fixed wing UAV will have a mass at takeoff of 1 to 10kg. This puts it into the class of UAVs known as the mini-UAV.

The current regulatory environment for operation of UAVs in New Zealand is described in Appendix A.

1.1.1 Problem Statement

The current work focuses on the problem of georeferencing the high resolution survey data collected from the mini-UAV. That is the problem of establishing the relationship between the pixels of an image or other piece of survey data and a geographical reference frame.

The georeferencing process requires knowledge of the precise location and orientation of the survey sensor (eg, camera) at the time the data were collected. This is usually achieved by determining the trajectory of the sensor and using knowledge of the precise time of data collection to estimate the position and orientation at that time. The actual accuracy requirement will depend on the system designer and the flight profile, they are discussed further in Appendix B.

In traditional aerial survey performed by manned aircraft the trajectory is usually determined using a high grade Inertial Navigation System (INS) and a position from a Global Navigation Satellite System (GNSS) receiver. In these applications the cost of the INS and GPS receiver is analogous to the cost of operating a manned aircraft. The INS in particular is expensive, costing upwards of \$US100000, 100 times the cost of a complete UAV and imaging system.

The purpose of this work is to develop an alternative to the high grade GNSS/INS system traditionally used on manned aircraft. The solution must be cheap, lightweight and accurate enough for mini-UAV applications.

1.1.2 GNSS Attitude

GNSS attitude determination has been identified as a possible solution to the problem described above. GNSS attitude determination uses two or more GNSS receiver and antenna pairs separated by known baselines (Figure 1.1). Attitude parameters may then be

estimated directly from the GNSS observations or via an estimate of the relative positions of the antennas in a global reference frame. The GNSS attitude method has existed since the advent of GNSS (*Spinney, 1976*). The past 25 years of research has made the technique accurate and cost effective enough to be considered for UAV applications.

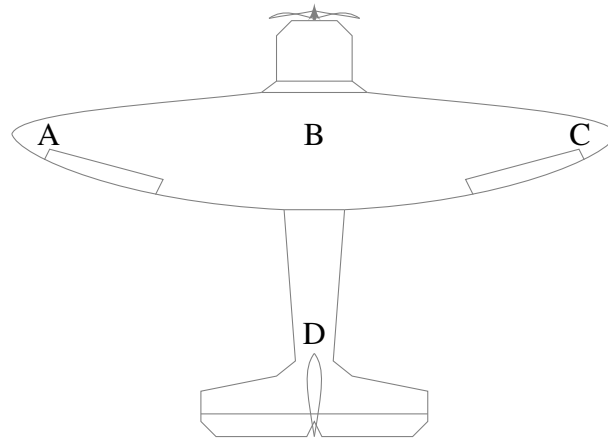


Figure 1.1: GNSS attitude layout on a mini-UAV. Baselines can be formed between any of the antenna locations A,B,C and D. Baseline A-B or A-C can be used to estimate roll and heading. Baseline B-D can be used to estimate pitch and heading. A triangle of any three baselines which are not collinear will provide an estimate of the complete three dimensional attitude.

Cost

The GNSS attitude determination technique offers a relatively low cost. Three receiver and antenna pairs are required for full attitude determination at a total cost of around \$US1000. These receivers may also be used collectively or independently to estimate the position of the UAV (*Pinchin et al., 2008*).

The number of applications for low cost attitude determination increase with the reduction in cost. Currently such systems find application in airborne (*Evans et al., 1999*) (*Lee et al., 2004*), space (*Cohen et al., 1993*), marine (*Lu, 1995*) and land environments.

Weight

The use of GNSS attitude determination also adds very little to the weight of the survey payload. The uBlox LEA-5T receiver used in this work weighs 2.1g (*u-blox AG*, 2009) while the Onshine ANT-555 antenna used weighs 80g with 2m of cable (*Onshine*, 2007).

Accuracy

The accuracy and precision of the GNSS attitude technique is difficult to determine from the literature. The variety of equipment, applications and most importantly baseline lengths used makes comparison challenging.

In his 1999 PhD thesis (*Keong*, 2001) Keong tested a two receiver GPS system over a 0.9m baseline in a static setting. The RMS error was observed to be 0.27° in yaw and 0.93° in pitch. This compares to 0.23° in yaw and 0.43° in pitch when using combined GPS and GLONASS observations from a high-end receiver.

In static tests Cannon and Ray (*Cannon and Ray*, 2000) achieved attitude accuracies of 5.93° , 6.29° and 2.66° in roll, pitch and heading respectively. This was done over a very short baseline in the order 10-14cm. The static nature of this test allowed errors to be mitigated by utilising many observations of the same attitude parameters.

In 2005 Kannemans conducted airborne testing of a two receiver GPS attitude system with 1.8m antenna separation (*Kannemans*, 2005). The test was performed aboard a full sized aircraft. Accuracies of 1.7° and 0.8° were achieved in pitch and roll respectively.

In tests conducted at sea Lu et al show accuracies of 0.04° are achievable in heading using a 15m baseline (*Lu*, 1995). These tests were performed aboard a small survey launch. Lu also shows that low cost receivers with independent oscillators (such as those used in this work) match a high grade dedicated attitude determination system with common oscillator to within 0.25° in pitch and 0.11° in yaw (*Lu et al.*, 1993).

Disadvantages

The primary disadvantages of the GNSS attitude method are those which affect all GNSS based navigation solutions. It suffers from relatively low measurement rates, is vulnerable to problems with the GNSS system itself and is vulnerable to problems with tracking the GNSS signals.

GNSS has proven itself over three decades to be sufficiently reliable for non-safety critical applications such as the one currently under consideration. Problems arising from the GNSS itself are not considered to be a major obstacle to the use of GNSS attitude for georeferencing.

Measurements from a typical IMU based attitude solution are available at upwards of 100Hz. This is a major advantage over GNSS which typically outputs measurements at a maximum of 5Hz. This problem will be particularly acute on the mini-UAV which accelerates and turns at high rates.

Finally the GNSS attitude method suffers from problems in tracking the GNSS signals. These are caused by highly dynamic trajectories, large rotation angles and electronic noise, particularly in low cost equipment.

If for any reason the raw GNSS range measurements are unavailable at one measurement epoch the solution does not degrade gracefully. In this case it is immediately lost and must be regained when GNSS range measurements become available.

1.1.3 Alternatives

The practical alternatives to the GNSS attitude technique are low cost GNSS/INS systems or the use of ground control to georeference images.

Low cost GNSS/INS systems are not suitable for accurate attitude determination on mini-

UAVs. They are prone to problems resulting from vibration of the platform and the large dynamics observed. UAVs may rotate at rates in excess of 300 degrees per second and accelerate at rates upwards of 5g. A vibration noise of up to 3g may also be observed. In addition low cost GNSS/INS systems require an accurate initial heading estimate for stable filter performance (*Farrell and Barth, 1999*). The heading observability may be improved through the use of augmenting sensors, for example the twin antenna GNSS attitude solution, a magnetometer or image recognition technology (*Hide and Botterill, 2010*), (*Hide et al., 2004*). The fact remains however that the penalty of the GNSS/INS system in weight and cost remains too high for the performance delivered.

The second alternative is to avoid directly georeferencing the data collected and use targets on the ground with known, pre-surveyed, locations. By identifying these features in aerial images, the georeferencing may be performed through the use of a least-squares procedure known as a bundle adjustment. The first disadvantage to this technique is that it will only work for imagery. Other data, for example laser ranging data, cannot be georeferenced in this way. Secondly this technique requires trained personnel with expensive survey equipment to access the ground being surveyed. This may not be practical or safe and in all cases will be expensive when compared to the cost of flying the UAV. Finally images from collected from the UAV flown at low altitude will naturally only cover a small area on the ground. To survey a large area many images will need to be collected, often upwards of 10000 images per square kilometre. To identify the pre-surveyed locations in all of these images is difficult to automate and would take many expensive man hours to complete.

1.1.4 Summary

The case can be made that GNSS attitude determination is a key enabler for aerial surveying using mini-UAVs. If the problems listed in Section 1.1.2 can be overcome for the mini-UAV environment, a wide range of commercial and research applications will have

access to low cost, high accuracy aerial survey data previously beyond their reach.

1.2 Research Aims and Objectives

The aim of this work is to develop methods which will provide a robust attitude solution using low cost GNSS attitude hardware onboard a mini-UAV.

The objectives are:

- To identify and test the current state of the art in GNSS attitude technology.
- To identify and quantify limitations with existing methods.
- To develop algorithms and methods which overcome these limitations without adding significant cost, weight or processing requirements to the mini-UAV payload.
- To quantify the benefits the developed algorithms give over existing methods and assess the suitability of the complete system for use on the mini-UAV.

1.3 Methodology

The methodology used for this research is as follows:

- Research the current state of the art in GNSS attitude technology and identify the processing methods likely to give the most robust GNSS attitude solution from low cost receivers.
- Gather GNSS datasets representative of typical mini-UAV applications. Develop a Matlab script to test the current state of the art processing techniques. Identify

problems and disadvantages with the use of GNSS attitude technology on the mini-UAV.

- Identify approaches to mitigate the effects of cycle slips and loss of lock events caused by mini-UAV attitude dynamics. Develop novel algorithms to implement these approaches.
- Apply the algorithms to the same GNSS datasets and analyse the effects on the reliability and availability of the attitude solution.

A key aspect of this research has been the development of approaches to mitigate the effects of cycle slips and loss of lock events. Two independent approaches have been devised. The first makes use of the velocities available from the GNSS triple difference observable to bridge short gaps in the GNSS attitude solution due to cycle slips. The second develops a dynamic model of the fixed wing mini-UAV to bridge longer gaps in the GNSS attitude solution due to loss of lock incidents. The use of the dynamic model allows a graceful degradation of the attitude solution in all cases where the GNSS attitude solution is lost. It utilises the control inputs to the mini-UAV to predict the resulting attitude dynamics.

1.4 Thesis Overview

- Chapter 2 will give an overview of GNSS concepts and mathematical models used in this research. The GPS L1 signal will be introduced and the methods used by the receiver to acquire and track it are examined. The GNSS range observables derived from the L1 signal will be described, including the errors and biases present in their measurement. Mitigation of these biases through differencing is described.
- Chapter 3 examines the mathematical models available for use in GNSS attitude determination. Their relative merits are discussed and the steps used to estimate at-

titude from the GNSS observables are described. Finally state of the art techniques for including geometric constraints in the GNSS data processing are examined. A model for validating carrier phase integer ambiguities using the inter-antenna distance has been developed in this research and is introduced here.

- Chapter 4 goes on to test the state of the art in GNSS attitude determination using appropriate data sets. This is the first work to test these techniques using equipment suitable for the mini-UAV.

GNSS measurements have been made using low cost receiver equipment in simulated and real environments. Static data is used to examine the performance of the system under ‘ideal’ conditions and a GNSS hardware simulator is used to examine the receiver performance in dynamic situations with precisely known trajectory.

Measurements from a low cost receiver onboard a mini-UAV are used to identify problems caused by UAV dynamics. Loss of lock incidents, integer cycle slips and half cycle ambiguous measurements are observed throughout the sample flight. The GNSS hardware simulator is then used to replicate and quantify the effect of these problems in a controlled environment.

- In Chapter 5 novel mitigation strategies are developed to deal with signal tracking problems without adding weight or cost to the system.

Kinematic and dynamic models are developed to estimate the mini-UAV attitude trajectory. The output of these models is then used to bridge signal outages and correct half integer cycle slips. This is the first time kinematic and dynamic models have been combined with GNSS carrier phase attitude determination.

Finally the triple difference carrier phase observable is employed to make use of the half cycle ambiguous carrier phase measurements. It is used to estimate the angular velocities which are then integrated over time to give an attitude output. The high precision of the output allows half integer ambiguity resolution if the initial attitude error is low.

- Chapter 6 presents the results obtained using the developed algorithms. It is shown, using real mini-UAV flight data, that the proposed algorithms allow an accurate and precise attitude solution throughout the mini-UAV flight.

A comparison is made between the attitude models and the output from a UAV mounted Inertial Measurement Unit (IMU). This shows that the dynamic model is superior to the simple kinematic models but also identifies flaws in the model when wind is present.

It is shown that by making use of the triple difference observable half cycle ambiguity resolution is possible with a high rate of success. This enables the use of half cycle ambiguous carrier phase data for georeferencing which in turn increases the reliability and availability of the GNSS attitude solution, making it practical for ‘real world’ use.

- Finally in Chapter 7 a more detailed thesis summary is presented. Conclusions are drawn and recommendations for future work are given.

Chapter 2

GNSS Principles

2.1 Introduction

Global Navigation Satellite Systems (GNSS) have been available for civilian use for more than 20 years. They can be used to provide a user with a position and time solution anywhere on or near the earth's surface. All of the systems currently in use provide a binary code signal, borne on a radio frequency carrier signal, which may be used to determine the range to the transmitting satellite. With knowledge of the satellite's position the user may then determine their position through process known as trilateration.

GNSS attitude relies on precise observations of the carrier signal and its resolution into a ranging signal. This chapter will place an emphasis on this process and the mathematical models used to obtain an attitude solution. For a more complete description of GNSS systems and methods the reader is directed to texts such as ref (*Hofmann-Wellenhof et al.*, 2003), (*Hofmann-Wellenhof et al.*, 2001), (*Misra and Enge*, 2006) or (*Kaplan and Hegarty*, 2006).

This chapter, and thesis, will focus on the use of the US Global Positioning System (GPS). GPS is the most mature of the currently available GNSS with the first satellite launched in 1978. While GPS is primarily a military system it was made available to civilian users early in its development. Its modern day popularity amongst mass-market

civilian users and relative ease of use has recently lead to a plethora of compatible low cost receiver equipment suitable for the purposes of this work.

The errors and biases present in GPS observables will be described in this chapter and a mathematical model of the observables formed. Emphasis is then placed on use of differential processing to mitigate errors and provide the high accuracy solutions necessary for effective attitude determination.

Finally in this chapter three methods of ‘integer ambiguity resolution’ are introduced. Integer ambiguity resolution is necessary to make use of the precise GPS carrier phase observable and is essential for GNSS attitude determination.

2.2 Global Navigation Satellite Systems (GNSS)

2.2.1 Overview

A Global Navigation Satellite System (GNSS) is a system which allows a user to position themselves in three dimensions using radio frequency navigation signals emitted from a number of satellites in earth orbit. By measuring the signals time of flight from satellite to receiver, a user computes their distance to the satellite. With knowledge of the satellites positions a user may use this distance to determine their position and the precise time through the solution of a set of simultaneous equations.

GNSS satellites broadcast all of the information needed for positioning or time transfer. The user only needs to receive these signals and does not require two-way communication with the satellites. This property of GNSS systems means that they can handle an infinite number of users at no extra cost to the operator and has helped GNSS become popular in civilian mass market applications.

Current operational GNSS include the Global Position System (GPS), operated by the

United States, and the Russian Global'naya Navigatsionnaya Sputnikovaya Sistema (GLONASS). A European system, Galileo, is currently in development. Regional satellite positioning services may also provide signals over a restricted portion of the earth's surface or may provide augmentation to the global systems.

Any GNSS may be described in terms of three segments, the space segment, the control segment and the user segment.

The space segment describes the space hardware, the satellites. A GNSS needs sufficient satellites to ensure adequate global availability at all times. Spare satellites are often also stored in orbit to cover gaps in the constellation caused by the failure of satellites in use. All current and proposed GNSS use satellites in Medium Earth Orbit (MEO), around 20000 km from the earth surface. Satellites are arranged in multiple orbital planes to provide global signal coverage.

The control segment consists of a network of ground control stations which monitor and control the GNSS space segment. These stations check that each satellite is performing to specifications and issue satellite 'health' warnings in the event of malfunction. The ground segment also monitors the satellites clocks to maintain the synchronised timing critical to GNSS operation. The stations also compute the satellite orbits to produce 'ephemerides' which allow the user to compute the satellite position at a given time.

Finally the user segment consists of a receiver capable of receiving and decoding the GNSS signal. Modern receivers usually contain 12 or more channels making them capable of receiving signals from 12 or more satellites simultaneously. Position and time determination may be performed in real time by the receiver hardware or raw measurements may be logged for post processing.

High end receivers may be capable of receiving and processing signals from multiple GNSS and from multiple frequencies within the same GNSS. Such receivers inevitably cost more than simple, single frequency, single system receivers. They also have a larger

form factor, require more power, require more advanced data handling and require specialised antennas.

Single frequency, single system receivers usually provide an adequate solution for most mass market users therefore they dominate the market. In this work raw measurements are taken using a typical single frequency, single system receiver. In so doing the cost of the proposed system is minimised at the expense of high quality, plentiful observations.

2.2.2 Global Position System (GPS)

The first Global Position System (GPS) satellite was launched in 1978, in 1993 the system reached initial operating capacity (IOC) (*Parkinson and Spilker, 1996*). As a military system civilian access to the signals was initially limited. On one frequency the signal was fully encrypted while on the other a technique known as ‘selective availability’ was used to decrease the accuracy of the position and time solution to a level determined by the US Department of Defense (USDOD).

Increasing civilian use of the system lead to pressure on the USDOD to remove selective availability. On 1st May 2000 the level of error introduced by the selective availability system was set to zero, effectively turning the system off. In 2007 USDOD announced that future satellites would be launched without the selective availability function.

GPS is currently undergoing a modernisation process which began in 2000. This process recognises the increasing civilian use of GPS and is introducing open signals on three frequencies. The GPS constellation currently consists of 31 actively broadcasting satellites in six orbital planes.

A wide range of user hardware is available for GPS. This ranges from high sensitivity receivers for use in environments where line of sight signals may not be available, to survey grade receivers designed for ultra precise positioning. This work is concerned with the low cost end of the GPS hardware range. This hardware is limited to a single

frequency, the L1 frequency 1575.42 MHz.

2.2.3 The GPS L1 Signal

On the GPS 'L1' frequency a 'coarse / acquisition' (C/A) code is broadcast which has been open to civilian use since GPS became operational. This C/A code is a 1023 bit pseudorandom binary code known as a 'Gold Code'. Gold Codes have excellent cross correlation properties allowing each satellite to broadcast its individual code on the same L1 frequency without fear of interference. GPS is therefore a 'Code Division Multiple Access' (CDMA) system. Since these C/A codes have been available to civilian users for some time and have well known properties they are typically the codes used in low cost GPS receivers.

Each Gold code used in the C/A signal is 1023 bits long. This code is broadcast repeatedly with a period of 1ms, or $0.977\mu\text{s}$ per bit. This equates to 293m at the speed of light. The C/A code is modulated onto the L1 sinusoidal carrier phase signal using a technique known as Binary Phase Shift Keying (BPSK). For each bit transition in the C/A code sequence a phase shift of $\pi/2$ is introduced to the carrier phase.

Also modulated on the GPS L1 signal is the navigation message. The navigation message contains information important to the user such as satellite health, ephemeris and almanac data. The almanac data is primarily used for signal acquisition and will be described in more detail later. Ephemeris information allows precise computation of the satellite position at a given time and is generally valid for four hours. The navigation message is broadcast at 50 bits per second and added to the C/A code through a modulo-2 adder before being modulated onto the carrier phase.

2.3 GPS Signal Acquisition and Observables

A full description of GPS signal acquisition and tracking is beyond the scope of this chapter, a good description can be found in (*Borre et al., 2007*). Signal acquisition has been, and is, an active area of research leading to improvements such as reduced acquisition time, high sensitivity acquisition and improved tracking accuracy. The exact techniques used are very often commercially sensitive. Of relevance to this thesis is the time taken to acquire the signals and the nature of the observables provided.

A description of the GPS L1 signal and C/A code can be found in Section 2.2.3.

2.3.1 C/A Code Signal Acquisition

When acquiring a GNSS code signal, two parameters need to be determined; the carrier phase frequency and the code phase shift.

Although all GPS satellites broadcast the L1 signal at 1575.42 MHz, a doppler effect is introduced due to the relative motion of satellite and receiver. This doppler shift may reach $\pm 10\text{kHz}$. A search therefore needs to be performed across a frequency range of $1575.42\text{ MHz} \pm 10\text{kHz}$.

Secondly the code phase shift needs to be determined. This phase shift allows the receiver to determine the start of the C/A code ‘frame’ with respect to receiver time. Since the transmission time of the C/A code is known, the signal time of flight from satellite to receiver may then be estimated. When multiplied by the speed of light this time of flight may be transformed to a range. However because the receiver and satellite local time is not necessarily synchronised with GPS system time this range estimate is corrupted by clock offsets. For this reason it is known as a ‘pseudorange’. In order to determine the code phase shift a second search is performed across all 1023 bits of the C/A code.

The acquisition process is therefore a search across two dimensions; carrier frequency

and code phase shift.

If the receiver's approximate position and an estimate of the satellite orbit is available the carrier frequency search may be directed to the most likely doppler frequency shift. An estimate of the satellite position may be made from coarse orbit information contained within the almanac, broadcast in the navigation message. Once the full almanac is received it remains valid of 6 months. This type of acquisition is called a 'warm start' and is useful if the receiver contains a valid almanac and has not moved far since its last use. Warm starts may be performed in seconds in ideal conditions, depending on the receiver type. If almanac and receiver position information is not available the receiver must perform a 'cold start' with no search optimisation. Naturally this takes considerably longer, depending on the receiver it may take many minutes. The specifications for the single frequency receiver used in this work indicates that acquisition should be achieved in 29s for a cold start and <1s for a warm start (*u-blox AG*, 2009).

2.3.2 Code Signal Tracking

After acquisition a receiver will use a Delay Lock Loop (DLL) to track the code signal. A DLL is a feedback loop which uses an error signal to control the tracking subsystem.

In its most basic form, the 'early-late tracking loop', the incoming signal is correlated with three locally generated replicas. These replicas are known as the early, prompt and late replicas. They are generally closely spaced, around half a bit of the C/A code.

If the signal is properly tracked the prompt replica should give the best correlation with the incoming code and the early and late replicas should give equal correlations. If this is not the case an error signal is generated through the use of a discriminator. Various forms of discriminator exist to give optimised performance in a given receiver and application. The discriminator output is used to steer the code generator clock and hence the locally generated code replicas. The resulting code phase shift is then used to obtain the code

pseudorange measurement.

In a modern receiver the spacing of the replicas is determined by the signal to noise ratio and has a direct impact on the noise performance of the system. If the replicas are too closely spaced the receiver will lose lock too often. If they are too far apart the noise bandwidth will increase and the quality of the pseudorange derived will suffer.

2.3.3 The Carrier Phase Observable

Finally the phase of the carrier signal may be used for positioning. It is this observable which may be used to provide optimum positioning accuracy. The wavelength of the GPS L1 signal is 19.029cm. Even very low cost GPS receivers are capable of tracking the L1 phase with a precision of 1cm or better. This compares well to a typical code tracking precision of 75cm (*Borre et al., 2007*). Since the carrier phase measurement is of critical importance in GPS attitude determination it is discussed in more detail below.

Within a GPS receiver the incoming GPS carrier phase signal is mixed with a locally generated replica to produce a signal at a third frequency known as the intermediate frequency. It can be shown that the effect of this is to produce a signal with two frequency components, one at the difference of the incoming and locally generated signal frequencies, and one at the sum. By filtering the mixed signal it is possible to isolate the first component, the difference. We now label this signal the ‘carrier beat signal’. This beat signal is at much lower frequency than the incoming GPS signal. This has many advantages, one of which is that it allows lower cost hardware to be used in the GPS receiver.

The beat signal has an associated ‘beat phase’ which is the phase actually measured by the GPS receiver. This beat phase may be expressed mathematically as:

$$\varphi(t)_B = \varphi(t)_R - \varphi(t)_G \quad (2.1)$$

Where $\varphi(t)_R$ is the phase of the locally generated signal at time t and $\varphi(t)_G$ is the phase of the GPS carrier signal at time t .

At this point the integer ambiguity is introduced. We cannot directly measure $\varphi(t)_B$ since we can only measure the fractional phase at any given time. An integer number of cycles may exist in the difference between $\varphi(t)_R$ and $\varphi(t)_G$. This is the integer ambiguity.

Before the precise nature of the carrier phase observable can be fully exploited the integer ambiguity needs to be resolved. The estimation of this integer ambiguity forms a large part of this work. A review of integer ambiguity resolution techniques is presented in Section 2.9.

It is worth noting that the carrier phase ambiguity should not change between observations.

We now modify Equation 2.1 to include this integer ambiguity, N and the measured beat phase, $\Phi(t)$:

$$\Phi(t) + N = \varphi(t)_R - \varphi(t)_G \quad (2.2)$$

Or further:

$$\Phi(t) = \varphi(t)_R - \varphi(t)_G - N \quad (2.3)$$

We are now in a position to model the carrier phase measurement including the phase change due to the signal time of flight:

$$\Phi(t_a)_a^i = f_0(t_a - T^i) + \varphi_{0a} - \varphi_0^i - N_a^i \quad (2.4)$$

In this model we have introduced notation to indicate the origin of the signals, satellite i , and the receiver a . We have also included the nominal beat signal frequency f_0 and made explicit the signal time of transmission (T^i) and reception (t_a).

The terms φ_{0a} and φ_0^i are the signal phase at a common time, $T = 0$. Their difference is a non-integer bias in the carrier phase measurement. Together φ_{0a} , φ_0^i and N_a^i form the ‘carrier phase bias’, β_a^i which is constant in time and non-integer:

$$\beta_a^i = \varphi_{0a} - \varphi_0^i - N_a^i \quad (2.5)$$

2.3.4 Carrier Phase Tracking

Carrier phase tracking is achieved through the use of a phase lock loop (PLL). A PLL is a feedback loop comparable to the delay lock loop used in tracking the code signal. Again a discriminator is used to generate an error signal which is fed back to the oscillator generating the locally generated replica.

A PLL has a number of controls which may be tuned. One of which is the noise bandwidth. The noise bandwidth controls the amount of noise tolerated by the filter. If it is too narrow, noise & initial local frequency errors will prevent the PLL tracking the carrier phase. Conversely if it is too wide the quality of the carrier phase observable will suffer.

The noise bandwidth of the receiver must also be wide enough to cope with doppler shifts in the incoming signal caused by platform dynamics. Modern receivers designed for dynamic applications often adjust the noise bandwidth according to observed signal

to noise ratio, the predicted dynamics of the application and the observed dynamics. In this case the noise characteristics of the carrier phase measurement will vary with the dynamics of the platform.

Half Cycle Ambiguities

The PLL used to track the incoming carrier phase signal must continue to track the signal through half cycle phase changes so that the modulation of gold code and navigation data will not cause a loss of lock. It's output is therefor ambiguous to half a cycle.

When both code and phase signals are properly tracked the half cycle phase changes can be removed from the incoming signal. Any that remain are due to the navigation message. Knowledge of the navigation message preamble allows the polarity of the local phase replica to be determined and full cycle ambiguous phase data to be output.

Until the navigation data preamble is detected and verified after acquisition carrier phase data will be half cycle ambiguous. The preamble is transmitted every 6 seconds. Some receivers will not output carrier phase data which is half cycle ambiguous while others will output the measurements with a flag to indicate it is half cycle ambiguous.

2.3.5 Doppler

In addition to the code pseudorange two further observables may be derived from the GPS signal. Firstly the doppler shift (also known as range rate) of the carrier signal may be used to derive the position or velocity of the receiver. This was the principle behind the precursor to GPS, the US TRANSIT system. Positioning accuracy using the doppler technique may be many orders worse than that achievable using the code pseudorange, for that reason the doppler is rarely used for positioning in modern systems.

2.4 Error Sources & Mitigation

Besides corruption due to the satellite and receiver clock offsets, the GPS code and phase observables will also be corrupted by a range of other effects. In order to achieve optimum positioning accuracy and precision these effects must be addressed.

2.4.1 Ephemeris Error

The position of the satellites at a given time is computed using the broadcast ephemeris. This ephemeris is broadcast by each satellite and allows the user to calculate the position of the satellite at a given time using the parameters of an orbit model. We are usually interested in the satellite position at the time of signal transmission.

Even if the signal time of transmission may be precisely determined, errors will still exist in the orbit parameters transmitted by the satellite and due to the divergence of the satellite path from the predicted orbit (*JPO*, 2000). These errors are mitigated in this work through differencing.

A second source of error in the satellite position calculation is in the estimated time of signal transmission. This problem is discussed in more depth later in this thesis.

2.4.2 Atmospheric Bias

The first phenomenon to affect the pseudorange and phase observables is changes to the signal propagation speed due to the atmosphere. The pseudorange is determined by multiplying the signal time of flight by the speed of light in a vacuum. For most of the signal flight this is appropriate, however when it enters the earth's atmosphere the signal propagation speed is affected. When processing GNSS observables the atmosphere is generally modelled as being composed of two parts, the ionosphere and the troposphere.

The ionosphere is the electrically charged part of the atmosphere. It may be considered to exist above 50km from the earth's surface and extending to 500km altitude or more. The ionosphere is composed of charged particles which affect the GNSS signal propagation. The speed of GNSS signal propagation is affected by the density of electrons in its path. The electron density depends largely on the solar activity at the time. The effect of the ionosphere on the code pseudorange may vary from 1m to 100m (*Hofmann-Wellenhof et al.*, 2001).

The troposphere is that part of the atmosphere which is electrically neutral. It can be considered to extend from the earth's surface to around 50km altitude. The effect of the troposphere on the GNSS pseudorange may vary from 2 to 20m. Like the ionospheric delay, the tropospheric delay depends on the density of the atmosphere. It also depends in part on the water vapour content of the atmosphere. Estimation of the tropospheric delay can therefore make the GPS useful in weather prediction.

Atmospheric delays may be mitigated by modelling. Sophisticated atmospheric models exist and their parameters may be distributed in a variety of ways. Atmospheric delays may also be mitigated by differencing measurements. If a second GPS receiver is in the vicinity of the first its measurement will be affected by the atmospheric delays in the same way. Differencing the measurements will therefore remove the effects of the atmosphere. Code and phase differencing will be described in more detail in Section 2.6.

2.4.3 Multipath

The GPS observables may be affected by a phenomenon known as multipath. Multipath is a result of the reflection of signals from surfaces other than the transmitting or receiving antennas. For example the signal may reflect from the ground before arriving at a receiving antenna. The increased path length of this reflected signal will increase the receiver's estimate of the satellite - receiver distance.

Multipath may be mitigated in kinematic applications by antenna design or in the design of the receivers' signal tracking system.

Antennas may be designed with 'groundplanes' or gain patterns which attenuate signals originating below the antenna. Such groundplanes add considerable weight to the antenna and are therefore unsuitable for use on the mini-UAV. Attenuation of signals originating 'below' the antenna may also be a disadvantage when the antenna is not level, as on a banking aircraft, this is depicted in Figure 2.1.

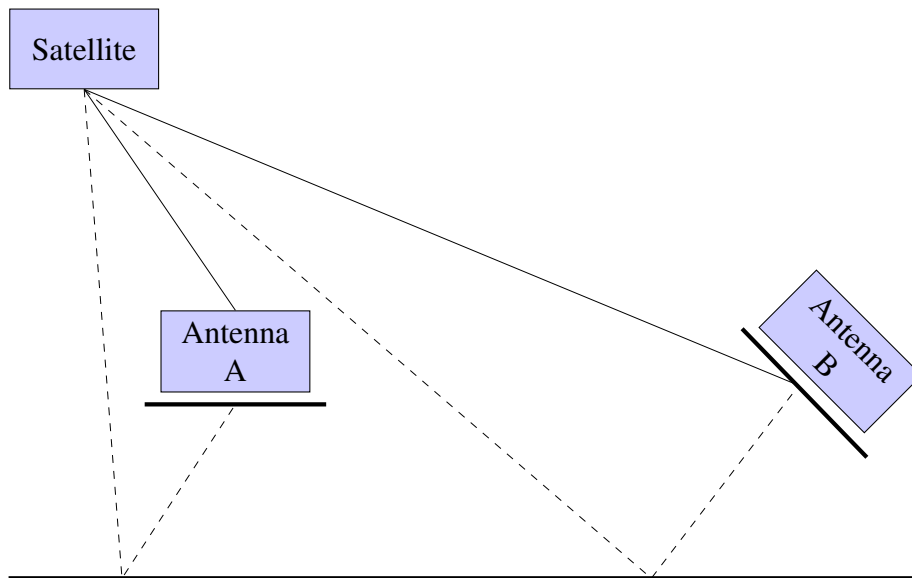


Figure 2.1: A groundplane in a turn. The direct signal from the satellite to antenna A is received while the reflected signal (dashed line) is blocked by the ground plane. When the antenna is rotated (antenna B) the direct signal may also be blocked by the groundplane.

Multipath primarily impacts the performance of the DLL used to track the code signal. Where multipath is present the received code will be distorted and result in incorrect placement of the code early, prompt and late replicas. This in turn will lead to a positive bias in the code pseudorange. Multipath mitigation strategies which work at the

signal tracking level are often propriety and not as effective as removing the multipath component at the antenna stage.

Multipath has a lesser but significant impact on carrier phase tracking. Mitigation strategies are less common and require static antennas or multiple antenna / receiver combinations which are impractical on the small UAV.

Multipath is unlikely to be mitigated by differencing since even the short baselines between antennas used for attitude determination will result in a decorrelation of the multipath bias.

In this work no multipath mitigation stratagems have been employed. Instead data has been gathered in zero (hardware simulator) or low (open field) multipath environments.

2.4.4 Antenna Phase Centre Variation

The antenna phase centre (APC) is the point at which the GNSS signal is considered to be received. It is not a physical point which can be directly measured but instead requires careful calibration of an antenna. The APC may vary by up to tens of millimetres from the physical centre of the antenna.

The APC varies between antennas and with frequency. High quality, survey grade, antennas are produced to tolerances which allow a single calibration to be used for all antennas of that type. Because such antennas are intended for precision work calibrations are usually performed and made available to the user (*Akrour and Geiger, 2005*).

Low cost antennas however are not produced to such high tolerances. Each antenna must be calibrated individually in order to obtain the highest quality results. Such calibrations are not practical or economic at this price point and therefore the APC is often an unmitigated bias.

GNSS attitude determination in this thesis has been performed between matched pairs of

antennas. In order to minimise the effect of antenna phase centre variations the antennas have been mounted in a similar orientation with the baseline measured from feed point to feed point.

2.4.5 Carrier Phase Cycle Slips

This error source only affects the carrier phase observable. Since fractional phase is measured, integer cycle slips in the receiver will not be measured. These cycle slips may be caused by temporary obstructions between satellite and receiver, a poor signal to noise ratio or high receiver dynamics. When a cycle slip occurs the integer ambiguity introduced in Section 2.3 changes and therefore must be re-estimated. Detection of cycle slips is a critical part of any carrier phase processing and will be discussed more later in this thesis.

2.4.6 Receiver Control Loop Performance

The final error source considered to be present in the GPS code and carrier observations originates in the receiver and antenna hardware. It can be thought of as noise with two components - system noise and tracking loop noise.

System Noise

System noise is generated by the receiver electronic hardware. It is composed of many sources of electronic noise including JohnsonNyquist noise (thermal noise). It is possible to quantify the system noise for a given combination of antenna and receiver (*Langley, 1997*) but in reality this is impractical and estimates of the noise performance are derived *a posteriori*.

High quality components generally lead to a lower system noise than their low quality counterparts. Therefore the system noise of a low cost receiver with a simple patch antenna is very likely to be worse than that of a high end receiver and antenna. The effect of system noise is far more pronounced on the code pseudorange than the carrier phase.

Tracking Loop Noise

The magnitude of the noise arising from the tracking loops will be determined by the loop bandwidth and the signal to noise ratio of the incoming GNSS signal. It depends largely on the proprietary receiver design and the trade off in the tracking loops design between noise performance and tracking performance.

The low cost receiver used in this work (uBlox LEA-5T) has been set up for dynamic applications to cope with the large rotation rates exhibited by the UAV. This setup results in a larger noise component in both the phase and code pseudoranges than would be expected from the same receiver setup for a static application. This is a deliberate choice in order to improve signal tracking performance and minimise loss of lock incidents and cycle slips.

2.5 The GNSS Observation Equations

2.5.1 Code Pseudorange

In order to use satellite to receiver range measurements to determine the receiver position, a model of the GNSS range observation must be created. The reader is directed to (*Blewitt, 1997*) for a good primer on this subject. First the pseudorange observation equation is introduced, Equation 2.6.

$$PR_a^i = \rho_a^i + c(dt^i - dT_a) + dion + dtrop + d\rho_a^i + \varepsilon(\phi_{rx}) + \varepsilon(\phi_{mult}) + \varepsilon(\phi_{ant}) \quad (2.6)$$

Where, PR_a^i is the pseudorange measurement from satellite i to receiver a in metres

ρ_a^i is the geometric range from satellite i to receiver a in metres

dt^i, dT_a are the satellite and receiver clock errors respectively

$dion$ is the ionospheric delay in metres

$dtrop$ is the tropospheric delay in metres

$d\rho_a^i$ is the error in the satellite position determination in metres.

$\varepsilon(\phi_{rx})$ is the receiver thermal noise in metres.

$\varepsilon(\phi_{mult})$ is the range measurement error due to multipath in metres.

$\varepsilon(\phi_{ant})$ is the antenna phase centre variation in metres.

The receiver position is contained within the geometric range term, as in Equation 2.6;

$$\rho_a^i = \sqrt{(X^i - X_a)^2 + (Y^i - Y_a)^2 + (Z^i - Z_a)^2} \quad (2.7)$$

Where \cdot^i and \cdot_a are satellite and receiver coordinate components respectively.

From equations 2.6 and 2.7 it may be seen that the observation equation is non-linear with respect to the components of the receiver position X_a, Y_a and Z_a .

2.5.2 Carrier Phase Pseudorange

Next the carrier phase observation equation is introduced, Equation 2.8.

$$\Phi_a^i = \frac{\rho_a^i}{\lambda} + \beta_a^i + \frac{c}{\lambda}(dt^i - dT_a) - dion + dtrop + d\rho_a^i + \varepsilon(\phi_{rx}) + \varepsilon(\phi_{mult}) + \varepsilon(\phi_{ant}) \quad (2.8)$$

It can be seen that the carrier phase observation equation is of the same form as the pseudorange observation equation with appropriate scaling by the wavelength λ . Recall that β_a^i is the ambiguity defined in Equation 2.5. Notice also that the ionospheric bias now has a negative sign. This reflects the increase in phase velocity the signal undergoes as it passes through the atmosphere.

2.6 Differential Positioning

As introduced in Section 2.4 if two or more receivers are present combinations of their measurements may be used to mitigate the biases introduced by atmospheric effects. This technique may also be applied to mitigation of the range biases introduced by the receiver and satellite clock offsets from GPS time (the ‘clock offsets’). In this section three combinations of GNSS carrier phase observations will be introduced.

2.6.1 Single Differencing

The single difference observation equation is obtained by differencing the observation equations between two receivers, a and b, and a common satellite, i. In Equation 2.9 the delta symbol, Δ , is used as a mnemonic device to indicate quantities obtained by differencing two points on the ground.

$$\lambda\Delta\phi_{ab}^i = \Delta\rho_{ab}^i + \Delta\lambda\beta_{ab}^i + \Delta c(dt_{ab}^i) + \Delta c(dT_{ab}) - \Delta dion_{ab}^i + \Delta dtrop_{ab}^i + \Delta d\rho_{ab}^i + \Delta\varepsilon(\phi_{ab}^i) \quad (2.9)$$

The primary benefit of using the single difference observation is the mitigation of atmospheric biases. If the receivers a and b are collocated the atmospheric biases they observe will be identical. These biases will therefore be completely removed by single differencing and the terms $\Delta dion_{ab}^i$ and $\Delta dtrop_{ab}^i$ will approach zero. As the inter-receiver distance ('baseline length') is increased, the atmospheric biases observed will decorrelate and the $\Delta dion_{ab}^i$ and $\Delta dtrop_{ab}^i$ terms will increase. The point at which these terms become significant depends on both the bias (error) acceptable to the user and the prevailing atmospheric conditions. The practical limit for the tropospheric term is usually reached at around 30km separation. A height difference between receivers will have a large difference on the differential tropospheric bias. The practical limit for the ionospheric term varies to a greater extent and may be reached at 1 - 30km separation. In the attitude determination application the antenna separation is constant and very short compared to the decorrelation distances. The atmospheric effects are therefore considered to have been completely removed by single differencing. In this work a 'short' baseline length is considered to be one in which the differenced atmospheric biases are negligible. This applies to all baselines under 100m and is certainly true for typical attitude determination baselines of 1-2m.

Satellite clock and ephemeris errors are also mitigated by the single difference operation. It may be assumed that the satellite clock bias changes very little between the signal time of transmission to receivers a and b. On differencing it may therefore be assumed that the term $\Delta c(dt_{ab}^i)$ is also zero. The same is true for the differenced ephemeris error term, $\Delta d\rho_{ab}^i$.

The disadvantage of differencing is the associated increase in measurement noise. The

term $\Delta\epsilon(\phi_{ab}^i)$ can be expected to be the sum of $\epsilon(\phi_a^i)$ and $\epsilon(\phi_b^i)$.

Significantly, single differencing also means that we can no longer estimate the position of an individual receiver, a or b. Instead we estimate the receiver's relative positions. In positioning applications this means that the position of one receiver must be known, the base station. By estimating the receivers' relative positions we can then derive the position of the second, roving, receiver. In attitude determination applications knowledge of the base receiver position is not necessary since the attitude information is contained in the baseline between receivers.

We now make the assumption that receivers a and b are in close proximity. The single difference observation equation is given with the negligible terms removed:

$$\lambda\Delta\phi_{ab}^i = \Delta\rho_{ab}^i + \Delta\lambda\beta_{ab}^i + \Delta c(dT_{ab}) + \Delta\epsilon(\phi_{ab}^i) \quad (2.10)$$

It may be seen that the integer ambiguity and receiver clock biases remain to be mitigated.

2.6.2 Double Differencing

The primary purpose of double differencing is to remove the receiver clock biases. A double difference observation is simply the difference between two single difference observations to a pair of satellites labelled i and j . The symbol ∇ is introduced as a mnemonic device to indicate between satellite differencing.

In this work a single 'pivot' satellite is used and other single difference observations are all differenced with respect to this satellite. The satellite with the highest elevation above the horizon is chosen as the pivot satellite.

$$\lambda \nabla \Delta \phi_{ab}^{ij} = \nabla \Delta \rho_{ab}^{ij} + \lambda \nabla \Delta \beta_{ab}^{ij} - \nabla \Delta c(dt_{ab}^{ij}) - \nabla \Delta dion + \nabla \Delta dtrop + \nabla \Delta d\rho_{ab}^{ij} + \varepsilon(\nabla \Delta \phi) \quad (2.11)$$

We assume that observations are made to all satellites simultaneously and therefore the receiver clock bias is constant for all observations. Under this assumption the term $\nabla \Delta c(dt_{ab}^{ij})$ becomes zero.

Double differencing also has an important effect on the carrier phase bias β . It can be shown that the double difference carrier phase bias, β_{ab}^{ij} , cancels to become simply a double differenced integer ambiguity, N_{ab}^{ij} . The double differenced integer ambiguity is, as the name suggests, integer in nature and the carrier phase bias may now be estimated using this integer constraint. this process is known as integer ambiguity resolution and is examined in detail later in this work.

We can further assume that the error in the satellite position determination is identical for receiver a and b . This assumption is based upon the realisation that the majority of the error in the satellite position determination is due to an ephemeris error, not transmission time estimation. Under this assumption the term $\nabla \Delta d\rho_{ab}^{ij}$ may also be removed.

The downside to the double difference observation is once again an increase in noise. Not only will the noise term increase, systematic effects due to atmospheric biases not cancelled in the single differencing process will also be amplified. In the limit that the receivers are collocated the double difference observation equation may be simplified to:

$$\lambda \nabla \Delta \phi_{ab}^{ij} = \lambda \nabla \Delta \rho_{ab}^{ij} + \nabla \Delta N_{ab}^{ij} - \varepsilon(\nabla \Delta \phi) \quad (2.12)$$

If the same double differencing process is undertaken with the code observables:

$$\nabla\Delta PR_{ab}^{ij} = \nabla\Delta\rho_{ab}^{ij} - \varepsilon(\nabla\Delta\phi) \quad (2.13)$$

After double differencing we notice that the integer ambiguity remains unmitigated. Therefore the triple difference observation is introduced.

2.6.3 Triple Differencing

A triple difference observation is simply the difference between two double difference observations separated by time. The triple difference observation equation is introduced in Equation 2.14.

$$\lambda\delta\nabla\Delta\phi_{ab}^{ij} = \delta\nabla\Delta\rho_{ab}^{ij} + \varepsilon(\delta\nabla\Delta\phi) \quad (2.14)$$

Since the double difference integer ambiguity should be constant in time it has been removed by triple differencing. However this is not true if a cycle slip occurs between the epochs used in triple differencing. In this case a large discontinuity appears in the triple differenced observable. This in turn makes the triple difference observable useful for cycle slip detection.

The primary disadvantage of the triple differenced observable is the amplification of noise and other biases in the threefold differencing process. This increase in noise usually makes the triple difference observable unsuitable for use in precise positioning and the double difference is usually chosen as the optimum observable.

2.7 Estimators

The estimator is the mathematic process used to estimate the desired parameters (in this case attitude parameters) from the observables. Many estimators are available and have been applied to GNSS data processing.

Estimation of baseline or attitude parameters from the observables requires the solution of simultaneous non-linear equations - the observation equations. The Non-Linear Least Squares and Extended Kalman Filter approach have proven to be reliable and robust in most GNSS applications. They require minimal processing power and are robust to errors in the initial state estimates and have therefore been chosen for this work.

2.7.1 Non-Linear Least Squares

The non-linear least squares method is an extension of the standard least squares estimator. It aims to adjust a set of variables in a functional model to fit a set of observations. A good text on the subject is (*Teunissen, 2000*).

In the case of GNSS attitude the variables are the baseline or attitude parameters (hereafter known as the state vector) and the observations are the observables. As has been shown through the observation equations, the observables have a non-linear relationship to the state vector.

If we have a vector of m observations y with variance - covariance \mathbf{Q}_y and a vector of n parameters x ($(m > n)$) they are related through the non-linear model \mathbf{A} ;

$$y = \mathbf{A}(x) \tag{2.15}$$

We then define the residuals as;

$$r_i = y_i - \mathbf{A}(x_i) \quad (2.16)$$

And we seek to minimise the sum of the square of the residuals;

$$S = \sum_{i=1}^m r_i^2 \quad (2.17)$$

The minimum of S occurs when the gradient of Equation 2.16 is zero and $y_i \approx \mathbf{A}(x_i)$. It is not possible to obtain a closed form solution to this problem.

Instead an iterative approach is taken in which an approximate value for the state vector x is chosen, (x_0) , and the non-linear model \mathbf{A} is linearised about this approximate value.

Commonly Taylor's theorem is used to linearise the model;

$$f(x) = f(x_0) + \frac{d}{dx}f(x_0)\Delta x + \frac{1}{2!} \frac{d^2}{dx^2}f(x_0)\Delta x^2 + \dots + \frac{1}{(q-1)!} \frac{d^{(q-1)}}{dx^{(q-1)}}f(x_0)\Delta x^{(q-1)} + R \quad (2.18)$$

If the assumption is made that the remainder term R and terms with $q > 2$ are negligible then;

$$f(x) \doteq f(x_0) + \frac{d}{dx}f(x_0)\Delta x \quad (2.19)$$

And:

$$a_i(x) = a_i(x_0) + \delta a_i(x_0)\Delta x \quad (2.20)$$

Where;

$$\delta a_i(x_0) = \frac{d}{dx} f(x_0) \quad (2.21)$$

We define the observed minus computed observations as;

$$l_i = y_i - \mathbf{A}x_0 \quad (2.22)$$

The linearised model can now be expressed as;

$$\Delta y = \delta_x \mathbf{A}(x_0) \Delta(x) \quad (2.23)$$

And $\delta_x \mathbf{A}(x_0)$ is a $m \times n$ matrix of the partial derivatives of the observation equations evaluated at x_0 .

The linearised problem 2.23 can now be solved as a weighted linear least squares problem with weight matrix $\mathbf{W} = \mathbf{Q}_y^{-1}$.

$$\hat{x} = x_0 + (\delta_x \mathbf{A}(x_0)^T \mathbf{W} \delta_x \mathbf{A}(x_0))^{-1} (\delta_x \mathbf{A}(x_0)^T \mathbf{W} l) \quad (2.24)$$

And;

$$\mathbf{Q}_{\hat{x}} = ((\delta_x \mathbf{A}(x_0))^T \mathbf{Q}_y^{-1} (\delta_x \mathbf{A}(x_0)))^{-1} \quad (2.25)$$

The problem is iterated, updating at each iteration k ;

$$x_k = x_{k-1} + \hat{x} \quad (2.26)$$

The solution is deemed to have converged when the change in the state vector \hat{x} is below

a threshold level set by the user. More robust methods have been proposed such as the Levenberg-Marquardt algorithm which aims to speed up convergence or prevent divergence in the solution. In this work these additions to the basic non-linear least squares algorithm have proved to be unnecessary and have therefore been omitted.

The non-linear least squares method is of use to this work in that it allows epoch by epoch analysis of the receiver and algorithms. Each measurement epoch is unaffected by those before it.

Conversely the primary disadvantage of the non-linear least squares method is that it does not take into account observations taken outside of the current observation epoch. It relies on the strength of the single epoch, single frequency model which is often insufficient. To solve this problem the Extended Kalman Filter is used.

2.7.2 Filters

Using filters can improve the attitude solution available from a given set of observations by incorporating the history of the observations in the estimate.

For example, the Extended Kalman Filter (EKF) is the *de facto* standard for kinematic GNSS processing. It has problems including divergence if the initial state estimate is sufficiently in error. However it utilises more observations than the single epoch, non-linear least squares approach and so, given time to converge, it will produce a superior solution.

The EKF is not used in this work since it is unstable if a good prediction of the change in attitude is not available.

If it is to provide superior performance compared to an epoch-by-epoch approach it also requires time to converge to a solution. This time is not available when estimating carrier phase ambiguities if they are subject to frequent cycle slips. This is often the case when

using low cost equipment in the mini-UAV environment as will be seen in Chapter 4.

The performance of filtering techniques with the rapidly changing motions of the mini-UAV is a subject for research beyond the scope of this thesis.

2.8 Stochastic Models

In order to optimise the processing of the GNSS observables a stochastic model must be formed. This model must describe both the relative precision of the observations (quantified through their variance) and their correlation. This model is quantified in the variance - covariance matrix of the observations, \mathbf{Q}_y .

Such a model is particularly important for code pseudorange observations from low cost equipment whose variances may vary considerably (*Wieser, 2007*).

We assume that the errors present in the observations have zero-mean and are initially uncorrelated.

2.8.1 Variance

In Double and Triple differenced observations a number of error sources still remain even on short and zero length baselines. Noise from the receiver hardware is the dominant component but multipath and remaining biases which were not removed through differencing may also be present.

The variance of the observations may be estimated if the receiving equipment is static. In kinematic applications however this is not practical and an *a posteriori* estimate sometimes derived from a functional model is used.

Equal Variance

The simplest functional model is one in which each measurement is deemed to have an equal variance to all the others. It follows that no one measurement is given greater weight than any other in the estimator. The actual variance assigned will be determined from experience with that receiver / antenna combination.

Signal to Noise Model

Many stochastic models have been proposed based on the signal to noise ratio reported by the receiver eg (*Brunner et al.*, 1999), (*Wieser et al.*, 2005). The SIGMA- ϵ model is one such model and has been shown to be effective when processing carrier phase or code pseudorange observables.

Using the SIGMA- ϵ model the variance of a measurement is given by:

$$\sigma_i^2 = C \cdot 10^{-\frac{C/N_0}{10}} \quad (2.27)$$

Where C is a model parameter and C/N_0 is the signal to noise ratio in dBHz^{-1} .

Use of such a model has the advantage of including most kinds of error source in the variance estimation. The variance of the observations is likely to significantly increase where the satellite has a low elevation in the sky and where multipath is present. Both of these will result in a lower signal to noise ratio and hence be reflected in this model.

The disadvantage of using this model, or any based on the signal to noise ratio, is in the way in which the signal to noise is measured and reported by the receiver manufacturer (*Ozlu demir*, 2004). No standardised way of presenting the signal to noise ratio to the user has been implemented and it therefore varies from receiver type to receiver type. Some data formats (for example the RINEX format) also give the signal to noise ratio on a scale

of 1-10 which may then be mapped to their values in dBHz^{-1} . This results in aliasing of the reported signal to noise ratio and is the reason that this method is not used in this work.

Elevation Weighting

As alluded to above, the variance of the observables will increase for satellites with a low elevation relative to the horizon. For this reason an ‘elevation mask’ of 10-15 degrees is often used to preclude low elevation observations from the attitude or position estimate.

A more refined model of the change in variance with elevation is used in this work, alongside the elevation mask for very low satellites (*Rothacher et al.*, 1998).

$$\sigma_i^2 = \frac{\sigma_0^2}{\sin^2 E_i} \quad (2.28)$$

Where σ_0^2 is an a posteriori estimate of the observable’s variance and E_i is the elevation of the satellite transmitting the signal.

In this work it is largely assumed that multipath is absent and that the primary cause of changes in the variance is elevation. This is therefore the chosen model.

2.8.2 Correlation

While it is assumed that un-differenced observations are uncorrelated, differencing will introduce predictable correlations. Since double and triple differenced observables are used in this research their properties are discussed.

Double Differencing

The double differenced operator \mathbf{D} acts on a vector of un-differenced observations Φ to form the double difference observables:

$$\nabla\Delta\Phi = \mathbf{D}\Phi \quad (2.29)$$

This operator can now be used to derive the variance - covariance matrix \mathbf{Q} of the differenced observables through propagation of error;

$$\mathbf{Q} = \mathbf{D}^T \boldsymbol{\sigma} \mathbf{D} \quad (2.30)$$

Where $\boldsymbol{\sigma}$ is a vector of the variances of the un-differenced observations.

Triple Differencing

The triple differenced operator \mathbf{T} acts on a vector of un-differenced observations Φ to form the triple difference observables:

$$\delta\nabla\Delta\Phi = \mathbf{T}\Phi \quad (2.31)$$

Again this operator can now be used to derive the variance - covariance matrix \mathbf{Q} of the differenced observables through propagation of error;

$$\mathbf{Q} = \mathbf{T}^T \boldsymbol{\sigma} \mathbf{T} \quad (2.32)$$

Where $\boldsymbol{\sigma}$ is a vector of the variances of the un-differenced observations.

2.9 Integer Ambiguity Resolution

The problem of resolving the integer ambiguity, N_a^i , or more commonly the double difference integer ambiguity $\nabla\Delta N_{ab}^{ij}$, to an integer has been the study of much research since attempts were first made to use GPS for precise positioning. Many methods have been proposed and a complete review of all these is beyond the scope of this thesis (*Verhagen, 2004*). Instead only those methods used in this work are introduced.

Hereafter the term integer ambiguity will be used to describe the double difference integer ambiguities $\nabla\Delta N$. To keep the notation concise, the symbol \hat{a} will be used to denote an estimate for $\nabla\Delta N$ which is allowed to take any real value. An estimate for $\nabla\Delta N$ which is constrained to integer values only will be denoted \check{a} .

The steps of the integer ambiguity process are common to all the estimators introduced in this section. First a ‘float’ solution is obtained in which the integer ambiguities are estimated alongside the attitude or baseline components and are allowed to take any real value. Since this stage does not take into account the integer nature of the ambiguities the ‘float’ solution naturally does not offer the most precise solution.

Since one integer ambiguity is introduced for each double difference carrier phase observation, the float solution must be obtained using both code and carrier phase observables. In the case where non-linear least squares is used to estimate the parameters on an epoch by epoch basis the float attitude solution will be no different to that obtained by solely using the code observable.

Secondly an estimator is used to resolve the float ambiguities to integers. These estimators are described below. The output from each is a set of integer estimates for the ambiguities.

Finally a ‘fixed’ solution is obtained for the attitude or baseline components in which the estimated integer ambiguities are taken as known and the carrier phase observables are

treated as range signals. The fixed solution takes full advantage of the precise nature of the carrier phase observable.

2.9.1 Rounding

The most straight forward method of integer ambiguity resolution is to simply round the ‘float’ estimate of the ambiguities to the nearest integer. While this method gives computational simplicity it does not take into account the variance - covariance of the float estimates. Since this information is not used the rounded estimate is not optimal.

In practice the success rate obtained when using rounding is often very low (*Teunissen, 1998*) and it is rarely chosen as an integer ambiguity estimator.

2.9.2 Integer Bootstrapping

Integer bootstrapping is based upon sequential conditional least squares estimation. The real valued float ambiguity estimates (\hat{a}_i for $i = 1, \dots, n$) are conditioned to integers (\check{a}_i) taking into account their correlation with the previous conditional estimates (*Teunissen, 1998*).

Since the bootstrapped estimator does not make use of variance information it is not an optimal estimator. It is however much less computationally intensive than other search based methods such as the LAMBDA method introduced below. This makes it an attractive method for use in real time applications particularly when only low cost hardware is available.

Firstly each real valued ambiguity \hat{a}_i is adjusted using sequential conditional least squares:

$$\hat{a}_{i|I} = \hat{a}_i - \sum_{j=0}^{i-1} \sigma_{i,j|J} \sigma_{j|J}^{-2} (\hat{a}_{j|J} - z_j) \quad (2.33)$$

Where $\sigma_{x|y}$ is the variance of x conditioned on y , $I = \{1, \dots, (i-1)\}$, $J = \{1, \dots, (j-1)\}$ and $z \in Z^n$.

The sequential conditional least squares estimates are then rounded to the nearest integer:

$$\check{a}_j = [\hat{a}_{j|J}] \quad (2.34)$$

Where $[.]$ represents nearest integer rounding and $j = 1, \dots, i-1$.

The unit lower triangular decomposition of the float ambiguity covariance matrix may be used when estimating the bootstrapped solution. It may be expressed as;

$$Q_{\hat{a}} = LDL^T \quad (2.35)$$

Where the entries of L are;

$$L_{ij} = \begin{cases} 0 & \text{for } 1 \leq i < j \leq n \\ 1 & \text{for } i=j \\ \sigma_{i,j|J} \sigma_{j|J}^{-2} & \text{for } 1 \leq j < i \leq n \end{cases} \quad (2.36)$$

Elements of L may therefore be substituted into Equation 2.33;

$$\check{a}_{b,i} = \left[\hat{a}_i - \sum_{j=0}^{i-1} L_{ij} (\hat{a}_{j|J} - z_j) \right] \quad (2.37)$$

2.9.3 LAMBDA

Finally we come to the **Least-squares AMBiguity Decorrelation Adjustment**, or LAMBDA, method. LAMBDA was proposed in 1993 (*Teunissen, 1993*) and has been shown to be the optimal integer ambiguity estimator. It consists of two stages, decorrelation of the ambiguities followed by an integer least squares process.

Much has been written on the LAMBDA method and a complete description will not be reproduced here. A good description of the process and its implementation can be found in (*De Jonge and Tiberius, 1996*) and (*Teunissen, 1999*). Instead the aspects important to this thesis are described. Of particular interest is the integer least squares process.

Integer Least Squares

Like the standard least squares method first proposed by Carl Friedrich Gauss in the 1700s, integer least squares seeks to minimise the square of the difference between observed values and values given by a mathematical model (*Teunissen, 2002*).

In our application we seek to find the integer ambiguity vector closest to the real valued float estimate. To optimise our solution we measure this distance in the metric of the variance of each float ambiguity, the Mahanobolis distance. Or otherwise:

$$\check{a} = \min_{a \in \mathbb{Z}^n} \|(\hat{a} - a)\|_{Q_{\hat{a}}}^2 \quad (2.38)$$

Where \check{a} is the selected integer ambiguity vector.

Since it is not possible to determine \check{a} directly, a search procedure is employed. A set of candidate integer vectors is chosen and the Mahanobolis distance of each one to the float solution is calculated. The candidate vector which minimises this Mahanobolis distance is then selected as \check{a} .

The choice of candidate integer vectors to test is critical to the process. The approach taken is first to identify a volume of ambiguity space around the float estimate. The volume of this space must be large enough to contain at least one candidate integer vector but not large enough to contain many candidates and make to process unduly computationally expensive. Since the bootstrapped integer vector will be close to the float ambiguity vector it is a sensible choice for setting the search space. Its Mahanobolis distance from the float ambiguity vector is calculated and all candidate vectors within this distance are collected (if any). The size of the search space is incrementally increased until the required number of candidates has been found (usually two for validation purposes described later).

As will be seen in Section 2.9.4 the two best candidate integer vectors are often required for validation of the chosen ambiguity vector. If insufficient vectors are found within the search space defined by the bootstrapped solution the search volume may be incrementally increased. The relevance of the volume of the search space to integer ambiguity resolution is investigated in (*Teunissen et al.*, 1996).

The LAMBDA Z-Transform

The float ambiguities \hat{a} are correlated due to the double differencing process. This correlation can makes the integer least squares search procedure very inefficient and so in the LAMBDA process the ambiguities are transformed using a transformation known as the Z-Transform.

The derivation of the Z-Transform in described in (*Teunissen*, 1995) and not reproduced here. It's effect is to decorrelate the ambiguities, improve or maintain their precision and retain their integer nature.

The transformation is performed on the ambiguities and their variance - covariance:

$$z = Za \quad (2.39)$$

$$\mathbf{Q}_z = Z\mathbf{Q}_aZ^T \quad (2.40)$$

The search for the ambiguities is now performed in the transformed volume Ω_z . When the chosen integer ambiguity candidate \check{z} is found the reverse transformation is performed on it.

The effect of decorrelating the ambiguities is to minimise and equalise the conditional variances. Using the Z-transform can therefore be expected to increase the success rate of integer bootstrapping.

2.9.4 Validation

Once a integer vector has been found it must be verified. Many approaches have been proposed (*Verhagen, 2004*), and a theoretical basis described (*Teunissen and Verhagen, 2004*). Of these the so called ratio test has proved to be the most popular.

The ratio test was first proposed in 1991 (*Euler and Schaffrin, 1991*). It requires that the best two integer vector candidates are obtained. The ratio of the squared norm of the ambiguity residual vectors (Mahalanobis distances $\|\hat{a} - \check{a}\|_{Q\hat{a}}^2$) are examined. If the ratio is not sufficiently high, usually above a preset threshold, it is concluded that the candidates cannot be sufficiently discriminated and the candidate integer vector is rejected.

There is no theoretical basis which allows a fixed value for the test threshold to be determined. Therefore when used in this way the ratio test as a whole lacks a theoretical background. It has however been shown to work effectively in practice. Since it is computationally cheap and simple to implement it is now considered the standard method.

Naturally the ratio test may not be applied to integer vectors determined using the integer bootstrapping or rounding estimators. In Chapter 3 a validation test which uses *a priori* baseline length information will be developed. This test is applicable to all estimators.

2.10 Conclusion

This chapter has introduced the models and concepts required to use a GNSS system for precise positioning or attitude determination.

Of the currently available GNSS, GPS has been identified as the most mature and most suitable for this work. The mass market appeal of GPS has led to the development of low cost equipment which is optimised for applications where cost, size and weight are a key factor, such as the mini-UAV.

In this chapter the significant sources of error in GNSS signals have been examined and mitigation strategies have been identified. Low cost receiver and antenna equipment is likely to show degraded performance when compared to higher cost options. This is mainly due to the noise performance of the cheaper electronic components, the lack of an antenna calibration and the inability of the cheap antenna to mitigate multipath signals.

A mathematical model of the GNSS carrier phase and code pseudorange observations has been introduced. Using this model it has been shown that by using a technique called differential positioning, most of the significant error sources can be eliminated. The single, double and triple difference observation equations have been developed.

Mathematical estimators to be used in processing the GNSS observables have been identified and discussed. The Non-Linear Least Squares method has been selected for use in this work due to its robustness given a good initial state estimate. It also allows the performance of the hardware and models to be examined without introducing filtering artifacts.

Stochastic models have been introduced to describe the variance and covariance of the GNSS observations. While the undifferenced observations are assumed to be uncorrelated, it has been seen that the correlations introduced by differencing must be taken into account. Three methods of modelling the observation variance have been introduced. Of these a model based on satellite elevation has been selected since it is equally effective regardless of receiver type.

Finally three methods of resolving the double differenced integer ambiguities have been described and the principles of the integer bootstrapping and integer least squares method introduced for use later in this thesis.

Chapter 3

GNSS Attitude

3.1 Introduction

GNSS attitude determination is the name given to deriving platform attitude from the GNSS observables. It has existed since the advent of GPS (*Spinney, 1976*), (*Cohen, 1993*) but only in recent times has it become accurate and practical enough for mini-UAV applications. If multiple antennas are positioned around a rigid platform, in this case the UAV, their relative position will be related to the platforms attitude at a given measurement epoch.

If two antennas are used they will be capable of providing two dimensions of the attitude, usually heading and roll or pitch. If three or more are used it will be possible to determine all three dimensions of the platform attitude.

In this chapter the key concepts and procedures needed to derive platform attitude from the GNSS observables are discussed. First the reference frames and rotation parameters relevant to this thesis are introduced.

The chapter then goes on to discuss the available functional models for use in the mathematical estimator. Particular emphasis is placed on the algorithm used in this work. Finally adaptation of the ambiguity resolution methods for attitude determination is ex-

amined.

3.2 The Principles of Attitude

In this section the concepts and mathematical systems behind the concept of attitude are discussed. Three ways of representing attitude are introduced and their qualities examined. The reference frames used in this thesis are described and their interrelationships explored.

3.2.1 Reference Frames

In this work three cartesian reference frames are used. This section describes each frame and gives the important relationships between them.

The Body Frame

As the name suggests, the body frame is affixed to, and moves with, the platform body itself. It is an orthogonal cartesian system with an origin defined at a point on the platform. Axes may be defined either relative to the platform or the navigation system. In this work both definitions are used and termed the body frame and sensor frame respectively.

In this thesis the term body frame is used to describe a frame with its origin at the UAV centre of gravity. The x_b axis points towards the nose of the aircraft, the y_b axis through the right wing and the z_b axis points down forming a right handed system. The body axis will primarily be used when discussing aircraft dynamics.

A second body frame is defined which will be termed the 'sensor frame'. This frame is affixed to and moves with the platform but is defined relative to the navigation sensors, in particular the antennas used in the GPS attitude system. In such a system one antenna is

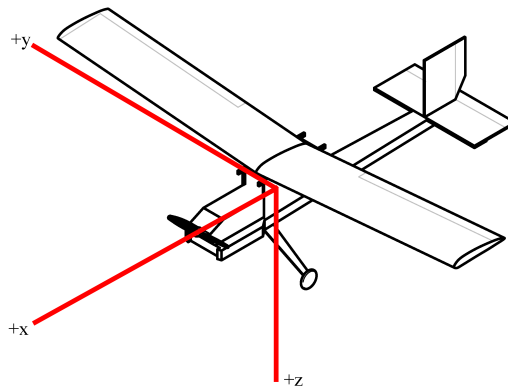


Figure 3.1: The Body Frame

designated the ‘base’ antenna. This antenna defines the origin of the sensor frame. In this work the base antenna is either on top of the wing (over the centre of gravity) or on the top of the leftmost wingtip. The y_n axis direction is defined as running from the centre of this base antenna through the second antenna (‘roving’ antenna) on the rightmost wingtip. The z_n axis is defined as being normal to the plane which passes through the base and roving antenna with its positive direction down. The x_n axis completes the right hand orthogonal system.

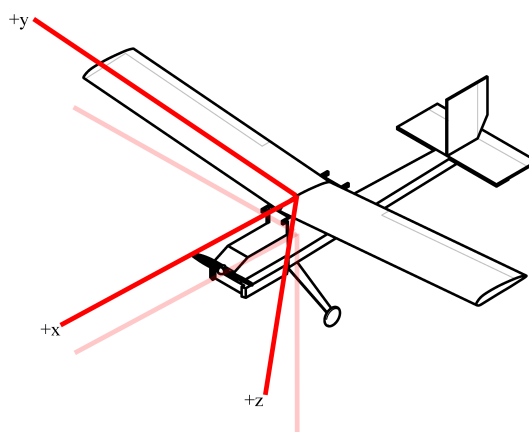


Figure 3.2: The Sensor Frame, body frame axis are shown for reference.

The transform between body and sensor frame can be achieved using a translation and rotation operation. The translation required will be known as the lever arm. The rotation is known as the boresight. Since the relationship between the sensor and body frame is constant, the lever arm and boresight are constants which may be obtained by survey of the platform.

The Local Level Frame

The local level frame is important when discussing the orientation and motion of a platform. For the purposes of this work its origin is at the UAV centre of gravity. The y_{ll} axis points to geodetic north and the z_{ll} axis points away from the centre of the earth through the centre of gravity (up). Once again the x_{ll} axis completes the right hand orthogonal system, pointing east.

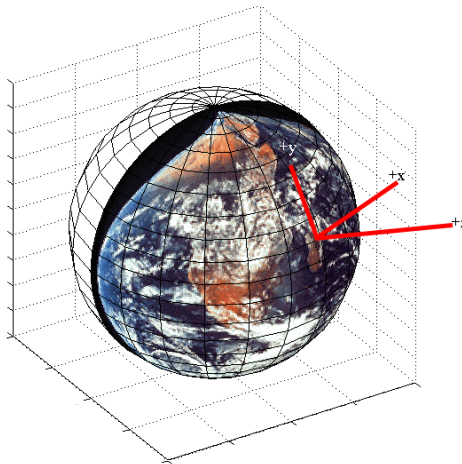


Figure 3.3: The Local Level Frame

The Earth Centre Earth Fixed Frame

The origin of the Earth Centre Earth Fixed (ECEF) frame is the centre of mass of the earth. The frame is not a true inertial frame since it rotates with the earth at $\sim 7.3 \times 10^{-5}$ rads^{-1} . The z_e axis runs along the mean axis of rotation towards the north celestial pole. The x_e and y_e axes run through the equatorial plane with the x_e axis pointing in the direction of the Greenwich meridian and the y_e axis completing the orthogonal system.

The realisation of an ECEF frame used in this work is WGS84. The choice of this frame stems from it being the datum used by the GPS system.

There are two ways of representing a position using the WGS84 datum. First there is the cartesian system using the axis defined above. Secondly a position on an ellipsoid defined in WGS84 may be used. This is the well known latitude and longitude. Together with a height above the ellipsoid a position is completely described. The relationship between the latitude(ϕ), longitude (λ), height (h) system and the cartesian system is given below (Vaníček and Steeves, 1996).

$$\begin{bmatrix} x \\ y \\ z \end{bmatrix} = \begin{bmatrix} (N+h) \cos \phi \cos \lambda \\ (N+h) \cos \phi \sin \lambda \\ \left(\frac{Nb^2}{a^2} + h \right) \sin \phi \end{bmatrix} \quad (3.1)$$

Where a and b are the semi-major axis and semi-minor axes of the ellipsoid respectively. N is given by:

$$N = \frac{a}{(1 - e^2 \sin^2 \phi)^{1/2}} \quad (3.2)$$

Where e is the eccentricity;

$$e^2 = \frac{a^2 - b^2}{a^2} \quad (3.3)$$

3.2.2 Rotation Representations

There are many ways of representing the rotation between two reference frames. Three of these are discussed in this thesis and are introduced here. Since these systems have been in use for many years much has been written on the subject. In particular (Schleppé, 1997), (Lovren and Pieper, 1998) and (Phillips et al., 2001) provide good introductions to the subject.

Direction Cosine Matrix (DCM)

The direction cosine matrix (DCM) specifies the direction of one set of axes in terms of another ('unrotated') set. A 3x3 matrix is used to define three unit vectors \hat{u} , \hat{v} and \hat{w} ;

$$A = \begin{bmatrix} \hat{u}_x & \hat{v}_y & \hat{w}_z \\ \hat{u}_x & \hat{v}_y & \hat{w}_z \\ \hat{u}_x & \hat{v}_y & \hat{w}_z \end{bmatrix} \quad (3.4)$$

Each of the elements of A is the cosine of the angle between the rotated unit vector and one of the reference axes.

The benefits of the DCM include computational simplicity and accuracy; no trigonometric functions are contained in the matrix itself. The singularities seen with the Euler angle representation also do not occur using the DCM. A series of rotations may also be represented simply by multiplying the DCMs.

The downside of the DCM is the use of 9 parameters to represent one rotation.

Euler Angles

Euler angles are perhaps the most intuitive of the rotation representations. In the 1700s Leonhard Euler showed that only three rotations were needed to represent a rotated coordinate system.

A rotation using Euler angles is a three rotation process. The first rotation is around an axis of the reference frame, the second around an intermediate axis and the third around an axis of the rotated frame. One of the major downsides to the Euler angle representation is that the order of the rotations is critical and many conventions have been proposed. In this work the so called 3-1-2 convention is adopted, this may be visualised as rotations about yaw then pitch then roll.

Each of the rotations may be represented by a DCM. As described above a series of rotations may be represented as a single DCM, the product of the individual rotation matrices. If the three rotations are through angles ϕ , Θ and Ψ the total rotation may be represented in a DCM such as this:

$$R_y^x = \begin{bmatrix} \cos \Psi \cos \phi - \sin \Psi \sin \Theta \sin \phi & \sin \Psi \cos \phi + \cos \Psi \sin \Theta \sin \phi & -\cos \Theta \sin \phi \\ -\sin \Psi \cos \Theta & \cos \Psi \cos \Theta & \sin \Theta \\ \cos \Psi \sin \phi + \sin \Psi \sin \Theta \cos \phi & \sin \Psi \sin \phi - \cos \Psi \sin \Theta \cos \phi & \cos \Theta \cos \phi \end{bmatrix} \quad (3.5)$$

If R_y^x represents the rotation from reference frame x to rotated frame y, the reverse rotation R_x^y is simply the transpose of R_y^x .

$$R_x^y = R_y^{xT} \quad (3.6)$$

By examining the elements of the DCM we can derive the Euler angles;

$$\Theta = \arcsin (R_y^x(2, 3)) \quad (3.7)$$

$$\Psi = \arctan \left(\frac{-R_y^x(2, 1)}{R_y^x(2, 2)} \right) \quad (3.8)$$

$$\phi = \arctan \left(\frac{-R_y^x(1, 3)}{R_y^x(3, 3)} \right) \quad (3.9)$$

By examining Equations 3.5 and 3.9 it can be seen that when the angle Θ is $\pi/2$ radians the denominators of Equations 3.9 and 3.8 become zero and therefore Ψ and ϕ are undefined. There is therefore a singularity encountered when using Euler angles, they are not

robust for applications where high angles might be encountered.

This singularity is the primary disadvantage to using Euler Angles. They also require trigonometric functions to be evaluated which will result in a loss of precision if many rotations are undertaken. For these reasons, as well as their intuitive nature, that Euler angles are mostly reserved for use as process inputs and outputs.

Quaternions

Quaternions are less intuitive than the Euler angle system but do give improvements in computational speed and accuracy. They also lack the singularity inherent in the Euler angle system.

The basis for the quaternion representation is Eulers rotation theorem which states that given two coordinate systems there is an invariant axis along which measurements are the same in both systems, otherwise known as the Euler Pole. It is therefore possible to move from one system to the other through a rotation about Euler Pole.

The quaternion representation uses four parameters, three to define the Euler Pole unit vector (\mathbf{e}) and one to describe the rotation around it β .

$$\mathbf{q} = \begin{bmatrix} \mathbf{e} \sin\left(\frac{\beta}{2}\right) \\ \cos\left(\frac{\beta}{2}\right) \end{bmatrix} \quad (3.10)$$

Or expanding;

$$\mathbf{q} = \begin{bmatrix} \mathbf{e}_x \sin\left(\frac{\beta}{2}\right) \\ \mathbf{e}_y \sin\left(\frac{\beta}{2}\right) \\ \mathbf{e}_z \sin\left(\frac{\beta}{2}\right) \\ \cos\left(\frac{\beta}{2}\right) \end{bmatrix} = \begin{bmatrix} q_1 \\ q_2 \\ q_3 \\ q_4 \end{bmatrix} \quad (3.11)$$

If the reference and rotated frames are parallel the quaternion reduces to;

$$\mathbf{q} = \begin{bmatrix} 0 \\ 0 \\ 0 \\ 1 \end{bmatrix} \quad (3.12)$$

At the point where $\beta = \pi$ the quaternion is;

$$\mathbf{q} = \begin{bmatrix} \mathbf{e}_x \\ \mathbf{e}_y \\ \mathbf{e}_z \\ 0 \end{bmatrix} \quad (3.13)$$

When β exceeds π radians it becomes negative. In all cases the four quaternion parameters are constrained by the equation;

$$q_1^2 + q_2^2 + q_3^2 + q_4^2 = 1 \quad (3.14)$$

A reverse rotation is represented using the inverse of the quaternion;

$$\mathbf{q}^{-1} = \begin{bmatrix} -q_1 \\ -q_2 \\ -q_3 \\ q_4 \end{bmatrix} \quad (3.15)$$

Multiple rotations can be achieved using an operation known as quaternion composition.

A rotation which may be represented using DCMs as;

$$R_z^x = R_y^x R_z^y \quad (3.16)$$

Is achieved using quaternions using;

$$\mathbf{q}_z^x = \begin{bmatrix} q_1 \\ q_2 \\ q_3 \\ q_4 \end{bmatrix}_z^x = \mathbf{q}_y^x \otimes \mathbf{q}_z^y = \begin{bmatrix} q_4 & q_3 & -q_2 & q_1 \\ -q_3 & q_4 & q_1 & q_2 \\ q_2 & -q_1 & q_4 & q_3 \\ -q_1 & -q_2 & -q_3 & q_4 \end{bmatrix}_y^x \begin{bmatrix} q_1 \\ q_2 \\ q_3 \\ q_4 \end{bmatrix}_z^y \quad (3.17)$$

Where a series of rotations is performed using orthogonal matrices such as the DCM, rounding errors will likely result in a non-orthogonal matrix which is difficult to correct. Rounding errors accumulated during quaternion composition are simply dealt with by normalising the quaternion vector using the condition given in Equation 3.12.

Problems arise when using quaternions with estimators such as non-linear least squares or the Extended Kalman Filter. Four parameters are used to describe three degrees of freedom. This leads to a variance - covariance matrix which is singular, it cannot be inverted. This problem may be overcome through the use of the pseudo-inverse but this introduces significant errors requiring normalisation of the quaternion at every iteration

(Hall *et al.*, 2008).

3.2.3 Transformations Between Reference Frames

The relationship between the ECEF Frame and the Local Level Frame

To transform a vector from the ECEF frame (\mathbf{r}_e) to the local level frame (\mathbf{r}_l) a translation and rotation is required. With the rotation expressed using a DCM (R_l^e) this can be described as:

$$\mathbf{r}_e = R_l^e \mathbf{r}_l + \mathbf{r}_{e_0} \quad (3.18)$$

Where \mathbf{r}_{e_0} is the origin of the local level frame in ECEF coordinates.

The DCM is given in terms of the latitude and longitude of the origin of the local level frame (Hofmann-Wellenhof *et al.*, 2003):

$$R_l^e = \begin{bmatrix} -\sin(\phi) \cos(\lambda) & -\sin(\lambda) & -\cos(\phi) \cos(\lambda) \\ -\sin(\phi) \sin(\lambda) & \cos(\lambda) & -\cos(\phi) \sin(\lambda) \\ \cos(\phi) & 0 & -\sin(\phi) \end{bmatrix} \quad (3.19)$$

The inverse rotation is obtained using the transpose of R_l^e .

The relationship between the Local Level Frame and the Body Frame

The relationship between the local level and body frame is key - this rotation describes the platform attitude. Since no scaling is needed and the frames share a common origin, the transformation required may be denoted as:

$$\mathbf{r}_b = R_l^b \mathbf{r}_{ll} \quad (3.20)$$

Where the DCM, R_l^b is simply derived from that given in Equation 3.5.

$$R_l^b = \begin{bmatrix} \cos \Psi \cos \phi - \sin \Psi \sin \theta \sin \phi & \sin \Psi \cos \phi + \cos \Psi \sin \theta \sin \phi & -\cos \theta \sin \phi \\ -\sin \Psi \cos \theta & \cos \Psi \cos \theta & \sin \theta \\ \cos \Psi \sin \phi + \sin \Psi \sin \theta \cos \phi & \sin \Psi \sin \phi - \cos \Psi \sin \theta \cos \phi & \cos \theta \cos \phi \end{bmatrix} \quad (3.21)$$

Angles ϕ , θ and Ψ now represent yaw, pitch and roll respectively. The euler angle singularity will therefore be encountered when the pitch reaches 90 degrees. In normal UAV flight this is unlikely, however it is not impossible and this singularity must be considered especially if a navigation system is to be used as part of a control system.

Again the reverse rotation is simply the transpose of R_l^b

The relationship between the ECEF Frame and the Body Frame

Finally we come to the transform from ECEF to body frame. Again a rotation and translation is required as in:

$$\mathbf{r}_e = R_b^e \mathbf{r}_b + \mathbf{r}_{e_0} \quad (3.22)$$

Where \mathbf{r}_{e_0} is the origin of the body frame in ECEF coordinates.

The rotation R_b^e can be expressed as the product of two rotations previously defined:

$$R_b^e = R_l^e R_b^l \quad (3.23)$$

Attitude Determination From ECEF Coordinates

To obtain attitude values from a baseline vector in the ECEF frame first the baseline is rotated to the local level frame. This is done using the DCM R_l^e given in Equation 3.19.

The heading, pitch and roll of the sensor frame may now be determined using basic trigonometric functions and the baseline coordinates in the local level frame. This is then corrected to the body frame using the boresight / lever arm calibration.

When defining the DCM R_l^e the latitude and longitude of the origin of the local level frame is needed. As described before this is defined as the centre of gravity of the platform. The estimate of this location will always have some error associated with it and this error will propagate to the DCM. The magnitude of this error is dependent on the latitude and longitude of the platform but will not be significant if the position error is kept small. It is likely to become significant only in high accuracy situations where the position error exceeds 1km.

In this work this situation is avoided by using the position of one of the antenna obtained using stand alone GPS positioning.

3.3 Functional Models

This section introduces the functional models and processes used to estimate the platform attitude from the GNSS pseudorange and carrier phase measurements. Many models have been proposed, a selection of which are introduced and discussed.

3.3.1 The Spherical Polar Functional Model

One approach involves re-parameterising the baseline in spherical polar coordinates. It is assumed that the baseline length between antennas is known from a survey. In spherical

polar coordinates this information is naturally used since the coordinate is parameterised in terms of two angles α , β and the baseline length, l (*Teunissen, 2006*).

$$b([\alpha, \beta]^T) = l \cdot \begin{vmatrix} \cos \alpha \cos \beta \\ \cos \alpha \sin \beta \\ \sin \alpha \end{vmatrix} \quad (3.24)$$

The GNSS observation equations are adapted to the spherical polar parametrisation and the weighted non-linear least squares estimate for $\delta\alpha$ and $\delta\beta$ is obtained at each iteration.

The reference frame chosen may either be ECEF or local level. If the ECEF frame is chosen the converged estimate for α and β must be rotated to the local level frame through the use of the rotation described in Equation 3.19.

Alternatively the pitch and heading angles may be estimated directly in the local level frame as described in (*Hide et al., 2007*) and (*Schlepppe, 1997*).

The primary disadvantage of this approach, and the reason it is not adopted in this work, is the requirement for a good initial estimate of the attitude.

The spherical polar parametrisation of the baseline leads to more non-linear observation equations than the cartesian approach. In order to ensure convergence to the correct solution a sufficiently accurate initial estimate of the baseline is required. This requires complimentary sensors to be used (eg an aligned inertial navigation system) or requires the system to be initialised in a known orientation.

In addition the spherical polar parametrisation also requires accurate and precise knowledge of the baseline length. Any error in this measurement will propagate into the attitude estimates.

3.3.2 The Constrained Functional Model

Again it is assumed that the coordinates of the antennas are known in the sensor and body frames. Note that the cartesian inter-antenna baseline in the ECEF frame, x_e is related to the inter-antenna baseline in the body frame, x_b by:

$$x_e = R_b^e x_b + x_{e0} \quad (3.25)$$

Given x_b and an estimate of x_{e0} we can now choose to estimate either x_e or R_b^e .

If we choose to estimate the rotation matrix R_b^e the solution will be constrained by the properties of the rotation matrix, namely that it must be orthogonal; $R_b^e (R_b^e)^T = I$.

The disadvantage of this approach, and again the reason that it is not used in this work is that it requires a good estimate of the rotation matrix R_b^e in order for the non-linear least squares or EKF estimator to converge.

3.3.3 The Unconstrained Functional Model

In this work the choice is made to solve for the inter-antenna vector in cartesian coordinates x_e . By rotating the ECEF vector obtained into the local level frame we may directly determine the attitude as described in Section 3.2.3.

This approach does not require knowledge of the inter-antenna baseline and a simple initial assumption that all of the antennas are collocated is enough for stable estimator performance.

Using this method allows use of a mathematical model identical to that used in standard positioning applications. The primary difference is that the reference, or ‘base’, antenna is allowed to roam and if the platform is in motion a new reference position is needed every epoch.

Adapting the standard positioning method means that the model does not intrinsically include available information on the baseline length. Later in this chapter the baseline length constraint is included such that the solution satisfies;

$$\|b\| = \sqrt{b^T b} = l \quad (3.26)$$

Where $\|\cdot\|$ is the Euclidean norm, b is the baseline vector and l is the baseline length. This constraint will be further explored in Section 3.8.

We must now determine the baseline components from the observation equations 2.12. To achieve this we use the estimators introduced in Section 2.7.

First we define the linearised functional model $\delta\mathbf{A}(x_0)$. The observation equations are linearised about an initial estimate of the baseline components. In this work the initial estimate of the baseline has been taken to be $\|b\| = 0$.

From Equation 2.21 the functional model has components;

$$\delta a_i(b_0) = \frac{d}{dx} f(b_0) \quad (3.27)$$

Using the double difference code observation Equation 2.13 we have:

$$\delta a_i(b_0) = \frac{d}{db} \nabla \Delta PR_{ab}^{ij} \quad (3.28)$$

For each of the baseline components x , y and z we therefore have a partial derivative of the form;

$$\frac{\delta}{\delta x_b} \nabla \Delta PR_{ab}^{ij} = \frac{\delta \nabla \Delta \rho_{ab}^{ij}}{\delta x_b} = \left[\frac{X^i - x_{0a}}{\rho_a^i} + \frac{X^j - x_{0a}}{\rho_a^j} + \frac{X^i - x_{0b}}{\rho_b^i} - \frac{X^j - x_{0b}}{\rho_b^j} \right] \quad (3.29)$$

Where X^i is the x component of the position of satellite i and x_{0a} , x_{0b} are the initial estimates of the x component of the position of receivers a and b .

For each double difference code observation we now have;

$$\delta\mathbf{A} = \left| \begin{array}{ccc} \frac{\delta\nabla\Delta PR_{ab}^{ij}}{\delta x_b} & \frac{\delta\nabla\Delta PR_{ab}^{ij}}{\delta y_b} & \frac{\delta\nabla\Delta PR_{ab}^{ij}}{\delta z_b} \end{array} \right| \quad (3.30)$$

In forming the linearised functional model for the double difference carrier phase observations we modify the code functional model to include terms for the integer ambiguities.

$$\frac{\delta\nabla\Delta\phi_{ab}^{ij}}{\delta a_{ab}^{ij}} = 1 \quad (3.31)$$

Therefore for each carrier phase observation:

$$\delta\mathbf{A} = \left| \begin{array}{ccc} \frac{\delta\nabla\Delta PR_{ab}^{ij}}{\delta x_b} & \frac{\delta\nabla\Delta PR_{ab}^{ij}}{\delta y_b} & \frac{\delta\nabla\Delta PR_{ab}^{ij}}{\delta z_b} & 1 \end{array} \right| \quad (3.32)$$

In the case where four satellites are being tracked we have six double difference observations (three code and three carrier phase);

$$\delta\mathbf{A} = \begin{pmatrix} \frac{\delta\nabla\Delta PR_{ab}^{ij}}{\delta x_b} & \frac{\delta\nabla\Delta PR_{ab}^{ij}}{\delta y_b} & \frac{\delta\nabla\Delta PR_{ab}^{ij}}{\delta z_b} & 0 & 0 & 0 \\ \frac{\delta\nabla\Delta PR_{ab}^{ik}}{\delta x_b} & \frac{\delta\nabla\Delta PR_{ab}^{ik}}{\delta y_b} & \frac{\delta\nabla\Delta PR_{ab}^{ik}}{\delta z_b} & 0 & 0 & 0 \\ \frac{\delta\nabla\Delta PR_{ab}^{im}}{\delta x_b} & \frac{\delta\nabla\Delta PR_{ab}^{im}}{\delta y_b} & \frac{\delta\nabla\Delta PR_{ab}^{im}}{\delta z_b} & 0 & 0 & 0 \\ \frac{\delta\nabla\Delta\phi_{ab}^{ij}}{\delta x_b} & \frac{\delta\nabla\Delta\phi_{ab}^{ij}}{\delta y_b} & \frac{\delta\nabla\Delta\phi_{ab}^{ij}}{\delta z_b} & 1 & 0 & 0 \\ \frac{\delta\nabla\Delta\phi_{ab}^{ik}}{\delta x_b} & \frac{\delta\nabla\Delta\phi_{ab}^{ik}}{\delta y_b} & \frac{\delta\nabla\Delta\phi_{ab}^{ik}}{\delta z_b} & 0 & 1 & 0 \\ \frac{\delta\nabla\Delta\phi_{ab}^{im}}{\delta x_b} & \frac{\delta\nabla\Delta\phi_{ab}^{im}}{\delta y_b} & \frac{\delta\nabla\Delta\phi_{ab}^{im}}{\delta z_b} & 0 & 0 & 1 \end{pmatrix} \quad (3.33)$$

We finally define the observed minus computed observations from Equation 2.22

$$l = \nabla\Delta\phi_{ab}^{ij} - \rho_{ab}^{ij}(b_{a0}, b_{b0}) \quad (3.34)$$

3.4 Pre-Processing

Before the differenced observations can be formed and the estimators used, the satellite positions must be calculated and the stochastic model created.

3.4.1 Satellite Position Computation

The procedure used to compute the satellite positions can be found in the GPS Interface control Document (ICD) and is therefore not reproduced here.

The procedure takes as its input the orbit parameters obtained from the satellites navigation message and an estimate of the time of signal transmission.

Errors in the estimate of the time of signal transmission will result in an error in the resulting position calculation. For high quality receivers the receiver clock is steered to remain close to true GPS time. In this case the error due to the receivers clocks can be considered to be negligible compared to the other parts of the ephemeris error. Most low cost receivers allow their clock to drift from GPS time significantly. The clocks of two receivers may differ by many milliseconds.

In this work the time of signal transmission (T^s) is taken as the receiver's estimate of the time of reception (T_r) minus the observed code pseudorange scaled to time.

$$T^s = T_r - (cPR_r^s) \quad (3.35)$$

The receiver clock offset is the dominant error source in the pseudorange. By estimating the time of transmission using the pseudorange the receiver clock offset is therefore taken into account along with the signal transit time due to the geometric range.

This process is used to obtain a satellite position for each observation from each receiver.

3.4.2 Stochastic Model

The stochastic models used in this work are obtained using the elevation dependent model introduced in Section 2.8.

It is assumed that the code and carrier phase observations are uncorrelated so that:

$$\mathbf{Q}_y = \begin{vmatrix} \mathbf{Q}_{y(PR)} & 0 \\ 0 & \mathbf{Q}_{y(\phi)} \end{vmatrix} \quad (3.36)$$

This model is then used to weight the code and carrier phase observations, $\mathbf{W} = \mathbf{Q}_y^{-1}$.

3.5 The Float Solution

Using the estimators introduced in Section 2.7.1 and the functional model from Section 3.3.3, an estimate of the baseline parameters may now be made.

Using Equation 2.24 we have:

$$\hat{b} = b_0 + (\delta\mathbf{A}(b_0))^T \mathbf{W} \delta\mathbf{A}(b_0) (\delta\mathbf{A}(b_0))^T \mathbf{W} l \quad (3.37)$$

And the estimate \hat{b} has variance - covariance:

$$\mathbf{Q}_{\hat{b}} = ((\delta\mathbf{A}(b_0))^T \mathbf{Q}_y^{-1} (\delta\mathbf{A}(b_0)))^{-1} \quad (3.38)$$

The state vector \hat{b} contains updates to the initial state estimates b_0 and if double difference carrier phase observations are used, a_0 .

The estimates for the baseline components are not constrained with the *a priori* knowledge of the baseline characteristics. The estimates for the ambiguities a are allowed to take any real value, not constrained to integers. For these reasons the float solution is not the most precise or robust available.

3.6 The Fixed Solution

If the integer ambiguities can be estimated from the float solution then the estimated baseline can be improved with this knowledge.

If the integer ambiguities are \check{a} then;

$$\check{b} = \hat{b} - Q_{\hat{b}\hat{a}}Q_{\hat{a}}^{-1}(\hat{a} - \check{a}) \quad (3.39)$$

And;

$$Q_{\check{b}} = Q_{\hat{b}} - Q_{\hat{b}\hat{a}}Q_{\hat{a}}^{-1}Q_{\hat{a}\hat{b}} \quad (3.40)$$

The ‘fixed baseline’ \check{b} uses the full precision of the double difference carrier phase observable. If the ambiguities are fixed correctly there will be little improvement to be had in the solution by including the *a priori* baseline knowledge.

3.7 The Choice of Baseline Length and Antenna Location

The precision of the attitude parameters which may be derived from an ambiguity fixed baseline will vary greatly with baseline length. For a given baseline precision the precision of the attitude parameter estimates will decrease with baseline length.

It follows that to maximise the precision of the attitude parameters the baseline length must be maximised with the practical limits of the platform. Suitable antenna locations on the UAV include the wingtips, nose and tail.

All of these locations are very sensitive to weight since they exert a large lever force around the UAV centre of gravity. To minimise lever forces the receivers should be mounted away from the antennas, in the main payload and as close to the UAV centre of gravity as possible.

3.8 Using the Baseline Constraints

It is possible to modify the ambiguity resolution process and the unconstrained float solution to include the *a priori* baseline knowledge. This section will develop a method used to constrain the float solution and introduce a modification to the LAMBDA method for ambiguity fixing.

3.8.1 Baseline Constrained Float Solution

In Section 3.5 the unconstrained float estimates \hat{b} and \hat{a} were obtained. We aim to constrain the float baseline solution using *a priori* knowledge of the baseline length. This is a quadratically constrained least squares problem. For convenience the constraint Equation 3.26 is presented again here;

$$\|b\| = \sqrt{b^T b} = l \quad (3.26)$$

The quadratically constrained least squares problem is one of finding a value for b which satisfies;

$$\min \|\hat{b}(a) - b\|_{Q_{\hat{b}(a)}}^2 \quad (3.41)$$

Subject to Equation 3.26.

The value for b which satisfies 3.41 is known as the constrained float solution and denoted \hat{b}_l .

As per (Teunissen, 2006) the problem is approached using lagrange multipliers. The constraint equation 3.26 is a sphere of radius 1. The objective function 3.41 can be put in the form of an ellipse with:

$$\|\hat{b}(a) - b\|_{Q_{\hat{b}(a)}}^2 = k^2 \quad (3.42)$$

At the point at which the sphere and ellipse touch we will find the constrained solution for b . At this point the gradient of the sphere and ellipse will be parallel and one will be a scaled version of the other. The symbol ∇ is used at this point to denote a gradient.

$$\nabla \|\hat{b}(a) - b\|_{Q_{\hat{b}(a)}}^2 = \lambda \nabla \|b\|_{I_3} \quad (3.43)$$

Rearranging we achieve the normal equations in the form $Ax - \lambda x = c$:

$$(Q_{\hat{b}(a)}^{-1} - \lambda I_3)b = Q_{\hat{b}(a)}^{-1} \hat{b}(a) \quad (3.44)$$

The smallest value for λ will yield the solution for b since this will be the point at which the ellipse first touches the sphere. With this in mind the solution to the problem 3.44 is:

$$\hat{b}_l = (Q_{\hat{b}(a)}^{-1} - \lambda I_3)^{-1} c \quad (3.45)$$

With:

$$c = Q_{\hat{b}(a)}^{-1} \hat{b} \quad (3.46)$$

We find λ by reformulating 3.44 as a quadratic eigenvalue problem of the form (*Meerbergen and Tisseur, 2001*):

$$\begin{aligned}(\lambda^2 M + \lambda C + K)x &= 0 \\ y^*(\lambda^2 M + \lambda C + K) &= 0\end{aligned}$$

Where x and y are eigenvectors and λ is an eigenvalue.

First note that from equations 3.45 and 3.26 we can say that:

$$(Q_{\hat{b}(a)}^{-1} - \lambda I)^2 y = c \quad (3.47)$$

And that:

$$c^T y = l^2 \quad (3.48)$$

With;

$$y = (Q_{\hat{b}(a)}^{-1} - \lambda I)^{-2} c$$

Rearranging 3.47 and 3.48 we form the symmetric quadratic eigenvalue problem;

$$\left(\lambda^2 I_3 - 2\lambda Q_{\hat{b}(a)}^{-1} + (Q_{\hat{b}(a)}^{-2} - l^{-2} c c^T) \right) y = 0 \quad (3.49)$$

Standard methods may now be used to find the eigenvalues of 3.49. The smallest eigen-

value is the λ required to complete Equation 3.45 for \hat{b}_l .

Once the constrained float baseline solution has been found, the constrained float ambiguity solution follows as:

$$\hat{a}_l = \hat{a} - Q_{\hat{a}\hat{b}} Q_{\hat{b}}^{-1} (\hat{b} - \hat{b}_l) \quad (3.50)$$

With associated covariance matrix ;

$$Q_{\hat{a}_l} = Q_{\hat{a}} - Q_{\hat{a}\hat{b}} \hat{b}_l (\hat{b}_l^T Q_{\hat{b}} \hat{b}_l)^{-1} \hat{b}_l^T Q_{\hat{b}\hat{a}} \quad (3.51)$$

3.8.2 Baseline Constrained LAMBDA

The *a priori* baseline knowledge may also be used to modify the objective function of the lambda process. Either the baseline constraint can be transformed to the ambiguity domain as in (Monikes et al., 2005) or the LAMBDA process can be modified via the use of an auxiliary search space. In this work the second approach is taken since it takes full advantage of the efficiency of the LAMBDA search method.

Recall from Section 2.9.3 the objective function of the standard LAMBDA process is:

$$\check{\alpha} = \min_{a \in Z^n} \|(\hat{a} - a)\|_{Q_{\hat{a}}}^2 \quad (2.38)$$

Following (Teunissen, 2006) we now include a term to include the baseline length constraint:

$$\check{\alpha} = \min_{a \in Z^n, b \in R^3} \left(\|(\hat{a} - a)\|_{Q_{\hat{a}}}^2 + \|\check{b}_l(a) - \check{b}(a)\|_{Q_{\check{b}_l}}^2 \right) \quad (3.52)$$

Where $\check{b}_l(a)$ is the fixed baseline solution obtained using integer ambiguities a and constrained to the baseline length l . It is obtained by solving the quadratic least squares problem as described as above (Section 3.8.1) substituting the fixed baseline $\check{b}(a)$ for the float baseline.

The quantity we seek to minimise in Equation 2.38 is now the sum of two parts. First is the distance of the fixed ambiguity to the float ambiguity in the metric of the float ambiguity variance - covariance matrix (as in the unconstrained LAMBDA process). Second is the distance of the fixed baseline to a constrained version of itself in the metric of the fixed baseline variance - covariance matrix.

This new objective function requires a modification to the integer search procedure. Recall that in the standard LAMBDA process a search space is chosen using the bootstrapped estimate of the fixed ambiguity vector. All candidates within this distance of the float solution are returned and the one closest to the float solution is the chosen candidate. If \check{a}_b are the bootstrapped ambiguities then this search space is;

$$\Psi(\chi^2) = \{\|(\hat{a} - \check{a}_b)\|_{Q_{\hat{a}}}^2 \leq \chi^2\} \quad (3.53)$$

With the new objective function 2.38 we can define a new search space;

$$\Psi(\chi_b^2) = \{\|(\hat{a} - \check{a}_b)\|_{Q_{\hat{a}}}^2 + \|\check{b}_l(\check{a}_b) - \check{b}(\check{a}_b)\|_{Q_{b_l}}^2 \leq \chi_b^2\} \quad (3.54)$$

This new search space is no longer simply elliptical as we had in Equation 3.53. The new shape is inefficient to search for candidates for \check{a} and so we define an auxiliary elliptical search space:

$$\Psi_0(\chi_b^2) = \{\|(\hat{a} - \check{a}_b)\|_{Q_{\hat{a}}}^2 \leq \chi_b^2\} \quad (3.55)$$

The new space is larger than $\psi(\chi_b^2)$ but is elliptical and can be searched using the same methods as in the standard LAMBDA process, including the Z transformation.

The downside of using the auxiliary elliptical search space $\psi_0(\chi_b^2)$ is that each returned candidate for \check{a} must be checked to see if it satisfies the inequality;

$$\chi_b^2 - \|(\hat{a} - a)\|_{Q_{\hat{a}}}^2 \geq \|\check{b}_l(a) - \check{b}(a)\|_{Q_{\check{b}_l}}^2 \quad (3.56)$$

This requires the solution of the quadratically constrained least squares problem in Equation 3.41 for each candidate. Those which meet the inequality lie within $\psi(\chi_b^2)$ and that which returns the solution to 3.52 is the chosen fixed ambiguity \check{a} .

For the imprecise float solutions available from low cost, single frequency systems the search space $\psi_0(\chi_b^2)$ will be large and the number of candidates within it will be very large, making the use of 3.56 impractical. For this reason, in this work the ‘search and expand’ method is used, as developed by Teunissen in (Teunissen, 2006).

In this approach the solution of the quadratically constrained least squares problem for every candidate is avoided by recognising that:

$$\|(\hat{a} - a)\|_{Q_{\hat{a}}}^2 + \|\check{b}_l(a) - \check{b}(a)\|_{Q_{\check{b}_l}}^2 \geq \|(\hat{a} - a)\|_{Q_{\hat{a}}}^2 + \lambda_{min} (\|\hat{b}(a)\|_{I_3}^2 - l)^2 \quad (3.57)$$

Where λ_{min} is the smallest eigenvalue of $Q_{\hat{b}(a)}^{-1}$. The expression to the right of the inequality is used to form a third search space:

$$\psi_1(\chi^2) = \{\|(\hat{a} - a)\|_{Q_{\hat{a}}}^2 + \lambda_{min} (\|\hat{b}(a)\|_{I_3}^2 - l)^2 \leq \chi^2\} \quad (3.58)$$

Three search spaces are now available, $\psi_0(\chi^2)$ the auxiliary search space without a baseline element, $\psi_1(\chi^2)$ which does not require solution of the quadratically constrained

least squares problems and $\psi(\chi^2)$ which is the original constrained LAMBDA search space. The search and expand procedure is depicted in Figure 3.4.

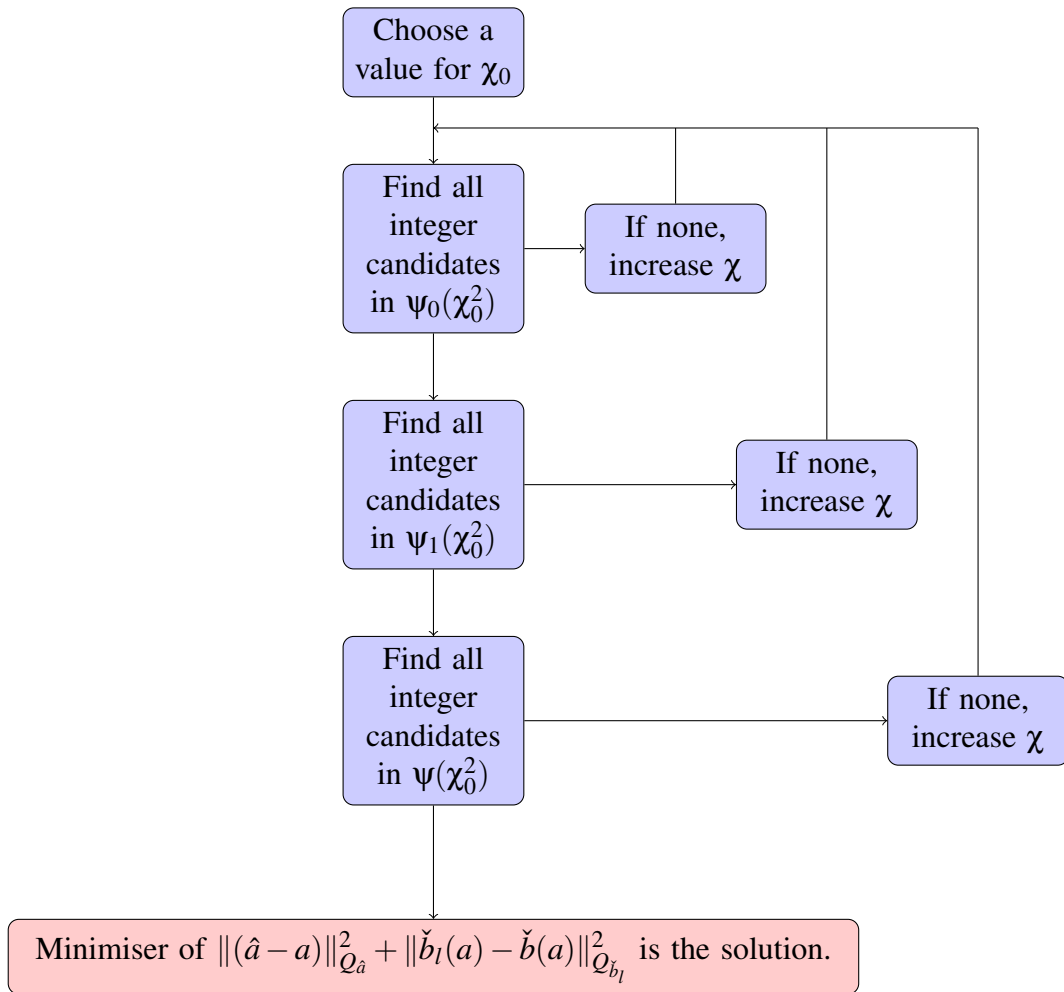


Figure 3.4: The ‘search and expand’ approach.

The quadratically constrained least squares problem is solved only for the first candidates which appear in $\psi(\chi^2)$. In this work the initial value for χ_0 is obtained using the bootstrapped estimate for \check{a}_b , $\chi_0 = \|\hat{a} - \check{a}_b\|_{Q_a}^2$.

3.8.3 Integer Ambiguity Validation

The *a priori* baseline length knowledge can also be used to validate an integer ambiguity candidate. The ratio test method introduced in Section 2.9.4 requires at least two candidates from the estimator, only the LAMBDA or constrained LAMBDA methods can deliver this. In this section a validation method is developed which can be used with any estimator - rounding, bootstrap or LAMBDA based.

Using the linearised law of propagation of variances the variance of the fixed baseline length may be found using Equation 3.59 .

$$\sigma_{|b|}^2 = A Q_b A^T \quad (3.59)$$

Where:

$$A = \left[\frac{\delta F(x, y, z)}{\delta x} \quad \frac{\delta F(x, y, z)}{\delta y} \quad \frac{\delta F(x, y, z)}{\delta z} \right] \quad (3.60)$$

And:

$$F(x, y, z) = \sqrt{(x - x_0)^2 + (y - y_0)^2 + (z - z_0)^2} \quad (3.61)$$

So:

$$\begin{aligned}
\frac{\delta F(x, y, z)}{\delta x} &= -\frac{x - x_0}{x} \\
\frac{\delta F(x, y, z)}{\delta y} &= -\frac{y - y_0}{y} \\
\frac{\delta F(x, y, z)}{\delta z} &= -\frac{z - z_0}{z}
\end{aligned}
\tag{3.62}$$

If the fixed baseline length $|\check{b}|$ and the *a priori* measurement of the baseline length are normally distributed then so will their difference $\Delta | b |$ be:

$$\Delta | b | = N(\Delta | b |, \sigma_{\Delta | b |}^2) \tag{3.63}$$

With:

$$\sigma_{\Delta | b |} = \sqrt{\sigma_l^2 + \sigma_{|\check{b}|}^2} \tag{3.64}$$

Where l is the *a priori* baseline length measurement. Finally, the probability that the baseline length difference ($\Delta | b |$) is smaller than the measured baseline length difference ($\Delta | \check{b} |$) is:

$$P(\Delta | \check{b} | < \Delta | b |) = \text{erf} \left[\frac{\Delta | b | / \sigma_{\Delta | b |}}{\sqrt{2}} \right] \tag{3.65}$$

Where *erf* is the Gauss error function.

It is now straightforward to obtain the probability that the baseline length difference

$(\Delta | b |)$ is larger than the measured baseline length difference $(\Delta | \check{b} |)$.

$$P(\Delta | \check{b} | > \Delta | b |) = 1 - \text{erf} \left[\frac{\Delta | b | / \sigma_{\Delta | b |}}{\sqrt{2}} \right] \quad (3.66)$$

A threshold probability is now chosen, above which the fixed baseline is taken to be the same as the *a priori* baseline and below which it is taken to be different and the fixed ambiguity candidate rejected.

3.9 Conclusion

In this chapter the models and concepts required to perform GPS Attitude determination have been introduced.

The reference frames and rotation representations used in this work have been described and their interrelationships explored. The intuitive nature of Euler angle representation has led to it being selected as suitable for system input and output. Transformations between reference frames are performed using the Direction cosine Matrix (DCM).

Next functional models for use in the estimators GNSS model have been discussed. The unconstrained cartesian parametrisation has been selected as the most suitable for this work primarily because *a priori* knowledge of the attitude is not required. This functional model is also more tolerant of variations in the baseline length due to errors in *a priori* measurement or flexing of the UAV structure.

The chapter went on to introduce a procedure for determining the unconstrained float and fixed ambiguity solutions. The pre-processing and hardware layout requirements were discussed. Emphasis was placed on the importance to this work of accounting for the poor performance of the low cost receiver clocks in the pre-processing stage.

Finally adaptations to the unconstrained float solution and the LAMBDA method were

introduced to include *a priori* information on baseline length.

The float solution was constrained by finding the solution to a quadratically constrained least squares problem. The quadratically constrained least squares problem was transformed into a quadratic eigenvalue problem (QEP) through the use of lagrange multipliers. The QEP can be can be efficiently and robustly solved leading to an estimate for the constrained float baseline.

The objective function of the LAMBDA method was modified to include a term which accounts for the known baseline length. A search method was introduced which gives an efficient search without the need to solve the quadratically constrained least squares problem for a large number of candidates. The use of the constrained float solution and the modified LAMBDA process is expected to provide the most robust GNSS attitude solution available.

Finally a validation method based on the *a priori* baseline length knowledge was developed. The method is equally valid for use with all estimators and so will be particularly useful when using the bootstrap estimator, for which no validation technique was previously available.

This thesis now moves on to testing these techniques in Chapter 4.

Chapter 4

Testing GNSS Attitude Determination

4.1 Introduction

The purpose of this chapter is to test the methods introduced in Chapters 2 and 3. The analysis will focus on the system performance with regard to the mini-UAV application. Of particular interest is the accuracy, precision and robustness of the attitude estimates.

The experimental setups used in this work will first be introduced. Zero baseline, short baseline, static and kinematic trials have been performed and their purposes are discussed. GPS measurements made on a mini-UAV platform will also be examined to identify problems caused by real world mini-UAV flight.

For this work GPS measurements have been made using a low cost receiver with radio frequency input from low cost antennas and a GPS hardware simulator. The hardware simulator provides a controllable environment to test the receiver performance while the low cost antenna trials are essential to examine the techniques in the environment in which they will be used.

Since successful integer ambiguity resolution is key to obtaining a GNSS attitude solution the performance of the estimators is quantified in terms of the number of independent measurement epochs in which the integer ambiguities are successfully resolved. The

effect of different measurement environments is quantified.

The outcome of an integer ambiguity estimator must be validated and the use of the LAMBDA ratio test and baseline length information is examined in this chapter.

In this work the ‘accuracy’ of the attitude estimates refers to the difference between the estimate and an accepted ‘truth’ estimate. The precision describes the degree of repeatability of the estimate, it relates to the distribution of the errors in the attitude estimates. In this work the precision is quantified in terms of the standard deviation. For complete definitions refer to (*Isaacs, 2000*).

Attitude accuracy and precision statistics are difficult to obtain from the literature (see Chapter 1). For this reason they will be examined using both real and simulated receiver inputs.

Next real GPS measurements made using low cost equipment on a mini-UAV are analysed. The rate of cycle slips and loss of lock incidents are used to examine the performance of the GPS receivers tracking loops in the highly dynamic UAV environment. Problems with the data are identified and quantified.

Finally a flight profile which replicates the problems observed in the real UAV data is generated using the hardware simulator. In this controlled environment the receiver response to dynamic inputs can be examined.

For each set of results a short discussion is given at the end of the section. All of the results in this chapter were obtained using the non-linear least squares estimator with code and phase variances of 0.75m and 3mm respectively. Observations were weighted using the elevation model given in Section 2.8.

4.2 Experimental Setup

4.2.1 Zero Baseline Testing

Zero baseline tests use two receivers connected to the same antenna. A splitter is used to feed the same radio frequency input to both receivers. In this work an ALDCBS1X2 Amplified L1/L2 splitter from GPS Networking Inc. was used.

Zero baseline tests are useful for examining the noise performance of the receiver / antenna combination. All other biases should be completely cancelled in the double differencing process.

This style of test allows the trivial recovery of the integer ambiguities. For convenience the double difference carrier phase observation equation is reproduced here:

$$\lambda \nabla \Delta \phi_{ab}^{ij} = \nabla \Delta \rho_{ab}^{ij} + \lambda \nabla \Delta N_{ab}^{ij} - \varepsilon(\nabla \Delta \phi) \quad (2.12)$$

In a zero baseline test the geometric range component $\nabla \Delta \rho_{ab}^{ij}$ will be zero. The carrier phase noise $\varepsilon(\nabla \Delta \phi)$ is expected to be a small fraction of a cycle so the ambiguities can be reliably estimated using:

$$\nabla \Delta N_{ab}^{ij} = \left[\nabla \Delta \phi_{ab}^{ij} \right] \quad (4.1)$$

Where $[\cdot]$ is used to denote the nearest integer rounding operation.

4.2.2 Short Baseline Testing

Static short baseline tests replicate the GNSS attitude layout. Two receivers are connected to two antennas on a short, known, baseline length.

In this work a 1m baseline has been used. This is to replicate the typical baseline length available on a mini-UAV. Increasing this baseline length up to ≈ 100 m will not have a significant effect on the decorrelation of the double difference error sources.

4.2.3 Hardware Simulator Testing

Hardware simulator testing provides a controlled environment in which to examine the performance of the GNSS attitude system.

In this work a Spirent GSS8000 hardware simulator was used. The hardware simulator provides a radio frequency signal which emulates that which would be received by an antenna following the simulated trajectory. It allows testing in different dynamic environments while using the same GPS constellation and atmospheric conditions.



Figure 4.1: Spirent GSS8000 Multi-GNSS Hardware Simulator

For this research the scenarios modelled in the hardware simulator were setup to closely replicate those in the ‘real world’ tests, without the effects of multipath and antenna phase centre variation. The same GPS constellations were simulated with atmospheric effects modelled by the hardware simulator.

One major advantage of the hardware simulator is the availability of the precise simulated

trajectory. This allows examination of the accuracy and precision of the attitude solution in three dimensions for both dynamic and static tests.

4.2.4 UAV Flights

For this research GPS measurements were made onboard a K70 mini-UAV flying a survey payload.

The K70 mini-UAV is a 1.8m wingspan UAV which weighs 5kg including payload. It was developed to test the feasibility of performing aerial surveys using UAVs. It is powered by a 10cc internal combustion engine and flies at speeds of $10\text{-}30\text{m s}^{-1}$. Control inputs come from a human pilot via a radio frequency control link.



Figure 4.2: K70 mini-UAV

For the flight trials used in this work the K70 was flying a survey payload consisting of one uBlox GPS receiver, a Crossbow IMU440 inertial measurement unit, a digital camera and datalogging equipment. Flights were all conducted within visual range of the pilot. The regulation and operation of the K70 UAV are discussed in Appendix A. Its payload is described in Appendix B.

The purpose of using the single receiver GPS data in this work is to examine the tracking performance of a low cost GPS receiver / antenna in a real mini-UAV environment.

4.3 Zero Baseline Test Results

In this section the results of simulated and real zero baseline tests are presented. The purpose of these tests is to quantify the effect of noise in the receiver / antenna combinations and examine the effects of linear acceleration and velocity on the observables.

4.3.1 Solution Accuracy & Precision

The results of processing data collected on a zero baseline are presented in Table 4.1. Since the attitude solution is undefined for a zero length baseline, the accuracy and precision have been determined by measuring the distance from the origin in metres.

‘Real’ data refers to that obtained using uBlox LEA-5T receivers and an Onshine patch antenna in an open sky environment. ‘Simulated’ data is that collected using a uBlox LEA-5T receiver and the hardware simulator. In all cases the statistics were derived using around 4000 measurement epochs.

Firstly static testing gives data free from the effects of dynamics. The receiver tracking loops should perform consistently throughout and all available satellites should be tracked at every epoch.

Table 4.1: Static Zero Baseline Results

Solution Type	Real		Simulated	
	Accuracy	σ	Accuracy	σ
Float	0.10 m	0.52 m	0.03 m	0.59 m
Fixed	45 μm	2.6 mm	6.9 μm	3.1 mm

The hardware simulator was also used to make measurements on a kinematic zero baseline. The purpose of this test was to examine the effect of platform dynamics on the

accuracy and precision of the results. It is expected that dynamics will decrease the precision of the GPS observables due to the changes required in the receiver tracking loops (see Section 2.4.6).

The trajectory simulated was level and straight with repeated acceleration and constant velocity phases. The results are given in Table 4.2 ;

Table 4.2: *Kinematic Zero Baseline Results*

Simulated		
Solution Type	Accuracy	σ
Float	0.07 m	0.57 m
Fixed	1.3 μm	3.6 mm

Discussion

The data in Table 4.1 shows that the majority of the noise in the solution arises from the receiver electronics rather than the antenna. The low cost antenna used for the ‘real world’ trial could be expected to add to the system noise but these results indicate that this is not the case.

The ‘real world’ data do show greater biases than the simulated data. While not large compared to the precision, a float bias of 0.1 m is unexpected. This may be due to residual errors in the double difference observables caused by the measurements being made at slightly different times (see Section 3.4). In particular the multipath signals could be expected to vary over the time between the receivers measurements.

In data used for this research the difference between the receiver’s clocks has been observed to be up to 7 milliseconds. Since multipath is difficult to model in kinematic applications this bias will be best mitigated by using antennas with ground planes. However as discussed in Section 2.4.3 this is not practical on the mini-UAV. The observed bias may therefore be unavoidable when using low cost, low mass equipment.

Finally the kinematic data in Table 4.2 show good agreement with the static simulated data. Millimetre level biases in the float and fixed solutions do appear during periods of platform acceleration but subside rapidly once the acceleration ceases. No significant increase in noise, or corresponding decrease in precision was observed.

4.3.2 Ambiguity Resolution

Since ambiguity resolution is required for attitude determination, the success rate of integer ambiguity resolution using the methods described in 2.9 and 3.8 is now examined. The fixed ambiguities determined using Equation 4.1 are taken to be correct and used for comparison in this section.

The constrained float is not used in this section since the constrained solution will always be the sought after baseline and integer ambiguity.

The mean value for χ^2 (size of the integer least squares search space) and number of candidates in the search is given for the LAMBDA and constrained LAMBDA methods. The number of candidates in the search is particularly relevant to processing times in real time applications.

Table 4.3: Simulated Static Zero Baseline Results

Ambiguity Fixing Method	Success %	χ^2	No. Candidates in search
Bootstrap	5.12	-	-
Bootstrap with Z transform	84.67	-	-
LAMBDA	88.56	0.11	3.17
Constrained LAMBDA	100	0.45	182

Table 4.4: 'Real' Static Zero Baseline Results

Ambiguity Fixing Method	Success %	χ^2	No. Candidates in search
Bootstrap	0.96	-	-
Bootstrap with Z transform	90.83	-	-
LAMBDA	92.82	0.10	3.24
Constrained LAMBDA	98.41	0.58	758

Table 4.5: Simulated Kinematic Zero Baseline Results

Ambiguity Fixing Method	Success %	χ^2	No. Candidates in search
Bootstrap	5.25	-	-
Bootstrap with Z transform	85.37	-	-
LAMBDA	88.16	0.11	3.16
Constrained LAMBDA	100	0.45	204

Discussion

All of the ambiguity resolution results demonstrate the effectiveness of using the Lambda Z transform. Improvements in the bootstrap success rate of 80-90% are observed when using the transformed ambiguities.

The unmodified LAMBDA method shows good success rates with few candidates searched compared to the constrained version. The requirement to examine hundreds of ambiguity candidates and compute baselines / constrained baselines for them all is a large computational overhead. The Constrained LAMBDA process does however show near perfect success rates.

Little difference is observed in the success rates between static and kinematic data from the simulator. The biases in the 'real world' float data however cause a large change in the size of the constrained LAMBDA search space. This has a negligible impact on the overall success rate but does add to the computational burden.

The data indicate that the success rate of the LAMBDA and even bootstrap methods may be sufficient without the computational burdens of the constrained version.

4.4 Short Baseline Test Results

Results are now presented from measurements made over a small baseline, nominally 1m. It is expected that this small baseline will introduce some decorrelation of the measurement biases which will no longer cancel completely in the double differencing process. The purpose of these tests is to quantify the effects this decorrelation has on both the quality of the solution and the ambiguity resolution processes.

4.4.1 Solution Accuracy and Precision

In Table 4.6 the accuracy and precision of the baseline estimates are given. They are first measured in terms of baseline component errors to allow comparison with the equivalent zero baseline test. They are then quantified in terms of the attitude solution which is of most interest to this work.

The best estimate of the baseline components and therefore attitude is the mean of the ambiguity fixed solutions. For this reason only the precision of the real world results is given.

Table 4.6: Static Short Baseline Accuracy and Precision

Solution Type	Real	Simulated	
	σ	Accuracy	σ
Float	0.68 m	0.01 m	0.58 m
Fixed	5.4 mm	7.9 μm	3.2 mm

Table 4.7: Static Short Baseline Attitude Accuracy and Precision

	Real	Simulated	
	σ ($^\circ$)	Accuracy ($^\circ$)	σ ($^\circ$)
Pitch	0.23	1.3×10^{-3}	0.16
Heading	0.11	0.3×10^{-3}	0.07

Discussion

The results in Table 4.6 show a small increase in noise between the ‘real world’ data and the simulated data. A similar increase in noise is observed between the short and zero baseline ‘real world’ data. This reflects the decorrelation of high rate multipath over this small distance.

The short baseline simulated results are very similar to those obtained over a zero baseline. As expected the atmospheric effects are removed in the double differencing process and therefore do not appear in the results. Since multipath is not simulated it does not appear in the noise levels.

The accuracy and precision of the attitude parameters (Table 4.7) justify the selection of GPS attitude determination for UAV georeferencing applications. For example a precision of 0.16° in pitch would result in a georeferencing error of around 30cm from a typical UAV flying height of 100 m. This is similar to the magnitude of the errors from other parts of the georeferencing process. If the baseline length were increased to 2m the results in Table 4.6 indicate that the ground error would approach 15cm given the same flying height. The relationship between attitude error and georeferencing error is discussed further in Appendix B.

4.4.2 Ambiguity Resolution

The effect of the decorrelated biases on the ambiguity resolution process is now examined. Tables 4.8 and 4.9 are intended for comparison with the zero baseline results in tables 4.3 and 4.4.

Table 4.8: Simulated Short Baseline Ambiguity Resolution Results

Ambiguity Fixing Method	Success %	χ^2	No. Candidates in search
Bootstrap	5.02	-	-
Bootstrap with Z transform	83.4	-	-
LAMBDA	88.4	0.12	3.12
Constrained LAMBDA	99.4	0.41	123
Constrained Float Input			
Bootstrap	18.2	-	-
Bootstrap with Z transform	93.4	-	-
LAMBDA	96.3	0.11	2.93
Constrained LAMBDA	99.7	0.40	105

Table 4.9: Short Baseline Ambiguity Resolution Results

Ambiguity Fixing Method	Success %	χ^2	No. Candidates in search
Bootstrap	0.32	-	-
Bootstrap with Z transform	30.4	-	-
LAMBDA	29.6	0.05	3.35
Constrained LAMBDA	86.7	0.24	224
Constrained Float Input			
Bootstrap	3.19	-	-
Bootstrap with Z transform	51.7	-	-
LAMBDA	55.1	0.04	3.02
Constrained LAMBDA	86.8	0.22	158

Discussion

Again the ‘real world’ short baseline results are worse than the zero baseline or simulated equivalent. Even in this case however the success rate of ambiguity resolution remains high, above 85% using the constrained LAMBDA method.

Other published work, (*Giorgi et al.*, 2008), tests the LAMBDA and constrained LAMBDA methods over a similar static short baseline (2.20m). In this work high quality, survey grade antennas are used with high quality receivers. This combination can be expected to mitigate ground reflected multipath much more effectively than the low cost equipment used in this thesis. Their results show ambiguity resolution success rates of 99.99% and 100.00% for the LAMBDA and constrained LAMBDA processes respectively. This agrees well with the multipath free simulated results in this work. This suggests that multipath is indeed to blame for the lower success rates in the real data when compared to the simulated data.

The best success rates of ambiguity resolution are achieved by the constrained LAMBDA process. Even in the ‘real world’ data the success rate remains above 85%. The use of a constrained float solution as the input does little to improve this success rate. However it does reduce the number of candidate ambiguity vectors which must be processed in the search step.

These results agree well with those published by the author in (*Pinchin*, 2008). They differ slightly due to different processing strategies and the use of a different type of receiver. In this 2008 paper it was argued that the standard LAMBDA or bootstrap with Z transform method gives acceptable results when used with the constrained float input. Using these techniques avoids the long search times associated with the constrained LAMBDA process. This approach is also justified by the present results which show success rates of around 95% in the simulated data and 55% in the ‘real world’ data.

4.4.3 Ambiguity Validation

In this section the effectiveness of the ambiguity validation techniques described in Section 2.9.4 and 3.8.3 are investigated.

First the use of the LAMBDA ratio test is examined. In Tables 4.10 and 4.11 the effect of the chosen threshold ratio on the quantity of false positives / negatives is given.

A false positive (candidate ambiguity vector passes the test but is in fact false) would be very detrimental in real world applications. It would allow an undetected error to affect the attitude results. The impact would be made worse if the wrong candidate vector is propagated forward to subsequent measurement epochs.

Conversely a false negative result (candidate ambiguity vector fails the test but is in fact correct) would pose no direct problem to the attitude results. It would however affect the efficiency of the ambiguity resolution process and so these errors should be minimised.

In testing the validation methods both the ‘real’ and simulated short baseline data is used. The input to the LAMBDA processes are the constrained float solutions.

Table 4.10: Use of the Ratio Test with the Standard LAMBDA Process

Threshold	Real		Simulated	
	False Pos. (%)	False Neg. (%)	False Pos. (%)	False Neg. (%)
1.5	33.6	27.6	76.7	14.3
3	20.5	27.0	50.7	37.9
5	12.4	33.7	31.2	57.3
8	7.6	38.4	18.8	69.6
10	5.5	40.5	14.7	73.7
20	2.0	44.0	6.3	82.0
30	1.4	44.7	3.4	85.0

Next the usefulness of the *a priori* baseline length for candidate validation is examined.

Table 4.11: *Use of the Ratio Test with the Constrained LAMBDA Process*

Threshold	Real		Simulated	
	False Pos. (%)	False Neg. (%)	False Pos. (%)	False Neg. (%)
1.5	77.5	11.4	97.4	2.1
3	55.6	30.8	81.4	18.0
10	24.2	62.2	28.3	71.1
30	7.2	79.2	6.8	92.6
70	1.7	84.7	1.8	97.6

In Table 4.12 the effect of the chosen threshold probability on the quantity of false positives / negatives is given. For clarity only the ‘real’ static zero baseline dataset is presented here.

Table 4.12: *The a priori baseline length as a validation tool*

Threshold	LAMBDA		Constrained LAMBDA	
	False Neg. (%)	False Pos. (%)	False. Neg. (%)	False Pos. (%)
50 %	0.00	20.1	0.00	13.7
90 %	0.00	1.10	0.00	12.2
95 %	0.07	0.93	0.00	9.60
98 %	16.8	0.50	16.8	5.97

Discussion

Tables 4.10 and 4.11 demonstrate the problems involved in using the ratio test. In order to minimise the number of false positives the threshold ratio must be increased. However this means a lot of false negative results especially for the constrained LAMBDA process which is effectively rendered useless by this test.

Table 4.12 shows that the baseline length makes a far more effective validation tool. False positives can be nearly eliminated by setting a confidence threshold of 98%. At this level the rate of false negatives is also low (16.8% for the LAMBDA process).

This validation method is less effective for the constrained LAMBDA method than the unconstrained version. This is because the constrained LAMBDA method always returns candidates which are close to the *a priori* baseline length. The high rate of false positive observed (5.97% compared to 0.50% from the standard LAMBDA method) means that the gains in success rate are offset by the reliability of the unconstrained methods with constrained float input. Taking validation into account the constrained LAMBDA method is a worse choice than the LAMBDA method in the absence of multipath.

4.5 UAV Flight Results

In this section GPS data from a low cost GPS receiver onboard a mini UAV is examined. The purpose is to analyse the quality of the carrier phase observables.

The flight profile consisted of six portions:

- Static Period.
- Acceleration and takeoff.
- Level off.

- Survey line & turn (repeated).
- Deceleration and Landing.
- Static Period.

The lines flown were necessarily short to keep the UAV within visual range of the pilot. The turns were performed at rates typical of survey UAV flight, no manoeuvres were performed with atypically high dynamics.

The ground track of the flight is shown in Figure 4.3.

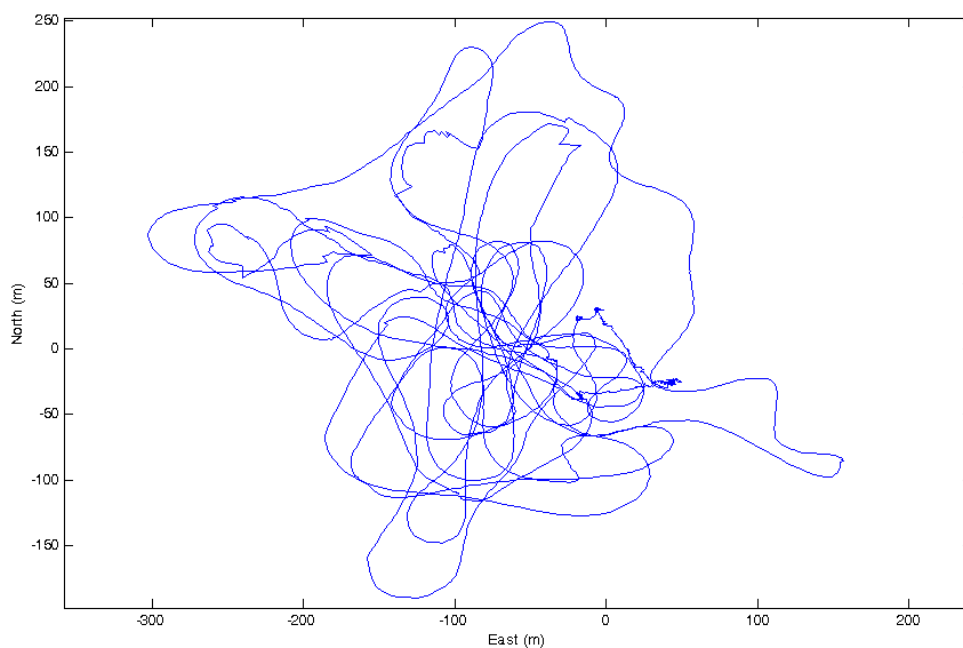


Figure 4.3: UAV Trial Flight Groundtrack

If carrier phase lock is completely lost in flight then no measurement will be output. By examining the number of phase measurements available over the course of the flight it was observed that 1% of epochs show a complete failure to track any satellites. Following a ‘failed’ epoch the receiver quickly regains the signal and epochs with no measurements occur individually or in very small clusters.

Another good measure of the receiver carrier phase tracking performance is its own reported Loss of Lock or LLI indicators. When the receiver detects a potential cycle slip an indicator is output with the data.

The RINEX (Receiver Independent Exchange Format) GNSS data format used in this work allows three types of LLI indicators, given in three data bits.

If the first bit is set to 1 the receiver has detected a loss of lock between measurement epochs and an integer wavelength cycle slip can be expected.

In Figure 4.4 the number of full cycle LLIs (type 1) at each measurement epoch is given. The UAV flying height profile derived from stand alone GPS positions is given to indicate when the UAV is in flight.

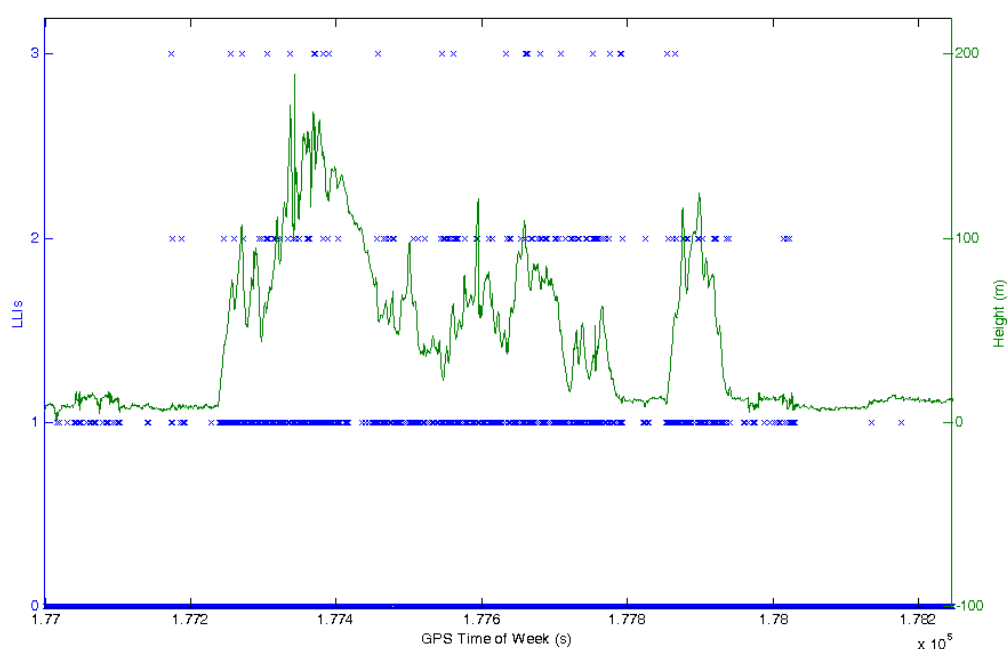


Figure 4.4: Full Cycle LLIs Observed During a UAV Flight

If the second bit is set the receiver has changed ‘wavelength factor’. The uBlox LEA-5T normally outputs data with half cycle ambiguities resolved (see Section 2.4.5). In the event of tracking difficulties the receiver is unable to do this and so changes the

wavelength factor from full cycle to half cycle. The measurement may therefore take three states, either correct or incorrect by plus or minus one half cycle.

In Figure 4.5 the number of half cycle LLIs at each measurement epoch is given.

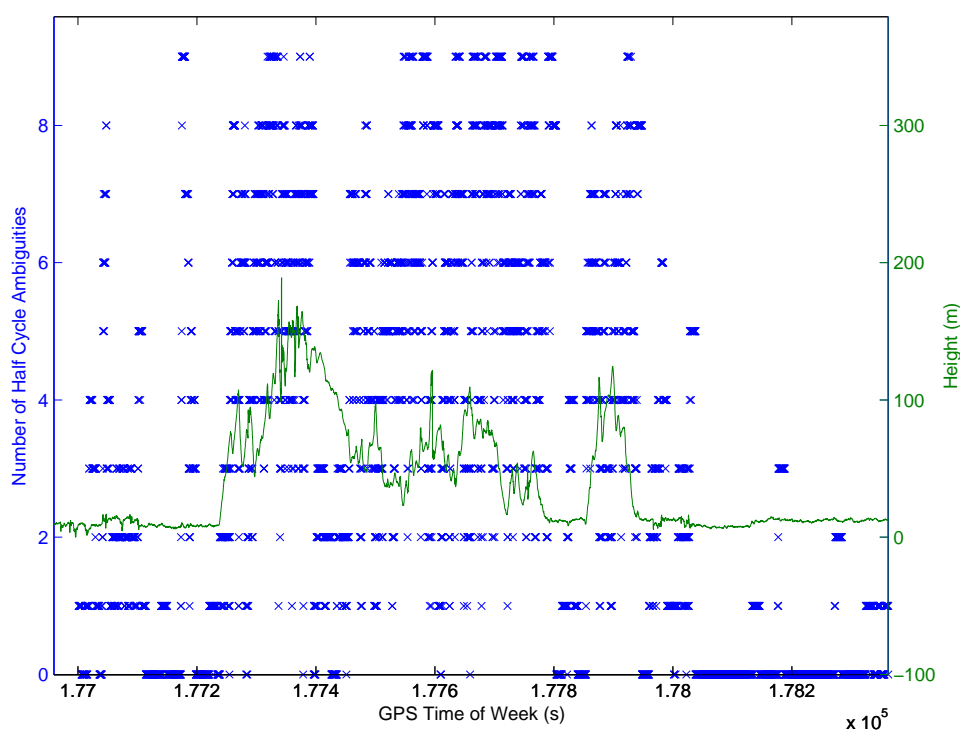


Figure 4.5: Half Cycle LLIs Observed During a UAV Flight

If the third LLI indicator bit is set then the measurement is contaminated by selective availability or anti-spoofing noise. This does not apply to L1 frequency measurements and so is not of concern to this work.

4.5.1 Discussion

The number of satellites tracked over a UAV flight remains high throughout most of the flight. When the receiver loses lock on a satellite it tend to lose lock on all the satellites in that epoch, suggesting that receiver motion is causing the incident rather than partial

signal blockage by the UAV airframe.

The number of full cycle slips remains low throughout the flight. When a full cycle slip does occur one of three approaches may be taken - remove the measurement, estimate the cycle slip or estimate the integer ambiguities without reference to the previous epoch.

If the success rate of ambiguity resolution is high enough (see 4.4.2), ambiguities can be resolved independently at each epoch and integer cycle slips between epochs will not affect the solution.

If the success rate of ambiguity resolution is low, validated ambiguity vectors need to be propagated between epochs to maximise the availability of an attitude solution. In this case the integer cycle slips will affect the solution since the validated ambiguity vector will no longer be valid. We can choose to estimate the integer cycle slip and correct the validated ambiguity vector. Or the measurement and integer ambiguity affected by the full cycle slip can be removed.

This data indicates that the measurement can often be safely removed while leaving enough observations to produce a solution. Therefore no full cycle slip resolution process is necessary to produce valid attitude results.

However in around 1% of the measurement epochs in this dataset insufficient observations remain without integer cycle slips. For these epochs a valid attitude solution will not be available if the integer ambiguities are not resolved or the cycle slip quantified.

The number of half cycle ambiguities remains high throughout the kinematic portion of this data. In many measurement epochs all of the observations are half cycle ambiguous. Removing these observations is therefore not an option if an attitude solution is to be estimated. The half cycle slips must be quantified or the half cycle ambiguities resolved to maximise the number of epochs with a valid attitude solution.

4.6 Simulated UAV Flight

To reproduce the full and half cycle slip problem under predictable conditions a simulated flight profile was generated using the hardware simulator. A zero baseline test was performed to allow simple recovery of the correct integer ambiguities.

Again this flight profile consisted of six sections;

- Static Period.
- Acceleration and takeoff.
- Level off and maintain constant speed.
- Survey line & 90 degree turn (repeated).
- Deceleration and Landing.
- Static Period

In this data the 90 degree turns result in short bursts of acceleration and bank angle. It is expected that these will result in cycle slips. The turns are followed by 30 seconds of straight and level flying to allow the receiver to recover the half cycle ambiguities and resume good carrier phase tracking.

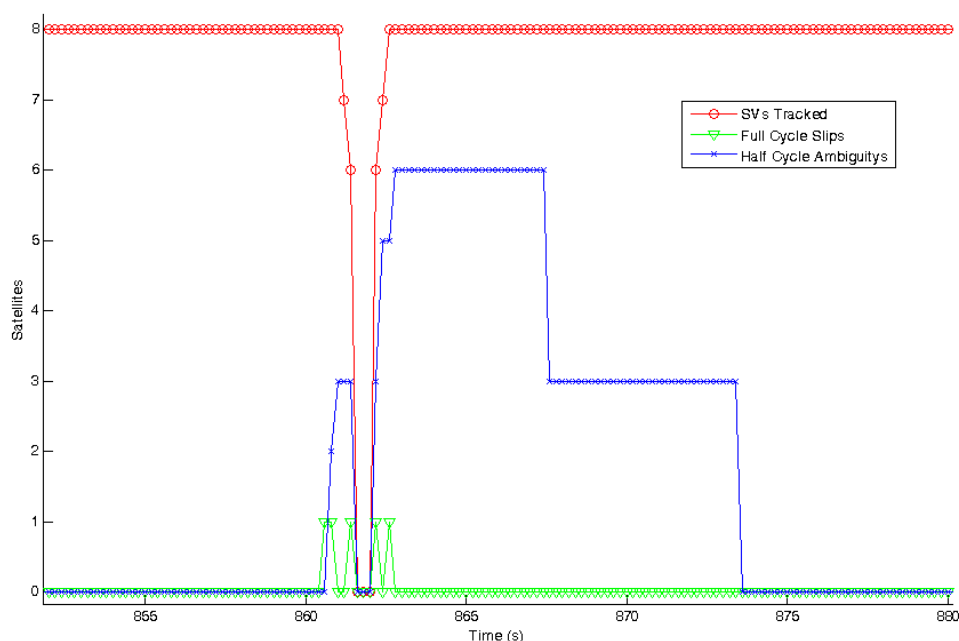


Figure 4.6: The Effects of UAV Acceleration in a Turn on Phase Tracking

In Figure 4.6 the effects of one turn on carrier phase tracking are depicted. At the start of the example the receiver is tracking all eight GPS satellites in view. At 861 seconds the turn begins. Soon the half and full cycle slips occur. In the turn the receiver loses lock on all satellites. At the end of the turn at around 864 seconds the receiver quickly regains all satellites. Half cycle ambiguities remain however until around 9 seconds after the turn.

Artifacts in the double difference code observations can also be observed after a turn. Figure 4.7 shows the code residuals during three turns. On the second axis acceleration is plotted to indicate when the turns occur.

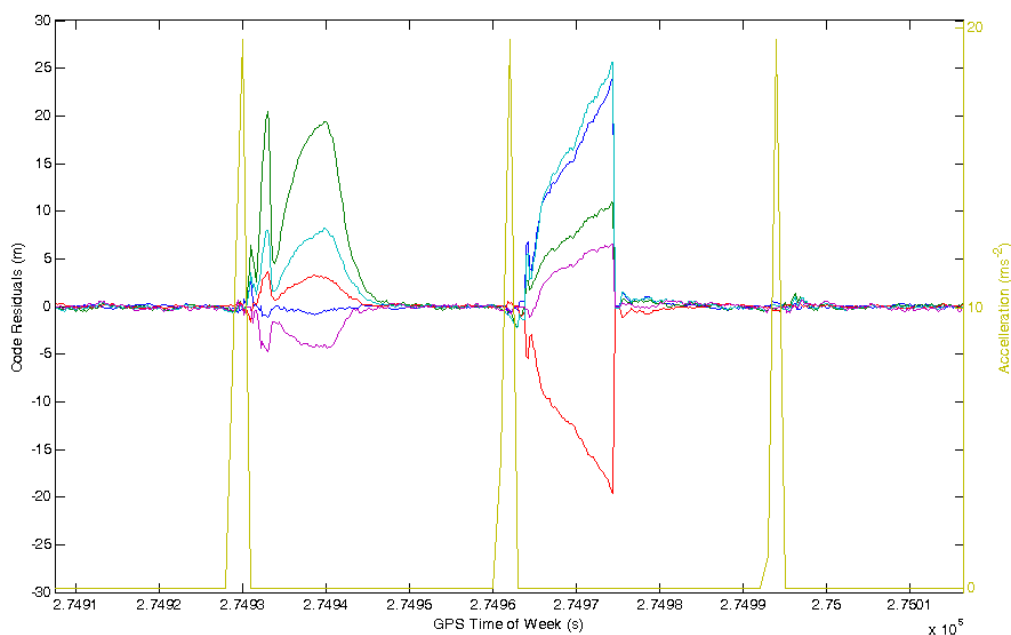


Figure 4.7: The Effects of UAV Acceleration in a turn on Code Tracking

4.6.1 Discussion

The simulation results show that the acceleration of a turn can cause loss of phase lock and cycle slips. Large biases are also observed in the double difference code observations.

In Figure 4.7 it can be seen that the code measurements show large biases after a turn. This is likely to be due to the operation of the tracking loops within the receiver. Since the methods used within the receiver are proprietary it is not possible to say exactly what the cause is.

The consequence for this work is that the float solution, dominated by code measurements, is likely to be un-useable for some time after an turn.

Figure 4.6 shows that during a turn no GPS attitude estimates can be expected since no satellites are tracked. The GPS attitude solution must restart after the turn using the float solution to estimate ambiguities.

After the acceleration ceases the receiver takes around 9 seconds of steady flight to regain the half cycle ambiguities and output full cycle carrier phase for all satellites in view. In a real UAV flight 9 seconds of flight will cover a long distance. If data georeferencing is not possible for this period the flight will be very inefficient. It is imperative that a method for making use of half cycle ambiguous carrier phase data is developed.

4.7 Conclusion

In this chapter it has been established that the accuracy and precision of the GNSS attitude estimates are sufficient for the mini-UAV georeferencing application. Accuracies of 1.3 thousandths of a degree in pitch and 0.3 thousandths of a degree in heading were achieved. The precision of heading and pitch/roll estimates obtained using low cost equipment and a 1m baseline was 0.07 and 0.16 degrees respectively. This was reduced to 0.11 and 0.23 degrees in the presence of ground reflection multipath.

This precision, while already adequate for many georeferencing applications, could be further improved by increasing the baseline length where the size of the UAV allows.

Zero baseline tests using real and simulated radio frequency inputs show good agreement both in terms of the accuracy and precision of the attitude estimates and in terms of the ambiguity resolution success rates.

The quality of the attitude estimates and the success rate of ambiguity resolution dropped when data was collected over a short baseline in real world tests. Data collected over a simulated short baseline agrees closely with the zero baseline equivalent. Since multipath is the only bias not simulated this suggests that multipath decorrelates even over a sort baseline of 1m.

Over a short real world baseline ambiguity resolution success rates reached up to 86%. In simulated trials without multipath the success rate reached 100% suggesting that if

multipath could be fully mitigated the real world success rates would improve.

The benefits of using a constrained float input have been demonstrated. Significant improvements have been seen in both the bootstrap and LAMBDA success rates. The Quadratic Eigenvalue approach to constraining the float solution has been stable throughout the data sets used in the present research.

When using the constrained float solution the success rate of unconstrained LAMBDA and the bootstrap with Z transform techniques reached 96% and 93% respectively. They therefore may be more relevant to real time applications since they avoid the heavy processing overhead involved in the constrained LAMBDA process.

Use of the *a priori* baseline length knowledge to validate integer ambiguity candidates, as contributed by the author, has been seen to give significantly better results than use of the traditional LAMBDA ratio tests. The ratio tests give higher rates of both false positive and negative errors when compared to the baseline length techniques. Efficient validated ambiguity resolution and a robust GNSS attitude solution is dependent on the use of the developed baseline validation method.

When validation is taken into account and using the constrained float solution, the bootstrap with Z-transform and LAMBDA processes show better success rates than the constrained LAMBDA method.

Finally real GPS data from a mini-UAV was found to contain many loss of tracking incidents as well as full and half cycle slips. Using the hardware simulator it was found that these may be caused by the accelerations involved in a turn which also cause biases in the double difference code measurements.

Since the details of the operation of the tracking loops is proprietary information the exact cause of the loss of phase tracking and introduction of code biases cannot be established. However the consequences for this work are;

- Sufficient phase measurements are not available throughout the flight, at times no measurements are available. This causes gaps in the availability of the GPS attitude solution which must be bridged.
- Since the code measurements are often biased by acceleration it cannot be assumed that an effective float solution can be obtained after a gap in phase measurements. An estimate of the float ambiguities must then come from another source.
- For large portions of the flight carrier phase data is output by the receiver which is not resolved to full carrier phase cycles. Until full cycle measurements are output the half cycle ambiguities must be resolved in order to use the measurement.

These are the problems addressed by the following chapters.

Chapter 5

Attitude Rate Modelling and Estimation

5.1 Introduction

In Chapter 4 problems with using GNSS attitude determination on a mini-UAV were identified. Rapid rotational acceleration causes loss of carrier phase tracking, half cycle ambiguous carrier phase data and unusable code pseudorange measurements. In this chapter strategies for dealing with these problems will be introduced.

First the problem of using the half cycle ambiguous carrier phase data is dealt with. The option of solving for half cycle ambiguities using the previously introduced integer ambiguity estimators is discussed.

The triple difference carrier phase observable is then examined in more detail. It is usable even with half cycle ambiguous carrier phase observations if no cycle slips occur. It can also be used to correct for cycle slips if the change in attitude between epochs can be predicted or obtained from another source.

To predict the change in attitude between epochs, kinematic and dynamic models are developed. The inputs to these models are discussed in detail and their integration with the triple difference observable examined.

The integration of GPS based velocity measurements with a dynamic model has been

suggested in previous work, for example (*Lievens et al.*, 2005) or (*Park and Kee*, 2006). In that research the velocity derived from a single GPS receiver and simple stand alone positioning was integrated with a dynamic model to predict the platform attitude to within a few degrees. The results of this method were of insufficient accuracy for georeferencing applications. The techniques proposed also require good code signal tracking throughout a manoeuvre and the attitude estimates were aided by airspeed measurements which added cost and weight to the system. For those reasons they are not suited to the present application.

Other work, for example (*Lightsey and Madsen*, 2003) has suggested the use of a dynamic model augmented by signal to noise measurements to estimate attitude. This technique requires an expensive calibrated antenna and relies on the use of a receiver with high resolution signal to noise reporting. The results of that work were also of insufficient accuracy for georeferencing applications.

The use of platform attitude models with the triple difference observable is a key innovation in this thesis. It allows data gaps to be bridged and sub-optimal quality GPS measurements to be used. This in turn increases the availability of an altitude solution throughout the UAV flight and high accuracy attitude estimates during steady flight. Previously no attitude solution would be available during and after a moderate turn in the flight path.

5.2 Ambiguity Resolution

The ambiguity resolution methods introduced in Section 3.8 can be adapted to resolve the ambiguities to half integers. Using this approach the half cycle ambiguous carrier phase data can be treated in exactly the same way the the normal full cycle ambiguous data.

If the quality of the code observations remained constant throughout the flight the variance of the float ambiguities would remain similar. Even in this case the success rate

of half cycle ambiguity resolution could be expected to be considerably lower than that of full cycle ambiguity resolution. We would therefore need to use the best estimator available, the constrained LAMBDA method.

Double difference carrier phase measurements are normally ambiguous to one full cycle. A half cycle on one carrier phase observation before differencing introduces three further possible states - integer, minus one half cycle of plus one half cycle. In the worst case all of the undifferenced observations are half cycle ambiguous and the double difference observation can take nine states for each integer candidate. This extra number of candidates alone will make constrained LAMBDA method impractical.

In Chapter 4 it was observed that the quality of the code data does in fact not remain constant throughout the flight and can degrade considerably until full phase tracking is regained. Even with the optimal ambiguity estimator and allowing a large number of search candidates the success rate of half cycle ambiguity resolution can therefore be expected to be negligibly low.

An estimate of the platform attitude from another source, independent of the code observables, can be used to compute a float ambiguity solution. If it is of sufficient precision and accuracy this float solution will lead to a high ambiguity resolution success rate. For a new estimate of the platform attitude this work now turns to the carrier phase triple difference observable, and modelling techniques. Both give an estimate of the platforms rotation rate which may be integrated over time to give the change in platform attitude.

5.3 The Triple Difference Observable

In Section 2.6 the triple difference observable was introduced.

Its observation equation is reproduced here;

$$\lambda \delta \nabla \Delta \phi_{ab}^{ij} = \delta \nabla \Delta \rho_{ab}^{ij} + \varepsilon(\delta \nabla \Delta \phi) \quad (2.14)$$

In the triple difference observable the integer ambiguity has been removed if it has not changed between epochs (a cycle slip). This will also be true of the half integer ambiguities.

5.3.1 Relative Attitude Estimation

The triple difference geometric range $\delta \nabla \Delta \rho_{ab}^{ij}$ can be used to obtain the change in baseline between epochs. This is related to the relative velocity of the antennas, or angular velocity of the GNSS attitude system. The triple difference observable can therefore be used to estimate the change in attitude over time.

Assuming no cycle slips, the total error in the attitude obtained using the triple difference is composed of two parts. The error in the start attitude and the sum of the errors in the angular velocity estimates.

If the sum of the errors in the angular velocity estimates are sufficiently low and the starting attitude is of high quality, the triple difference observable may be used to give a float estimate of the attitude and ambiguities. The initial attitude estimate will be high quality from a fixed ambiguity estimate while signal tracking is good and the triple differenced observable can then be used to give a float estimate in subsequent epochs.

While the error in the attitude obtained using the triple difference observable remains lower than the error in a code based float solution, it is a better option to use as the float solution.

The same is true when processing data in reverse. In post-processing or even small latency applications the triple difference may be used to provide float estimates backwards in time from a fixed ambiguity attitude estimate. If the sum of the errors in the angular

velocity estimates are low the triple difference observable may even provide an attitude estimate which is of high enough quality to negate the need to fix ambiguities during half cycle carrier phase tracking.

5.3.2 Cycle Slip Correction Using the Triple Difference

If the triple difference geometric range $\delta\nabla\Delta\rho_{ab}^{ij}$ can be estimated from another source it can be removed from the triple difference observations leaving only cycle slips and noise. In the current application this requires an estimate of the platform angular velocity to obtain $\delta\nabla\Delta\rho_{ab}^{ij}$.

$$\delta\nabla\Delta\phi_{ab}^{ij} = \frac{\Delta(\delta\nabla\Delta\rho_{ab}^{ij})}{\lambda} + \delta\nabla\Delta N_{ab}^{ij} + \varepsilon(\delta\nabla\Delta\phi) \quad (5.1)$$

Where $\Delta(\delta\nabla\Delta\rho_{ab}^{ij})$ is the error in the triple difference geometric range prediction and $\delta\nabla\Delta N_{ab}^{ij}$ is a cycle slip.

If the sum of the error in the triple difference geometric range estimate and the noise $\varepsilon(\delta\nabla\Delta\phi)$ is less than the magnitude of a cycle slip, the slip can be detected. In the current application we need to detect half cycle changes.

The problem of obtaining an estimate of the platform angular velocity remains. In previous work it has been obtained from code and doppler GNSS observation (*Kim and Langley, 2003*). In the current application these prove to be too noisy and unreliable for half cycle slip resolution. As seen in Chapter 4, code measurements in particular are unreliable after signal tracking disturbances.

Another option is to use a second navigation sensor, such as an inertial measurement unit. The cost and weight penalties of this approach negate the benefits of using GNSS attitude determination.

In this work a method which uses mathematical models to predict the platform motion is developed.

5.3.3 Triple Difference Summary

- The triple difference observation can provide precise angular velocity estimates without needing to resolve ambiguities. It is usable with full and half cycle ambiguous carrier phase measurements.
- The angular velocity measurements can be integrated with respect to time in order to obtain an estimate of the change in attitude.
- The estimate of the change in attitude can be used to produce a double difference float solution from a fixed solution at another epoch.
- The triple difference observation is corrupted by cycle slips.
- To estimate and correct for cycle slips an estimate of the angular velocity is required to remove its effect on the triple difference observation.
- In this work this estimate will be derived from a model of the platforms motion.

5.4 Attitude Modelling

In this section three models of the platform attitude will be derived. The purpose of these models is to bridge the gaps in GNSS carrier phase availability and allow cycle slip detection using the triple difference observable.

Many such models have been proposed for aircraft dynamics and this is an evolving field of research. In recent years mini-UAVs have provided a challenge to those trying to model the torques and moments acting on aircraft. The high range of flight modes exhibited by

the UAV mean that ‘traditional’ methods involving linearisation of the dynamic model around one stable flight condition are not optimal.

First the simpler kinematic models are introduced for later comparison with the dynamic model. Then the equations of motion and an aerodynamic model are developed and combined to form a state space dynamic model of the UAV. The problem of identification of this model is treated and the instrumentation used is described.

5.4.1 Kinematic Models

Kinematics is the “branch of mechanics concerned with the motions of objects without being concerned with the forces that cause the motion” (*Isaacs, 2000*). The most basic form of kinematic model is the constant attitude model. While suitable for static applications this model is unlikely to give useful predictions for the length of GNSS outages on a dynamic UAV platform. To improve the model the variation of attitude with time must be modelled. Increasing orders of time differentiation will allow the interval between GNSS measurements to be extended while maintaining the quality of estimate from the model.

In this section the constant angular rate and angular acceleration models are introduced.

Constant Angular Rate

The constant angular rate model describes the attitude of the platform at epochs k and $k + 1$ via a first order differential equation.

The quaternion attitude formulation is used in this model to allow small errors which will accumulate over time to be managed via normalisation of the quaternion vector. Where \mathbf{q} , $\dot{\mathbf{q}}$ and $\ddot{\mathbf{q}}$ are the attitude, total angular rate and total angular acceleration parameterised in terms of the quaternions;

$$\mathbf{q}_{k+1} = \mathbf{q}_k + \dot{\mathbf{q}}\Delta t \quad (5.2)$$

Where;

$$\dot{\mathbf{q}} = \frac{d\mathbf{q}}{dt} = constant \quad (5.3)$$

The nature of the dynamics of the small UAV makes this model suitable for use where the time interval Δt is kept small. It will work well for constant attitude flight modes and constant rate turns. For other flight modes the second order differential, or constant angular acceleration model may be used.

Constant Angular Acceleration

By assuming that the rotation rate of the platform will continue to change in a constant way after a GNSS solution outage, the constant acceleration model is obtained.

The validity of this model over time will depend on the flight mode when the GNSS solution is lost. This model will work well for constant attitude, constant turn rate and constant acceleration into and out of a turn. If the flight mode changes during the outage this model will fail.

$$\mathbf{q}_{k+1} = \mathbf{q}_k + \dot{\mathbf{q}}_0\Delta t + \frac{1}{2}\ddot{\mathbf{q}}\Delta t^2 \quad (5.4)$$

Where;

$$\ddot{\mathbf{q}} = \frac{d\dot{\mathbf{q}}}{dt} = constant \quad (5.5)$$

5.4.2 The Attitude Dynamics Model

Dynamics is “the branch of mechanics concerned with the motion of bodies under the action of forces” (*Isaacs*, 2000). It is the study of the forces acting to rotate the UAV

which will allow us to predict its change in attitude over time. This section will develop a model of these forces and the motion that results through the application of Newton's second law.

5.4.3 Fundamentals and Assumptions

Reference Frames

The equations of motion derived below will assume that the reference frame is inertial, ie one in which a bodies motion remains unchanged unless a force is applied. In an inertial reference frame Newton's laws of motion are valid. An inertial frame is non-rotating and fixed relative to the stars.

For the purposes of this work the local level frame described in Chapter 3 is considered an inertial frame. While this is not strictly true due to the earths rotation relative to the stars, it is a fair assumption given that the earths rotation is negligible in the timescales concerned and the forces due to this rotation are negligible.

A further reference frame known as the wind frame must also be considered. The x axis of the wind frame points from the UAV centre of gravity along the velocity vector. When the UAV velocity points along the body frame x axis then the wind and body frames are collinear. This is known as 'trimmed flight'. The rotation of the wind x axis about the body y axis is known as the 'angle of attack' α . The rotation of the wind x axis about the body z axis is known as the 'angle of sideslip' or β . This relationship is depicted in Figure 5.1.

The origin of the wind axis is called the 'aerodynamic centre' of the UAV. If it collocated with the centre of gravity (the origin of the body frame) then no rotation will result from the linear movement of the UAV.

As described in Chapter 3, the platform attitude is defined as the rotation between the

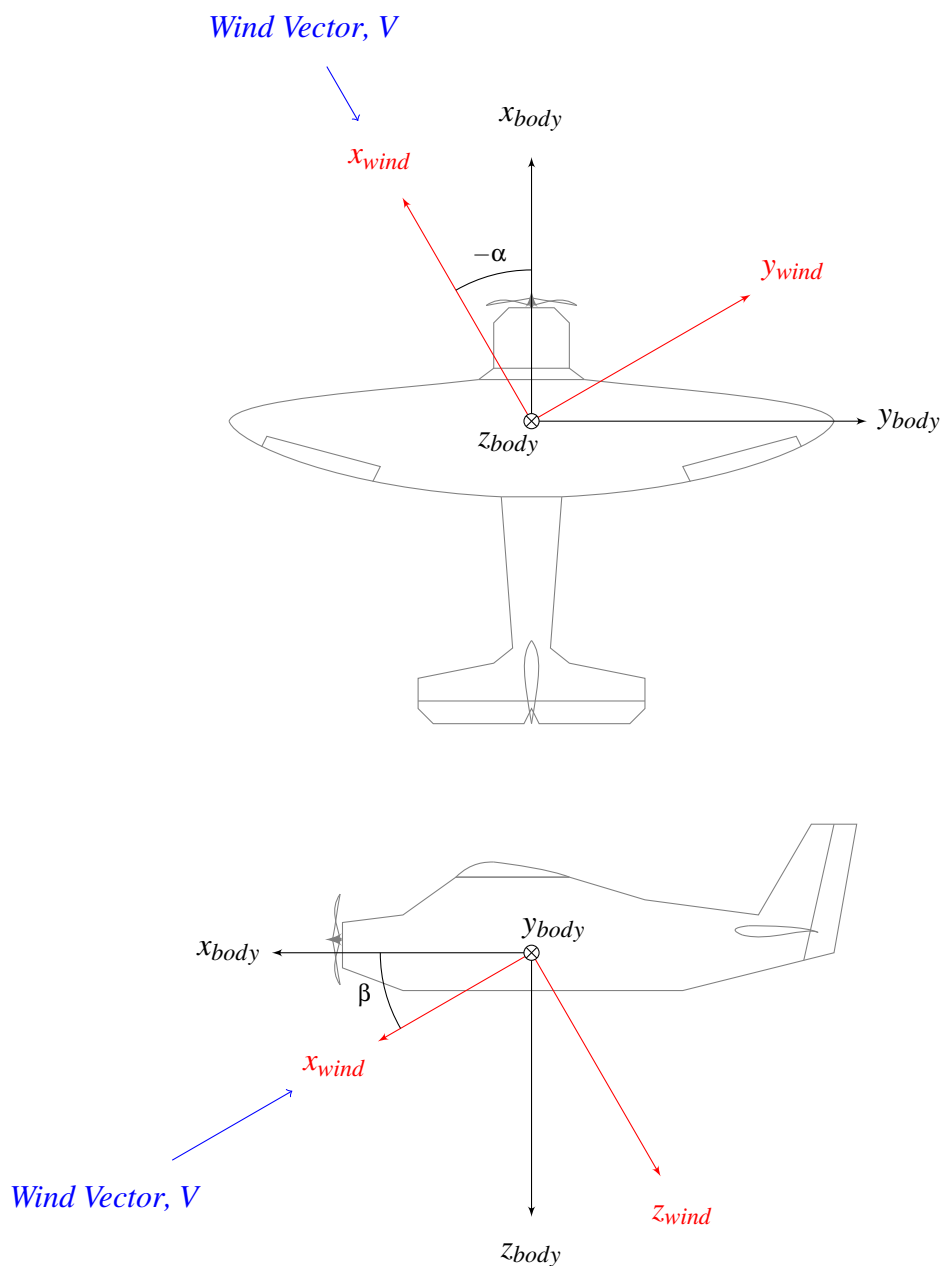


Figure 5.1: The relationship between the wind frame and the body frame.

local level and body frames through the euler angles ϕ , θ and Ψ . Since the dynamic model is developed in the body frame the rotation rates in the body frame p , q and r will not be identical to the roll, pitch and yaw rates $\dot{\phi}$, $\dot{\theta}$ and $\dot{\Psi}$ unless the local level and body

frames are parallel.

In all other cases the relationship is ((Duke *et al.*, 1988));

$$\begin{aligned}
 \dot{\Phi} &= p + q \sin \Phi \tan \theta + r \cos \Phi \tan \theta \\
 \dot{\theta} &= q \cos \Phi - r \sin \Phi \\
 \dot{\Psi} &= q + q \sin \Phi \sec \theta + r \cos \Phi \sec \theta
 \end{aligned}
 \tag{5.6}$$

Assumptions

The aircrafts moment of inertia is constant. This assumption is only truly valid for short time spans since, in most UAVs, fuel will be used over the course of the flight. If payload is moved or dropped during flight this assumption will be violated. This is not the case for the survey UAVs of interest to this work.

The mass of the UAV is symmetric in the plane defined by the x_b and z_b axes. Any motion in the x_b - z_b plane will now be termed ‘symmetric’, for example wings level climbs, descents or loops. Any motion out of this plane, for example banked turns or yaw, will be called an ‘asymmetric’ motion. This assumption allows simplification of the inertia matrix as will be seen below.

The UAV is a rigid body. Since the UAV platform will flex due to aerodynamic forces this assumption will be invalidated when the platform dynamics increase. For the purposes of this work it is assumed that the small UAV is sufficiently rigid to withstand these forces without significant flex. If this assumption is violated the effect will be a change in the moment of inertia and a small change in the aerodynamic properties.

Rotational Dynamics

When considering rotational dynamics it is common to consider the Torque (\mathbf{T}) acting to rotate the body. Torque is the analogue of the concept of force used in linear dynamics. It is defined as the “product of a force and its perpendicular distance from a point about which it causes a rotation or torsion” (*Isaacs, 2000*).

If torque is the analogue of force then the moment of inertia (\mathbf{I}) is the analogue of mass. It is the sum of all elements of mass multiplied by the square of their distance from the axis of rotation.

The analogue of Newton’s second law is therefore:

$$\mathbf{T}_b = \mathbf{I}\dot{\omega}_b \quad (5.7)$$

Where $\dot{\omega}_b$ is the rotational acceleration. The subscript b denotes a quantity in the body frame.

Angular momentum (\mathbf{H}) is the analogue of linear momentum. It is the product of the angular velocity of the body (ω) and its moment of inertia (\mathbf{I}) or (in the body frame):

$$\mathbf{H}_b = \mathbf{I}\omega_b \quad (5.8)$$

Expanding Equation 5.8 as in (*Calhoun, 2006*) we can derive:

$$\mathbf{H}_b = \begin{bmatrix} I_{xx} & -I_{xy} & -I_{xz} \\ -I_{yx} & I_{yy} & -I_{yz} \\ -I_{zx} & -I_{zy} & I_{zz} \end{bmatrix} \begin{bmatrix} p \\ q \\ r \end{bmatrix} \equiv \mathbf{I}\omega_b \quad (5.9)$$

Where p, q and r are the rotation rates about the body x, y and z axis. These are otherwise

known as the roll rate, pitch rate and yaw rate respectively. \mathbf{I} is hereafter known as the inertia matrix. Its elements describe the body mass distribution around the origin.

The assumptions made above mean that the inertia matrix, \mathbf{I} , can be reduced to:

$$\mathbf{I} = \begin{bmatrix} I_{xx} & 0 & -I_{xz} \\ 0 & I_{yy} & 0 \\ -I_{zx} & 0 & I_{zz} \end{bmatrix} \quad (5.10)$$

5.4.4 Equations of Motion

The derivation of the rotational equations of motion in this work will follow (*Stevens and Lewis, 1992*). We begin by modelling the motion caused by torques acting on the UAV. We then go on to approximate the torques in terms of their causes.

The torque \mathbf{T} , acting on the UAV can be expressed in the body frame using Newton's second law as:

$$\mathbf{T}_e = \frac{d}{dt} \mathbf{H}_b \quad (5.11)$$

The torque in Equation 5.11 is expressed in the inertial frame (the ECEF frame, denoted by the subscript e). For simplicity we will estimate the torques in the body frame since the causes of those torques act in the body frame. Therefore the Coriolis law (or 'transport theorem') is used to transform Equation 5.11 from the inertial frame to the rotating body frame;

$$\mathbf{T}_b = \dot{\mathbf{H}}_b + \boldsymbol{\omega}_b \times \mathbf{H}_b \quad (5.12)$$

Where $\dot{\mathbf{H}}_b$ is the derivative of the angular momentum with respect to time. We can now

expand Equation 5.12 to give the torques in terms of the angular rates and accelerations;

$$\mathbf{T}_b = \mathbf{I}\dot{\boldsymbol{\omega}}_b + \boldsymbol{\omega}_b \times (\mathbf{I}\boldsymbol{\omega}_b) \quad (5.13)$$

Expanding again;

$$\mathbf{T}_b = \begin{bmatrix} I_x & 0 & -I_{xz} \\ 0 & I_y & 0 \\ -I_{zx} & 0 & I_z \end{bmatrix} \begin{bmatrix} \dot{p} \\ \dot{q} \\ \dot{r} \end{bmatrix} + \left(\begin{bmatrix} p \\ q \\ r \end{bmatrix} \times \begin{bmatrix} I_x & 0 & -I_{xz} \\ 0 & I_y & 0 \\ -I_{zx} & 0 & I_z \end{bmatrix} \begin{bmatrix} p \\ q \\ r \end{bmatrix} \right) \quad (5.14)$$

Finally;

$$\mathbf{T}_b = \begin{bmatrix} L \\ M \\ N \end{bmatrix} = \begin{bmatrix} \dot{p}I_{xx} + qr(I_{zz} - I_{yy}) + (pq + \dot{r})I_{xz} \\ \dot{q}I_{yy} + rp(I_{xx} - I_{zz}) + (p^2 - r^2)I_{xz} \\ \dot{r}I_{zz} + pq(I_{yy} - I_{xx}) + (qr - \dot{p})I_{xz} \end{bmatrix} \quad (5.15)$$

Where L, M and N are known as the roll moment, pitch moment and yaw moment. Equation 5.15 allows us to relate the components of the rotation rate to the components of the torque applied to the airframe. Rearranging Equation 5.15 for the rotational accelerations;

$$\begin{bmatrix} \dot{p} \\ \dot{q} \\ \dot{r} \end{bmatrix} = \begin{bmatrix} \frac{1}{I_x I_z - I_{xz}^2} \{I_z [L + (I_y - I_z)qr] + I_{xz} [N + (I_x - I_y + I_z)pq - I_{xz}qr]\} \\ \frac{1}{I_y} [M + pr(I_z - I_x) + (r^2 - p^2)I_{xz}] \\ \frac{1}{I_x I_z - I_{xz}^2} \{I_x [N + (I_x - I_y)pq] + I_{xz} [L + (I_y - I_x - I_z)qr + I_{xz}pq]\} \end{bmatrix} \quad (5.16)$$

It can be seen that these equations are coupled and non-linear functions of the rotation rates p, q and r .

Given an estimate of the torques causing rotation we are now in a position to predict the rotational accelerations. Integration of these accelerations over time will give an estimate of angular velocity and from there, angular displacement.

The equations of motion derived so far do not account for the causes of the torques. In order to accurately predict the motion of the UAV we need to develop a model to approximate the torques in terms of the control inputs and characteristics of the airframe. This is done using the aerodynamic model.

5.4.5 The Aerodynamic Model

In the aerodynamic model the torque is described in terms of the ‘dynamic pressure’, the torque on the UAV due to the movement of the UAV surface through the air. This dynamic pressure is a result of a number of factors including;

- Control Inputs, δ_{ail} (aileron), δ_{rud} (rudder), δ_{elv} (elevator) and δ_{th} (throttle).
- Air-relative velocity, through the angle of attack and sideslip α and β .

- The rotation rates p , q and r .
- The body geometry.
- The local density of the air.

We can say that;

$$\begin{aligned}
 L &= C_l \bar{q} S b = C_l \left(\frac{1}{2} \rho V^2 \right) S b \\
 M &= C_m \bar{q} S \bar{c} = C_m \left(\frac{1}{2} \rho V^2 \right) S \bar{c} \\
 N &= C_n \bar{q} S b = C_n \left(\frac{1}{2} \rho V^2 \right) S b
 \end{aligned} \tag{5.17}$$

Where;

C_l , C_m and C_n are dimensionless coefficients which will vary with control input and rotation rate,

\bar{q} is the free stream dynamic pressure,

ρ is the air density,

V is the airspeed,

S is a reference area (in this case the wing planform area),

b is the wingspan,

and \bar{c} is the mean aerodynamic chord of the wing.

Recall the assumption made in Section 5.4.3 that the airframe is symmetrical in the x_b - z_b plane. Motions in this plane are called symmetric motions and those out of this plane asymmetric. We now further assume that state and control variables relating to symmetric parameters (e.g. θ , q and δ_{elv}) have no influence on the asymmetric coefficients C_l and C_n and *vice versa*.

Control Inputs

As throughout this work the mini-UAV in question is assumed to be a propeller driven fixed wing aircraft suitable for survey work. Control inputs are made to the aircraft to control pitch, roll, yaw and thrust. In the derived model we take a typical fixed wing aircraft layout with independent aileron, rudder and elevator inputs. The model will need to be adapted for UAVs with other control layouts.

In this work we take the aileron control to produce a pure rolling motion, the rudder to produce a combined roll and yaw motion and the elevator to produce a pure pitch motion.

The throttle input controls the rotation speed of the propeller and therefore the thrust. The throttle input needs to be considered in this work since it will affect not only the thrust force but also all of the torques.

If the motor, and thrust vector, is collinear with the body x axis then no rotation will be caused regardless of the magnitude of the thrust. Any misalignment of the motor will cause the thrust rotate the UAV at a rate determined by the magnitude of the misalignment and the thrust.

A change in the throttle setting will result in a rotational acceleration of the propeller. This in turn will produce a reaction which will rotate the UAV. This is depicted in Figure 5.2.

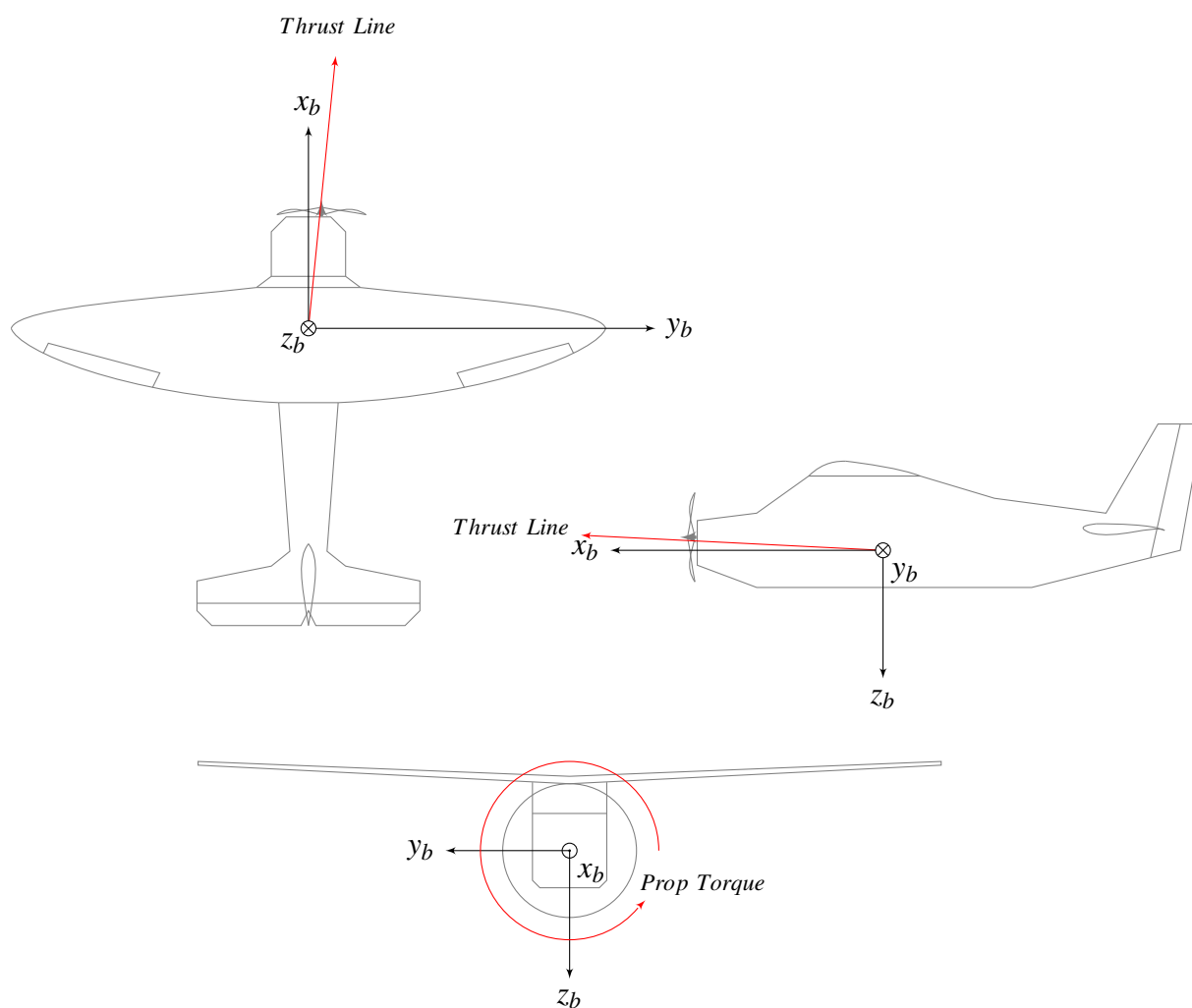


Figure 5.2: Engine Torques

The Aerodynamic Coefficients

In Equation 5.17 the aerodynamic coefficients C_l , C_m and C_n were introduced. The magnitude of these coefficients will vary with control input and aerodynamic restoring forces.

The partial derivatives of the aerodynamic coefficients with respect to the control inputs and aerodynamic restoring forces are known as the control and stability derivatives. For example $C_{L\Omega}$ is the partial derivative of C_L with respect to parameter Ω ;

$$\frac{\delta C_L}{\delta \Omega} = C_{L\Omega} \quad (5.18)$$

The full expression for the torques L, M and N now becomes;

$$\begin{bmatrix} L \\ M \\ N \end{bmatrix} = \begin{bmatrix} (C_{L\beta}\beta + C_{Lp}p + C_{Lr}r + C_{L\delta_{ail}}\delta_{ail} + C_{L\delta_{rud}}\delta_{rud} + C_{L\delta_{th}}\delta_{th}) b \\ (C_{M0} + C_{M\alpha}\alpha + C_{Mq}q + C_{M\delta_{elv}}\delta_{elv} + C_{M\delta_{th}}\delta_{th}) \bar{c} \\ (C_{N\beta}\beta + C_{N\beta}\beta^2 + C_{Np}p + C_{Nr}r + C_{N\delta_{rud}}\delta_{rud} + C_{N\delta_{th}}\delta_{th}) b \end{bmatrix} \frac{\rho V^2 S}{2} \quad (5.19)$$

The control and stability derivatives are dimensionless and non-linear. Traditionally the model 5.19 is now linearised around a ‘trimmed flight’ condition and values for the derivatives identified.

The values may be experimentally determined using wind tunnels and / or flight data or modelled using software such as the United States Air Force Stability and Control Digital DATCOM. Such software takes the geometry of the aircraft as an input and returns values of for the derivatives at a set of flight conditions. These values can then be used in a ‘lookup table’ when modelling the flight dynamics.

In flight the mini-UAV has a low Reynolds number, the ratio of the inertial forces to the aerodynamic forces is very low when compared to larger aircraft (*Gursul, 2004*). This condition causes the models used in software such as Digital DATCOM to fall down when dealing with very small aircraft such as the mini-UAV.

Alternatively the coefficients may be estimated in flight. For example the work of Salman

et al (*Salman et al.*, 2006) gives a method for identifying a non-linear state-space model of the mini-UAV. These methods require accurate measurement of the rotation rates and accelerations for model estimation.

In the current application this is not possible. The purpose of the model is to bridge gaps in the attitude parameter estimates.

Simplified Model

In this work a simplified approach is developed which reduces the number of coefficients.

We know that the angles of sideslip and attack are proportional to the rotation rates p , q and r . Simplifying 5.19 we arrive at the model used by (*Salman et al.*, 2006);

$$\begin{aligned}
 L &= L(p, r, \delta_{ail}, \delta_{rud}, \delta_{th}) = l_p p + l_r r + l_{\delta_{ail}} \delta_{ail} + l_{\delta_{rud}} \delta_{rud} + l_{\delta_{th}} \delta_{th} \\
 M &= M(q, \delta_{ele}, \delta_{th}) = m_q q + m_{\delta_{ele}} \delta_{ele} + m_{\delta_{th}} \delta_{th} \\
 N &= N(p, r, \delta_{ail}, \delta_{rud}, \delta_{th}) = n_p p + n_r r + n_{\delta_{rud}} \delta_{rud} + n_{\delta_{th}} \delta_{th}
 \end{aligned} \tag{5.20}$$

Where the l , m , and n , terms are approximations of the aerodynamic derivative coefficients.

We further assume that the primary torque acting to slow the roll of the UAV is proportional to the roll rate and the primary torque acting to slow the yaw of the UAV is proportional to the yaw rate. That is that $l_r r \approx 0$ and $n_p p \approx 0$. The low Reynolds number means that aerodynamic forces will return the rotation rate to zero very quickly after a control input. The $l_p p$ and $n_r r$ terms will therefore be large and negative.

Having made this assumption the aerodynamic model of the torques is comprised of two parts. One part is a torque which acts to restore the UAV to a zero rotation rate. It is

proportional to the rotation rate. The other part is a torque which acts to increase the rotation rate. It is proportional to the control inputs.

$$\begin{aligned}
 L &= L(p, r, \delta_{ail}, \delta_{rud}, \delta_{th}) = l_p p + l_{\delta_{ail}} \delta_{ail} + l_{\delta_{rud}} \delta_{rud} + l_{\delta_{th}} \delta_{th} \\
 M &= M(q, \delta_{ele}, \delta_{th}) = m_q q + m_{\delta_{ele}} \delta_{ele} + m_{\delta_{th}} \delta_{th} \\
 N &= N(p, r, \delta_{ail}, \delta_{rud}, \delta_{th}) = n_r r + n_{\delta_{rud}} \delta_{rud} + n_{\delta_{th}} \delta_{th}
 \end{aligned} \tag{5.21}$$

Combining the equations of motion 5.16 and the aerodynamic model of the torques 5.21 we get the final model for identification:

$$\begin{aligned}
 \dot{p} = \frac{1}{I_x I_z - I_{xz}^2} \{ & I_z [(l_p p + l_{\delta_{ail}} \delta_{ail} + l_{\delta_{rud}} \delta_{rud} + l_{\delta_{th}} \delta_{th}) + (I_y - I_z) q r] + \\
 & I_{xz} [(n_r r + n_{\delta_{rud}} \delta_{rud} + n_{\delta_{th}} \delta_{th}) + \\
 & (I_x - I_y + I_z) p q - I_{xz} q r] \}
 \end{aligned} \tag{5.22}$$

$$\dot{q} = \frac{1}{I_y} [(m_q q + m_{\delta_{ele}} \delta_{ele} + m_{\delta_{th}} \delta_{th}) + p r (I_z - I_x) + (r^2 - p^2) I_{xz}] \tag{5.23}$$

$$\begin{aligned}
 \dot{r} = \frac{1}{I_x I_z - I_{xz}^2} \{ & I_x [(n_r r + n_{\delta_{rud}} \delta_{rud} + n_{\delta_{th}} \delta_{th}) + (I_x - I_y) p q] + \\
 & I_{xz} [(l_p p + l_{\delta_{ail}} \delta_{ail} + l_{\delta_{rud}} \delta_{rud} + l_{\delta_{th}} \delta_{th}) + \\
 & (I_y - I_x - I_z) q r + I_{xz} p q] \}
 \end{aligned} \tag{5.24}$$

The inertia matrix I , coefficients l , m , n , and control inputs δ_{ail} , δ_{ele} , δ_{rud} , δ_{thr} are required as inputs to the model.

5.4.6 Model Inputs

Inertia Matrix

The inertia matrix, I , can be determined experimentally or via mathematical models of the UAV mass distribution. For the small UAV the experimental method is straightforward, accurate and preferred.

Experimental estimation of the inertia parameters is based on measuring the period of compound and bifilar pendulums - for example, (*Jardin and Mueller, 2007*) and (*Bottasso et al., 2009*).

The procedure used for the estimation of the inertia matrix of the K-series UAVs in this work was published in (*Ou et al., 2008*).

The effect of increased inertia is to increase the ‘lag’ of the UAV’s response to control input since more torque is required to accelerate the rotation of the UAV. Similarly larger inertia will increase the time taken to achieve trimmed flight after a control input since the aerodynamic torques cannot reverse the effects of a control input as quickly.

Control Inputs

In this work the control surface deflection and thrust are not measured directly. Instead the input to the actuators used to move the surfaces and throttle is measured.

These actuators are servo motors with a ‘Pulse Position Modulation’ (PPM) input. The position of the actuator, and by inference the thrust or control surface deflection, is proportional to the width of an input pulse which may vary from 1-2ms. This pulse is

received by the servo at 50 Hz giving measurements of δ_{ail} , δ_{rud} , δ_{ele} and δ_{th} ten times faster than the GNSS attitude system update.

A calibration is used to map the servo input (in ms) to control surface deflection (in radians) or thrust (in Newtons). In this work the calibration of the aileron, rudder and elevator deflections was undertaken in a wind tunnel at various airspeeds to check the deflection angle is unaffected by the force applied by an increasing airflow over the control surface. At airspeeds up to 30 ms^{-1} the effect on the control surface deflection was negligible.

The control input pulses can be measured by hardware either mounted onboard the UAV or at a ground station. There is therefore no need to add any hardware to the UAV itself.

Coefficients

The approximations to the stability coefficients l_p , m_q and n_r used in the model will need to be large and negative to model a large restoring torque on the UAV after a control input.

If they are too large the predicted resorting torque will be too large and the model will not be stable. If they are too small the model will not predict a return to trimmed flight for a long time after control input. From experience and knowing the Reynolds number of a small UAV is small, this does not reflect reality.

In this work the approximations to the stability coefficients have been selected to provide a stable model in combination with the measured inertia matrix while providing as fast a return to stable flight as possible.

For the present research the assumption is made that the approximations to the control coefficients are constant with respect to the control inputs. This is true if the control inputs are kept small.

If the approximations to the control coefficients are too large the model will be unstable

since the predicted torque and acceleration will be too large to be countered by the stabilising aerodynamic torques. If they are too small the influence of the modelled control input will be too small to allow the model to reflect reality. In the proposed method the control coefficients should be selected to match the model output to a fixed ambiguity solution after signal tracking resumes.

5.4.7 Time-Stamping and Datalogging

In this work the servo inputs were logged and each input pulse time-stamped using GPS time. Accurate time stamping is essential to accurately align the dynamic model with the GNSS attitude system.

A basic stand alone GPS position gives a time solution to within $50\mu\text{s}$. This is true even with substantial code biases. A time-stamp error of $50\mu\text{s}$ will lead to a negligible attitude error even at very high rotation rates.

The hardware required to measure, time-stamp and log the control inputs is the only additional hardware required on the mini-UAV to implement the technique proposed in the current work. The time-stamp and logging equipment will be necessary for other elements of the UAV payload and so the only addition in most cases will be a low cost and lightweight circuit to measure the pulse time.

5.4.8 Attitude Modelling Summary

- Kinematic models can provide a prediction of the change in platform attitude over time without requiring control inputs and with only one calculation.
- A constant angular velocity model is suitable for constant attitude flight modes and constant rate turns. A constant angular acceleration model is suitable for constant attitude, constant rate turns and for transition into / out of a turn.

-
- A dynamic model predicts the torques acting the UAV. Through equations of motion the torques are then converted to rotational accelerations.
 - The torques are predicted using an aerodynamic model. Dimensionless coefficients are used to convert rotation rates and control inputs into relaxing and disturbing torques.
 - The dimensionless coefficients are traditionally determined using computational fluid dynamics or experimental methods. The first method breaks down when modelling the turbulent flow around a mini-UAV. The second requires an accurate attitude estimate throughout all manoeuvres. This is not possible in the survey UAV application.
 - In this work assumptions are made to allow the dimensionless coefficients to be chosen to match the attitude estimate at the end of a signal outage to the ambiguity fixed solution.

5.5 Algorithms

5.5.1 Bridging Signal Outages

The roll, pitch and yaw of the UAV is predicted using the kinematic or dynamic models until carrier phase tracking resumes.

For the kinematic models the angular velocity or angular acceleration is integrated with respect to time to give the predicted change in attitude.

For the dynamic model the angular acceleration is predicted at each discrete epoch where a control input is measured. The accelerations are then twice integrated over time to predict the change in attitude. Use of the dynamics mode is depicted in Figure 5.3.

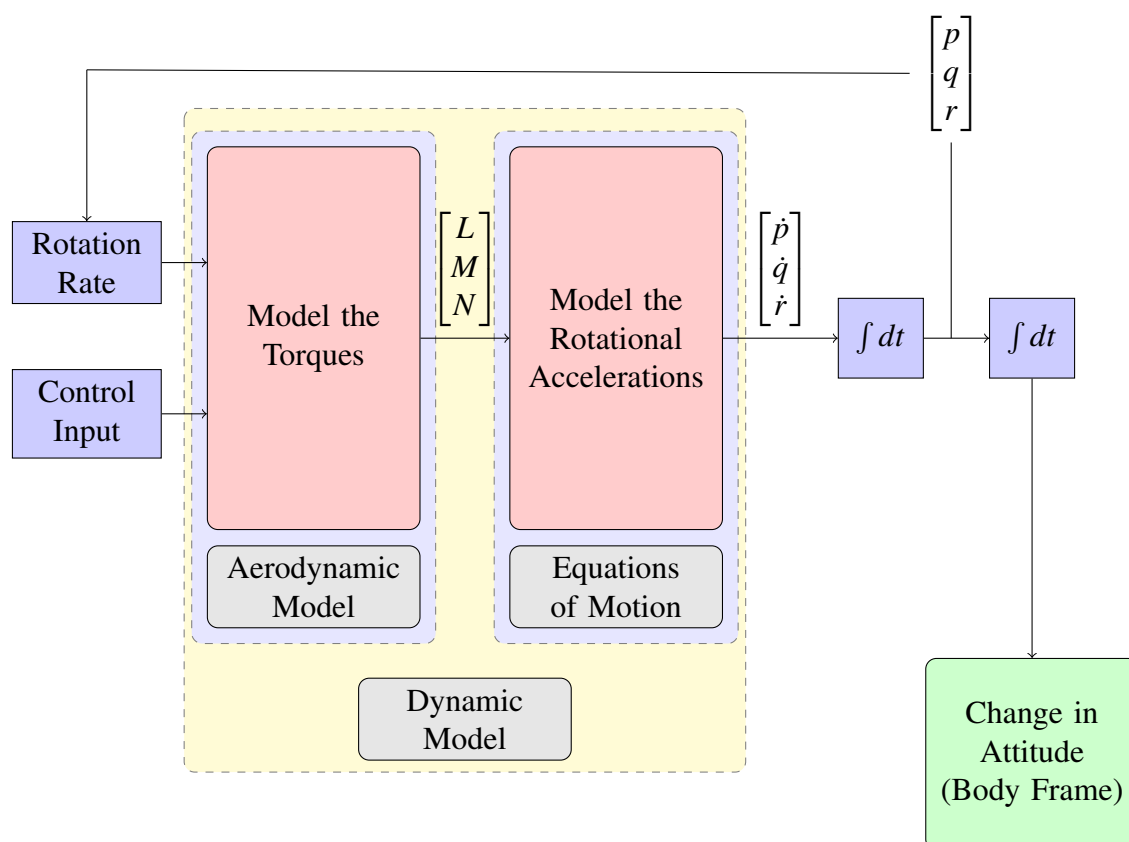


Figure 5.3: Use of the Dynamic Model

5.5.2 Cycle Slip Correction

The attitude dynamic or kinematic models are used to adjust the triple difference observable to leave only cycle slips for detection and correction.

So long as the relationship given in Equation 5.25 is true, half cycle slips can be detected.

$$\delta\nabla\Delta\phi_{ab}^{ij} - (\Delta(\delta\nabla\Delta\rho_{ab}^{ij}) + \varepsilon(\delta\nabla\Delta\phi)) < 0.5 \quad (5.25)$$

The triple difference geometric range $\delta\nabla\Delta\rho_{ab}^{ij}$ is calculated from an estimate of the change in attitude over the time separating the triple differenced epochs.

The baseline components $x(t_1)$, $y(t_1)$, $z(t_1)$ are computed from the roll, pitch and yaw using the inverse of the rotation matrix 3.21;

$$\mathbf{r}_{\parallel} = (R_l^b)^{-1} \mathbf{r}_b \quad (5.26)$$

Where \mathbf{r}_b is known and

$$\mathbf{r}_e = \begin{bmatrix} x(t) \\ y(t) \\ z(t) \end{bmatrix} = (R_l^e)^{-1} \left[(R_l^b)^{-1} \mathbf{r}_b \right] \quad (5.27)$$

If $x(t_0)$, $y(t_0)$, $z(t_0)$ and $x(t_1)$, $y(t_1)$, $z(t_1)$ are the baseline components at the first and second epochs used in the triple difference then;

$$\begin{aligned} \delta \nabla \Delta \rho_{ab}^{ij} &= \nabla \Delta \rho(t_1)_{ab}^{ij} - \nabla \Delta \rho(t_0)_{ab}^{ij} \\ &= \left[(\rho(t_1)_a^i - \rho(t_1)_b^i) - (\rho(t_1)_a^j - \rho(t_1)_b^j) \right] - \left[(\rho(t_0)_a^i - \rho(t_0)_b^i) - (\rho(t_0)_a^j - \rho(t_0)_b^j) \right] \end{aligned} \quad (5.28)$$

With;

$$\rho(t)_a^i = \sqrt{(X(t)^i - x(t))^2 + (Y(t)^i - y(t))^2 + (Z(t)^i - z(t))^2} \quad (5.29)$$

Where $X(t)$, $Y(t)$ and $Z(t)$ are the satellite positions at time t .

If $\Delta(\delta \nabla \Delta \rho_{ab}^{ij})$ and $\varepsilon(\delta \nabla \Delta \phi)$ are small then the cycle slip $\delta \nabla \Delta N_{ab}^{ij}$ is;

$$\delta\nabla\Delta N_{ab}^{ij} = \left[\delta\nabla\Delta\phi_{ab}^{ij} - (\Delta(\delta\nabla\Delta\rho_{ab}^{ij}) + \varepsilon(\delta\nabla\Delta\phi)) \right]_{0.5} \quad (5.30)$$

Where $[\bullet]_{0.5}$ represents rounding to the nearest half integer.

The triple and double difference observables can now be corrected using $\delta\nabla\Delta N_{ab}^{ij}$.

The process is depicted in Figure 5.4.

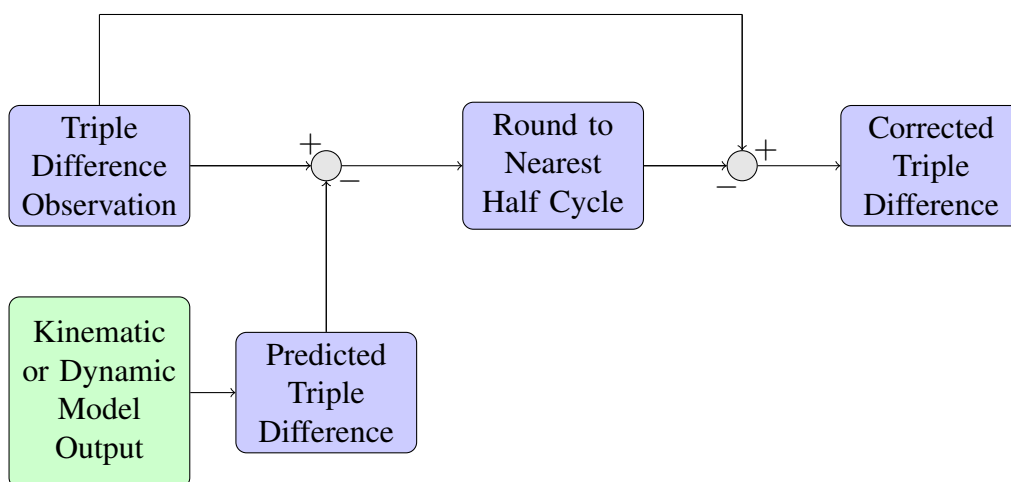


Figure 5.4: Cycle Slip Correction

5.5.3 Using Half Cycle Ambiguous Carrier Phase

The cycle slip corrected triple differenced carrier phase observable is used to obtain estimates of the platform angular velocity. These are integrated over time to estimate the change in platform attitude and a float ambiguity solution. Ambiguity resolution can then be attempted.

The integration can be performed forwards or backwards in time. Forwards it provides an estimate of the change in platform attitude which is likely to be significantly more accurate than that available from the kinematic or dynamic models. If it remains suffi-

ciently accurate it can be used to provide a double difference float solution of the integer ambiguities when full cycle carrier phase tracking resumes.

Backwards in time from an ambiguity fixed attitude solution the integration provides an estimate of the platform attitude during half cycle carrier phase tracking. The estimated attitude is again likely to be significantly more accurate than that available from the kinematic or dynamic models and may be good enough for georeferencing purposes.

The triple difference observable is linear with respect to the change in relative position of the antennas. Scaling the observations with the time between measurement epochs Δt , the inter antenna velocity \mathbf{v} is given by:

$$\lambda \frac{\delta \nabla \Delta \phi_{ab}^{ij}}{\Delta t} = A \cdot \mathbf{v} + \delta \nabla \Delta \epsilon_{ab}^{ij} \quad (5.31)$$

Where A is the design matrix, consisting of the double difference unit vectors, as introduced in Section 3.3.3, Equation 3.29. The antenna relative velocity is now solved for using a standard least squares estimator.

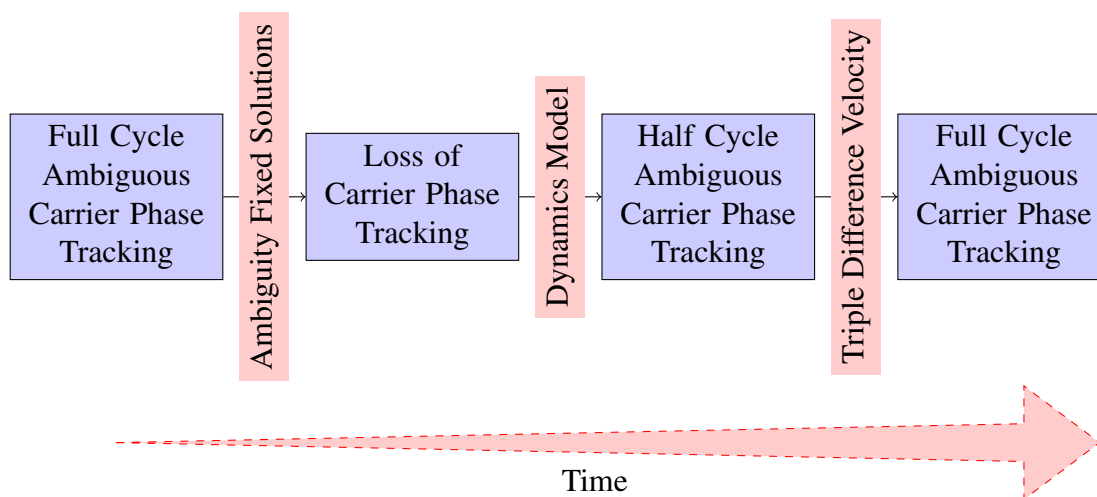


Figure 5.5: Use of the Triple Difference Velocity (Forwards)

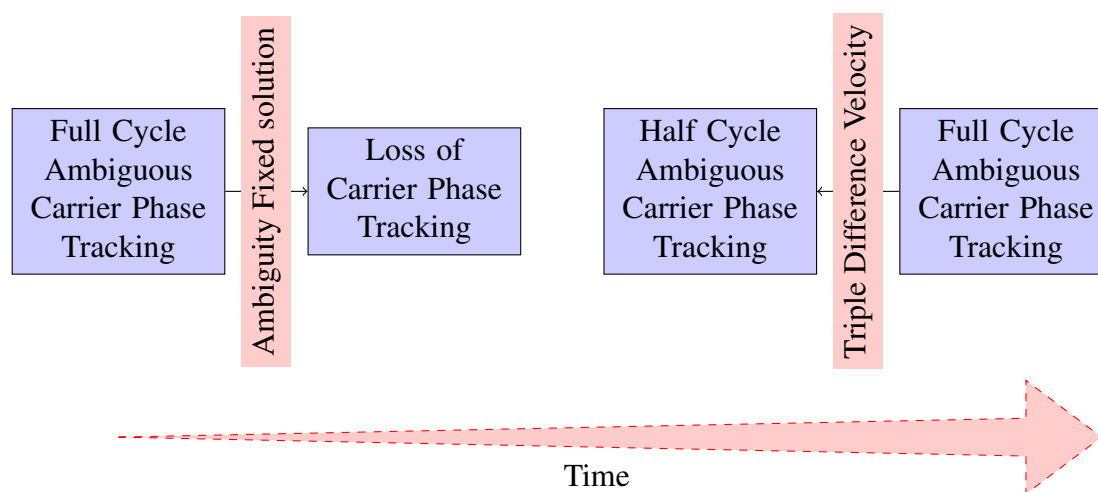


Figure 5.6: Use of the Triple Difference Velocity (Backwards)

5.6 Conclusion

In this chapter three algorithms have been developed for use in case of GNSS signal tracking problems.

The first uses a kinematic or dynamic model to predict the mini-UAV attitude during signal outages. This allows a graceful degradation of the attitude solution when carrier phase tracking is lost. It also provides an attitude solution which may be used as the float solution when full carrier phase tracking resumes.

The second uses the output from kinematic or dynamic models to remove cycle slips from the triple difference carrier phase observation. The modelled change in attitude is used to compute a predicted triple difference geometric range. When this is subtracted from the triple difference observable only cycle slips will remain which can then be identified.

The third algorithm uses the cycle slip corrected triple difference carrier phase observable to compute the change in attitude at each epoch. This is possible even with half cycle ambiguous carrier phase measurements. The estimated attitudes are used to form a float solution for use in half integer ambiguity resolution.

The following questions remain to be answered;

- How accurate is the rotational velocity estimated using the triple difference observable with half and full cycle ambiguous measurements?
- How accurate does the attitude prediction from a kinematic or dynamic model need to be to correct for half cycle slips under normal mini-UAV flight conditions?
- How well do the kinematic and dynamic models match real UAV flight dynamics? For how long do they remain valid?
- What is the success rate of half cycle ambiguity resolution using the triple difference observable?

These questions will be addressed in the final chapter.

Chapter 6

Algorithm Testing

6.1 Introduction

In Chapter 5 three novel algorithms were developed for bridging GNSS signal outages, identifying and correcting half cycle slips and using half cycle ambiguous carrier phase measurements. In this chapter the algorithms and the methods contained within them are tested.

First the use of the triple difference observable to estimate the platform change in attitude is examined using ‘real world’ static GPS measurements. Static measurements allowed analysis of the precision and drift of the attitude estimates over time.

Next the use of the geometry corrected triple difference observable to detect cycle slips is investigated. In the current application the antennas relative motion can only come from a rotation of the baseline between them. The accuracy requirement for the estimate of this baseline rotation is examined and a lower limit derived for the specific case of a 1m baseline and a half cycle slip.

Finally the kinematic and dynamic models will be tested using the output from a UAV mounted Inertial Measurement Unit (IMU). Their suitability for use in correcting cycle slips and bridging signal outages will be examined and their limitations discussed.

6.2 Angular Velocity Estimation Using the Triple Difference Observable

In this work the linear relative velocity between antennas is estimated from the triple difference observable (via Equation 5.31).

Using *a priori* knowledge of the baseline length it is possible to directly estimate the angular velocity. However using that approach introduces angular velocity errors through any error in the measurement of the baseline length.

Consequently the approach taken is to estimate linear velocities at each measurement epoch and convert a derived estimate of the change in position to an estimate of the change in attitude when required.

In this section the precision and accuracy of the linear velocity estimates derived using the triple difference carrier phase will be examined. The precision is quantified using the standard deviation as in Chapter 4.

6.2.1 Static Tests

To examine the performance of the triple difference observable as a measure of angular velocity a dataset generated using the GNSS hardware simulator was used. In the simulated scenario one antenna is static 1 metre away from another on a level baseline.

The purpose of this test is to quantify the accuracy and precision of the rotational velocity estimates over a typical short baseline. The test is performed under good conditions with no multipath and properly tracked phase and code.

The results of processing this dataset are given in Tables 6.1 and 6.2. The results are separated into plan and height (yaw and roll/pitch). The satellite geometry can be expected to make the height (roll / pitch) results worse than the plan (yaw) results.

Table 6.1: *Linear Velocity Estimates using the Carrier Phase Triple Difference (Hardware Simulator)*

	Plan	Height
Accuracy	$8.0 \times 10^{-5} \text{ ms}^{-1}$	$2.7 \times 10^{-4} \text{ ms}^{-1}$
Precision	$8.1 \times 10^{-3} \text{ ms}^{-1}$	$1.6 \times 10^{-2} \text{ ms}^{-1}$

Table 6.2: *Rotational Velocity Estimates using the Carrier Phase Triple Difference (Hardware Simulator)*

	Yaw	Roll / Pitch
Accuracy	$4.8 \times 10^{-3} \text{ }^\circ/\text{s}$	$1.6 \times 10^{-2} \text{ }^\circ/\text{s}$
Precision	$0.3 \text{ }^\circ/\text{s}$	$0.87 \text{ }^\circ/\text{s}$

To validate these results the data collected on a ‘real world’ short baseline were processed in the same manner. The experimental setup is described in Section 4.4 and the results are given in Tables 6.4 and 6.3.

Table 6.3: *Linear Velocity Estimates using the Carrier Phase Triple Difference (‘Real World’)*

	Plan	Height
Accuracy	$4.1 \times 10^{-5} \text{ ms}^{-1}$	$1.4 \times 10^{-4} \text{ ms}^{-1}$
Precision	$2.0 \times 10^{-2} \text{ ms}^{-1}$	$2.7 \times 10^{-2} \text{ ms}^{-1}$

Table 6.4: Rotational Velocity Estimates using the Carrier Phase Triple Difference ('Real World')

	Yaw	Roll / Pitch
Accuracy	$1.8 \times 10^{-3} \text{ }^\circ/\text{s}$	$5.0 \times 10^{-3} \text{ }^\circ/\text{s}$
Precision	$0.6 \text{ }^\circ/\text{s}$	$1.5 \text{ }^\circ/\text{s}$

The small biases seen in the velocity estimates will accumulate and appear as a drift in the position or attitude estimates. Figure 6.1 shows this drift in the attitude over time using the 'real world' short baseline, static dataset.

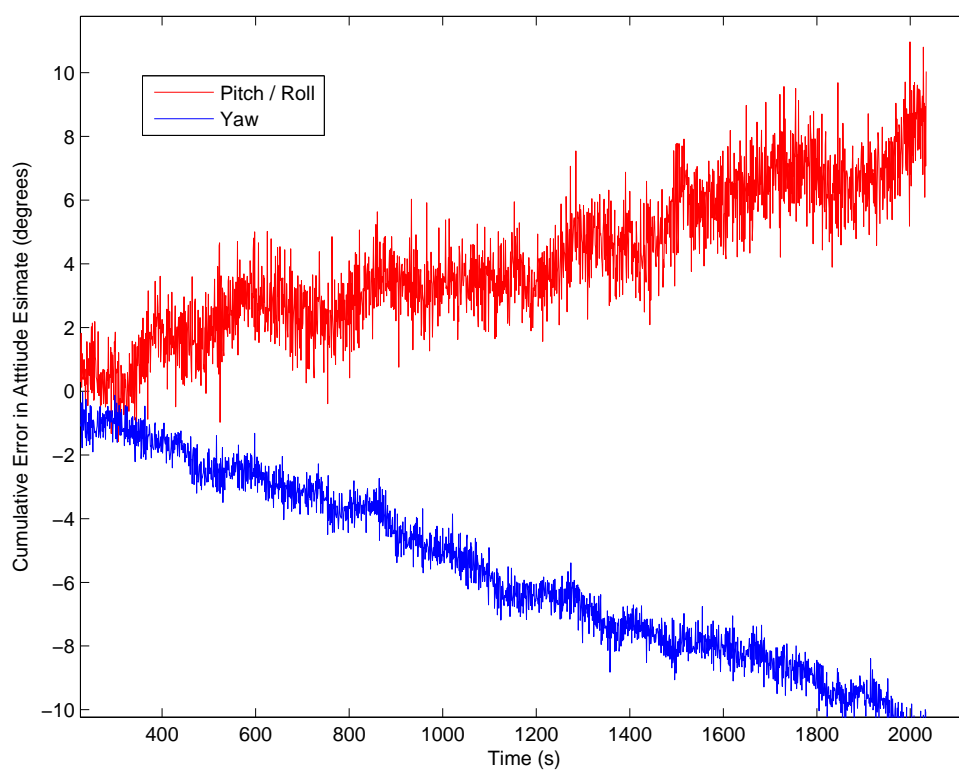


Figure 6.1: Drift in the Attitude Derived from Triple Difference Angular Velocity Estimates

6.2.2 Simulated UAV Flight

The third dataset examined is the zero-baseline simulated data used in Chapter 4, Section 4.6. This dataset was designed to reproduce the problems seen in the real UAV data by featuring turns which induce signal tracking problems followed by a period of straight and level flight for recovery.

The purpose of this test is to allow comparison of the linear velocity estimates obtained using variable quality data on a moving baseline with those obtained in the static test.

By definition the linear velocity between the antennas in a zero baseline test is zero. The rotational velocity is undefined. This allows simple recovery of the linear velocity accuracy and precision for comparison with the previous static test.

In Figure 6.2 the error in the velocity estimates for a section of the dataset is shown. Estimates obtained using half cycle ambiguous carrier phase measurements are shown in red. Table 6.5 gives statistics for the entire dataset.

Table 6.5: Linear Velocity Estimates using the Carrier Phase Triple Difference, Simulated UAV Dataset

	Plan	Height
Accuracy	$3.3 \times 10^{-5} \text{ ms}^{-1}$	$3.4 \times 10^{-4} \text{ ms}^{-1}$
Precision	$1.4 \times 10^{-3} \text{ ms}^{-1}$	$2.7 \times 10^{-2} \text{ ms}^{-1}$

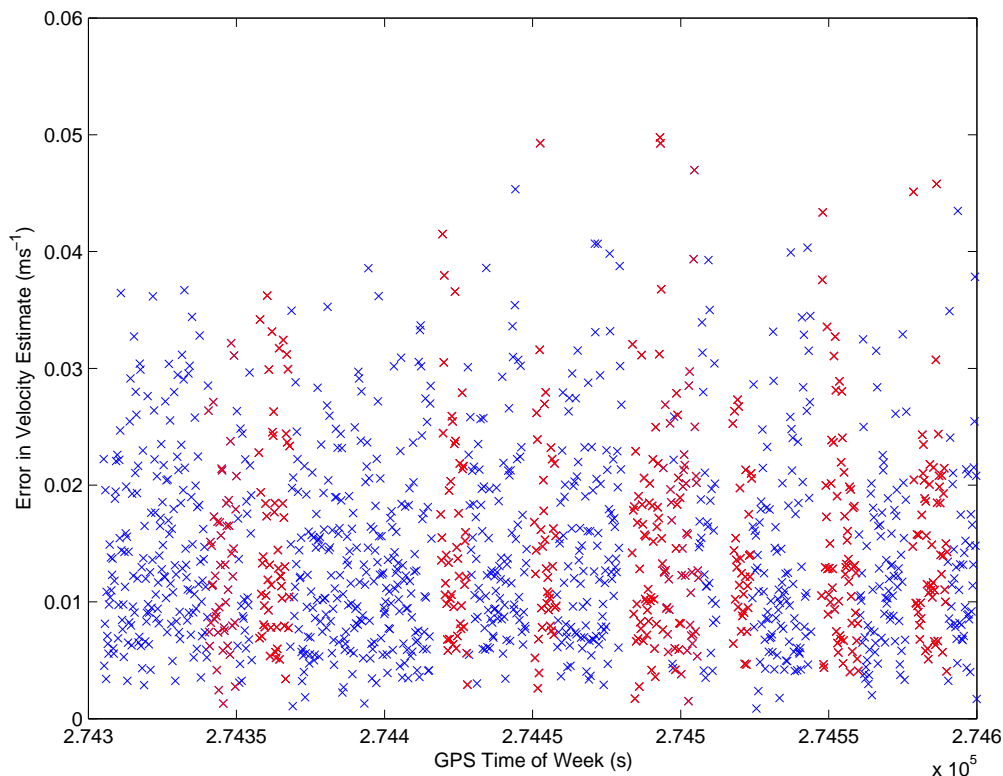


Figure 6.2: Error in the Triple Difference Velocity Estimates from the Simulated UAV Dataset. Half Cycle Ambiguous Measurements in Red.

6.2.3 Discussion

The results above show that the triple difference carrier phase observable is capable of giving good linear and angular velocity estimates.

In both simulated and real environments low cost equipment gave relative velocity estimates with noise levels of around 2-3cm per second (standard deviation). Angular velocity estimates had a precision of around 1 degree per second on a 1m baseline. The satellite - receiver geometry means that the yaw estimates are more than twice as good as the pitch / roll estimates.

Small biases in the angular velocity estimates appear as drifts in the attitude estimates. Over time these drifts become significant. For the proposed algorithms the triple dif-

ference will only be used when half cycle ambiguous carrier phase measurements are all that are available. This situation lasts for around 10 seconds after a signal outage. Over this time the drift in the angular velocity estimates is insignificant compared to their precision.

These results show that the triple difference attitude estimates are not precise enough for georeferencing. Within the short (10s) timescales being considered they are considerably more precise and equally accurate compared with those achieved using the code dominated ‘float’ estimates.

No significant loss of accuracy or precision was observed when using half cycle ambiguous phase observations (Figure 6.2).

6.3 Half Cycle Slip Correction

In this section the correction of half and full cycle slips is explored. The aim is to determine the effect of error in the attitude prediction on the ability to detect and resolve cycle slips.

For the purposes of this section a simple scenario was implemented on the GNSS hardware simulator. One simulated antenna circles the other at 1m distance and at constant angular velocity. Again the uBlox LEA-5T low cost receiver was used to make measurements from the simulated RF signal.

A short example of the triple difference observables which are formed from this data is given in Figure 6.3. A half cycle slip is artificially inserted into one observable 97 seconds into the example.

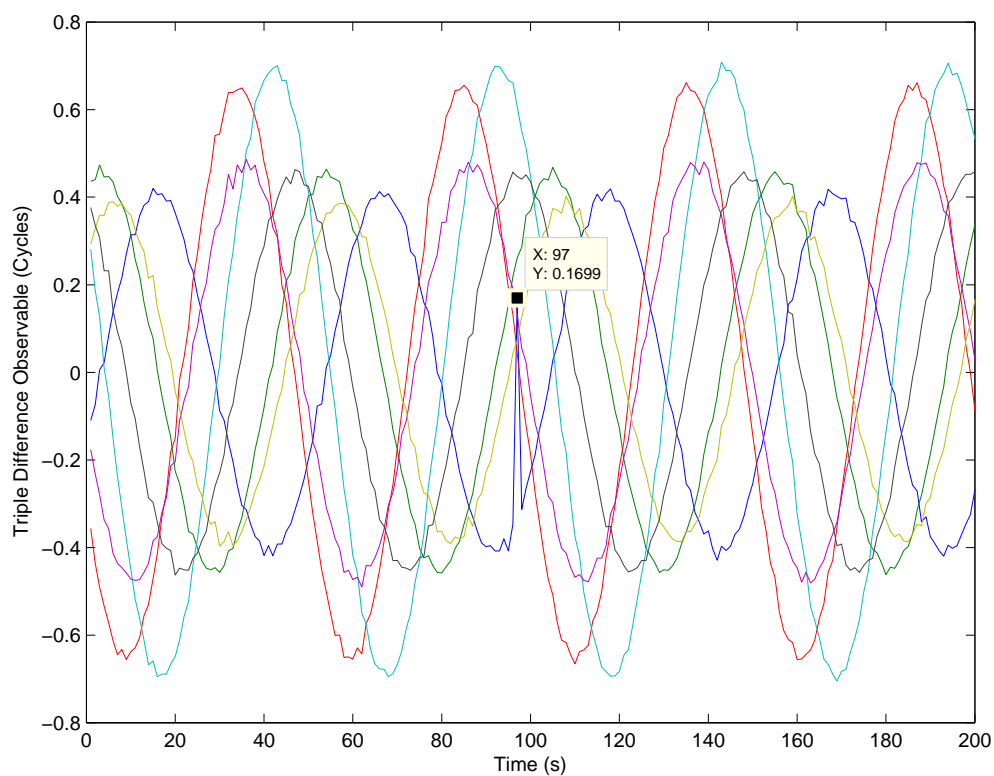


Figure 6.3: Circular Dataset, Triple Difference Observable. A half cycle slip appears in one observable (blue) at around 97 seconds.

The same set of triple difference observables, corrected for angular velocity, is shown in Figure 6.4. Use of the hardware simulator means that the trajectory is perfectly known and the velocity component of the triple difference observables can be removed completely. It can be seen that the cycle slip is now clearly identifiable.

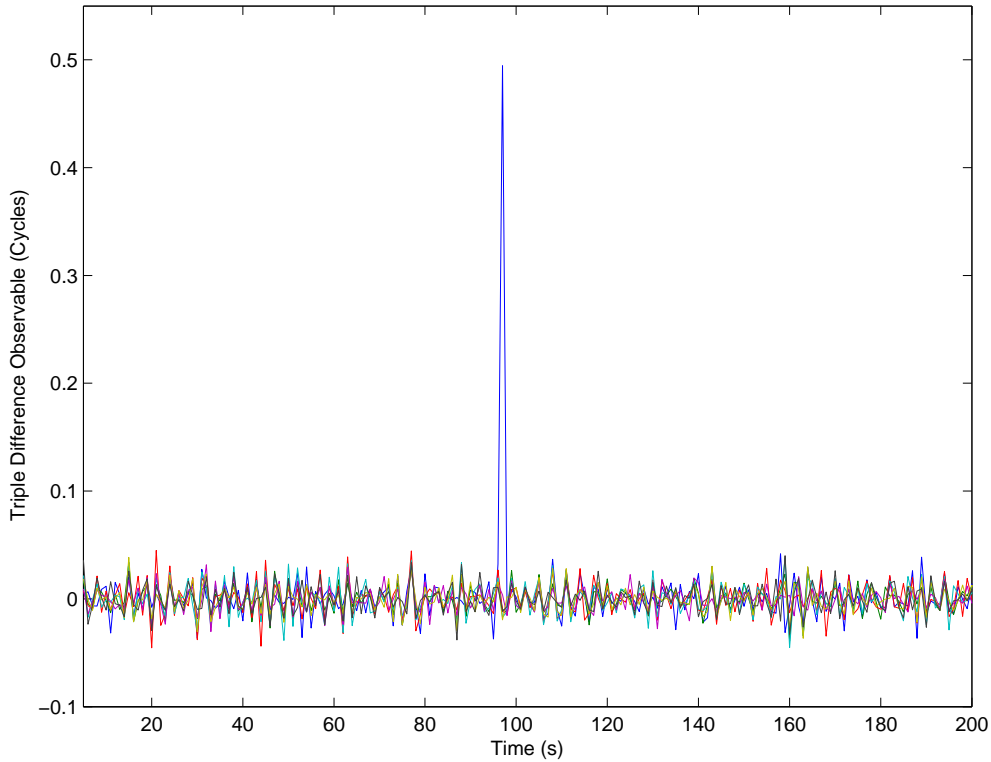


Figure 6.4: *Circular dataset, triple difference observable corrected for angular velocity. A half cycle slip appears in one observable (blue) at around 97 seconds.*

The standard deviation of the geometrically corrected triple difference observables ($\epsilon(\delta\nabla\Delta\phi)$) is 0.015 cycles. They will therefore make a minimal contribution to Equation 5.25 reproduced here:

$$\delta\nabla\Delta\phi_{ab}^{ij} - \lambda(\Delta(\delta\nabla\Delta\rho_{ab}^{ij}) + \epsilon(\delta\nabla\Delta\phi)) < 0.5 \quad (5.25)$$

All that remains is the error in the triple difference geometric correction which arises from the predicted attitude error ($\Delta(\delta\nabla\Delta\rho_{ab}^{ij})$). The magnitude of this error will vary for each triple difference observation. It will depend on the angle between the error vector and the double difference observation vector used in the design matrix.

This is depicted for two dimensions in Figure 6.5. An attitude error $\Delta\theta$ causes an error

vector $\Delta(\delta\nabla\Delta\rho)$. This is then projected onto the double difference observation vector to give the geometric error ($\Delta(\delta\nabla\Delta\rho_{ab}^{ij})$).

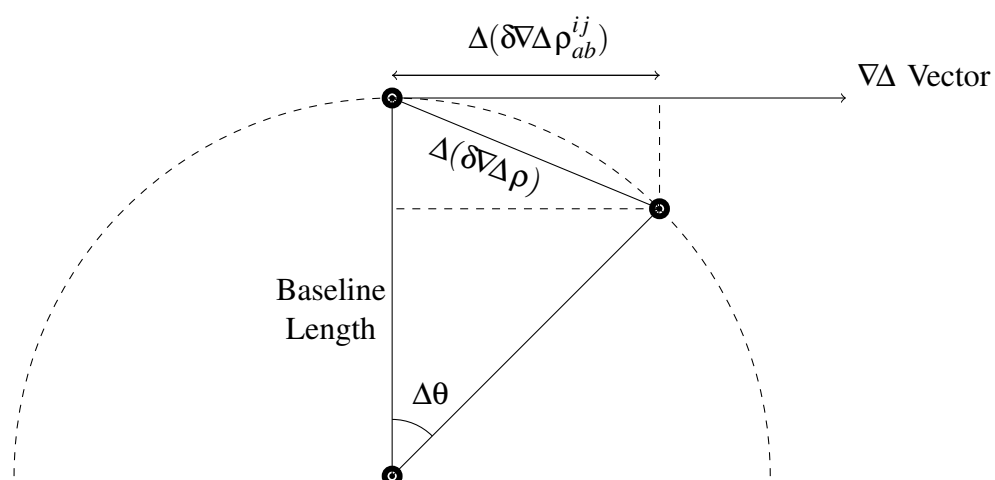


Figure 6.5: Error in the triple difference geometric correction which arises from the angular error $\Delta\theta$.

The situation depicted in in Figure 6.5 means that it is not possible to give a unique value for the maximum angular error which will allow Equation 5.25 to be satisfied. While it would be possible to calculate a value for the maximum angular error acceptable for each observation the approach taken in this work is to use the worst case scenario.

In the worst case the double difference observation vector is parallel to the error vector $\Delta(\delta\nabla\Delta\rho)$. This is depicted in Figure 6.6.

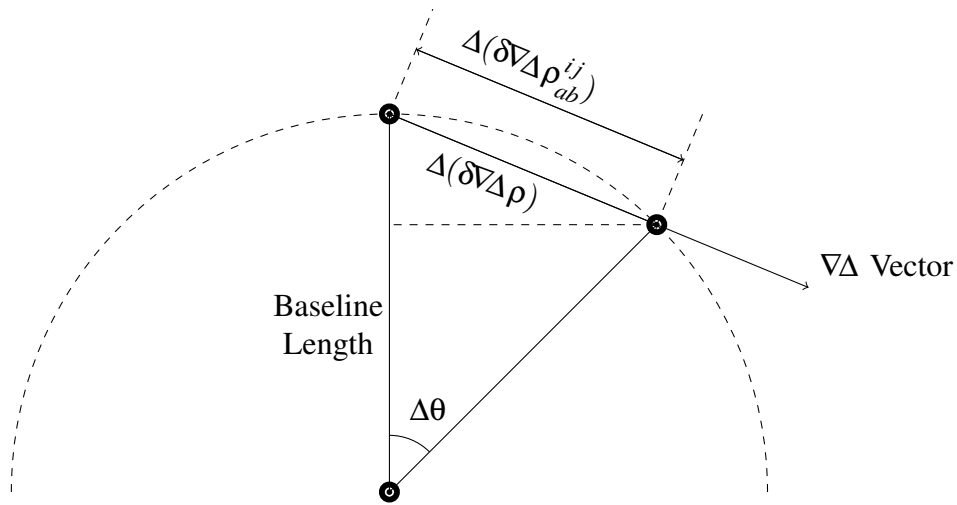


Figure 6.6: Worst case error in the triple difference geometric correction which arises from the angular error $\Delta\theta$.

The chord length $\Delta(\delta\nabla\Delta\rho)$ is;

$$\Delta(\delta\nabla\Delta\rho) = 2l \sin\left(\frac{\Delta\theta_{max}}{2}\right) \quad (6.1)$$

Where l is the baseline length. Rearranging for $\Delta\theta_{max}$ we have;

$$\Delta\theta_{max} = 2\sin^{-1}\left(\frac{\Delta(\delta\nabla\Delta\rho)}{2l}\right) \quad (6.2)$$

For a 1m baseline length and 0.015 cycle triple difference observation noise a total attitude error of 5.3° will satisfy Equation 5.25 even in the worst case.

This maximum total attitude error can be increased by lengthening the inter-antenna baseline however this will reduce the precision of the altitude estimates.

It also may be reduced to increase confidence in cycle slip detection. In this work however 5.3° is taken as a good indicative value for the purposes of examining the dynamic models.

6.4 Kinematic and Dynamic Modelling

In this section the kinematic and dynamic models developed in Chapter 5 will be implemented and tested. Sample UAV flight data is used to test their ‘real world’ ability to bridge GNSS tracking gaps and correct cycle slips.

6.4.1 Rotation Rate & Control Input Measurement

To examine the performance of the kinematic and dynamic models some measurement of the body axis rotation rates p , q and r will be needed.

This could be provided by a GNSS attitude system with a fixed ambiguity attitude solution. The disadvantage of this method is that to fully test the models an attitude /attitude rate estimate is required at all times, most importantly in periods of flight which are not straight and level. As has been seen this is not always possible.

A second option is to use an Inertial Measurement Unit (IMU) to directly measure p , q and r . High data rates and guaranteed availability of measurement in all flight modes makes the IMU an attractive choice for the purpose of testing the model outputs.

In this research an IMU is used to provide p , q and r measurements over the course of a dedicated mini-UAV flight. A Crossbow IMU440 unit forms part of the prototype survey payload of the K70 mini-UAV used in Chapter 4. The IMU440 is typical of the class of IMUs which can be flown on a mini-UAV and are theoretically capable of providing measurements of suitable quality for georeferencing purposes. Some important specification of the IMU440 are given in table 6.6. Details can be found in the datasheet (*Crossbow*, 2010).

The total payload weight flown on the K70 UAV is 1kg, the IMU440 constitutes more than half of this. It is also the single largest item in the payload bay.

Table 6.6: Crossbow IMU440 Inertial Measurement Unit

Weight	0.55 kg
Size	7.62 x 9.53 x 6.43 cm
Data Rate	100 Hz
Acceleration Range	$\pm 10g$
Rotation Rate Range	$\pm 400^\circ/s$
Rotation Rate Resolution	$0.02^\circ/s$
Rotation Rate In Run Bias Stability	$< 10^\circ/hr$

For the test flight the IMU was mounted to match the body axes as closely as possible. A ‘boresight’ rotation calibration from sensor to body axis is therefore unnecessary.

Since the GPS tracking performance is poor no attempt was made to integrate GPS and INS measurements. The IMU drifts therefore cannot be mitigated in this way. Instead the drift of each gyro was estimated from static periods before and after flight and the measurements corrected using this value. Gyro rate biases due to acceleration and temperature changes in flight remain unmitigated.

Angular acceleration was estimated from the angular rate output of the IMU. Noise in the IMU measurements propagates into the angular acceleration estimate and so an average of IMU rate measurements was used to derive the angular accelerations. The high rate IMU output meant that four IMU measurements could be used to derive the angular acceleration for each model update. Using any more IMU measurements would increase the risk of filtering out real angular accelerations.

Control inputs were measured using dedicated hardware as described in Section 5.4.6. They were timestamped and logged using the hardware which also logged the IMU measurements. All of the data from the flight was saved to a flash memory card and post-processed.

The control inputs were mapped to control surface angle and thrust force using calibrations performed in a wind tunnel at typical UAV flight speeds.

6.4.2 Test Flight

The flight test was performed within visual range of the pilot at a nominal 400ft (120m) above ground level. The temperature on the day was around 20°C and the winds were steady at less than 5kts (2.5ms^{-1}) throughout.

The K70 mini-UAV flew a series of circuits with frequent turns to remain within safe visual range of the pilot. On some lines deliberately exaggerated control inputs were sent to the UAV but the attitudes were kept within the limits of a normal survey flight.

A sample of the rotation rates measured by the Crossbow IMU440 is given in Figure 6.7.

A series of high frequency turns occur between 100 seconds and 130 seconds into the sample. This is followed by a positive and negative pitch event before a period of level flight from 150 seconds. After this the normal flight sequence is resumed.

The maximum rotation rate observed in this flight was around 100 degrees per second in roll.

Since they are not part of a normal survey flight, unusual flight modes were not included when examining the models performance for cycle slip detection and bridging GNSS signal outages.

The takeoff and landing phases were also not examined since the low airspeeds involved will adversely affect the dynamic model performance at times when the signal tracking performance can be expected to be good.

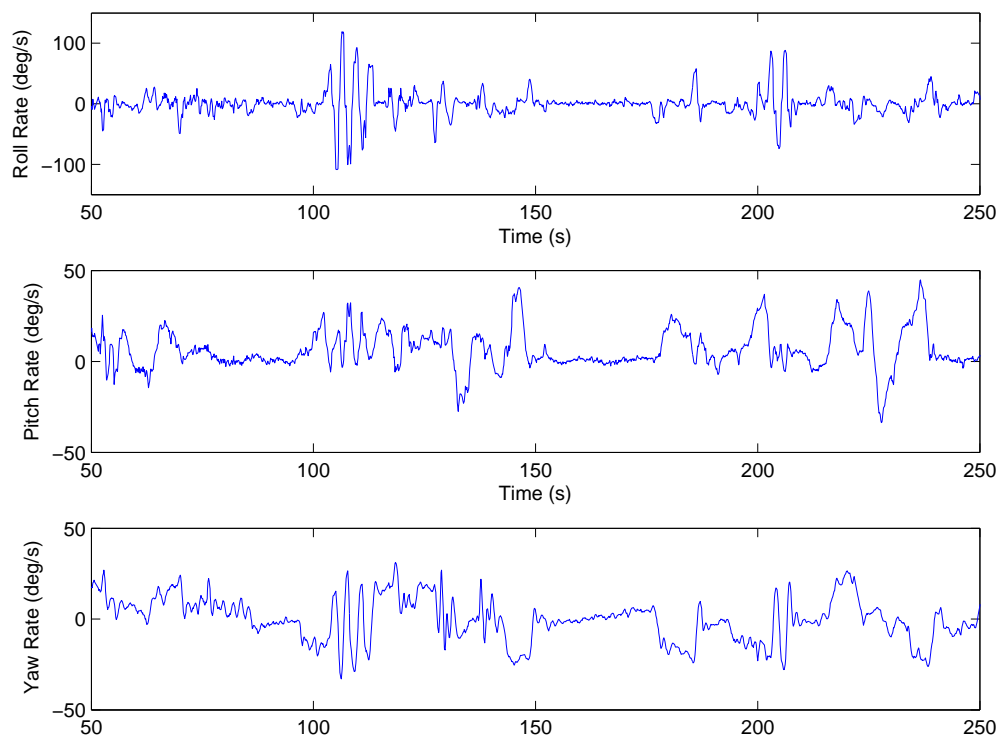


Figure 6.7: Rotation rate measured by a Crossbow IMU440 onboard a K70 mini-UAV.

In Figure 6.8 the aileron, elevator and rudder inputs for the same example period are shown. The throttle setting throughout this period is constant.

Again the coordinated rudder / aileron inputs forming high rate turns are seen after 100 seconds. At around 130 seconds into the example a rudder only input is performed.

The measurement noise associated with measuring the input pulse widths propagates into the control surface deflection estimates. In this research the standard deviation of the control surface deflection estimates when static is 0.22 degrees for ailerons, rudder and elevator. This noise further propagates into the dynamic model estimates.

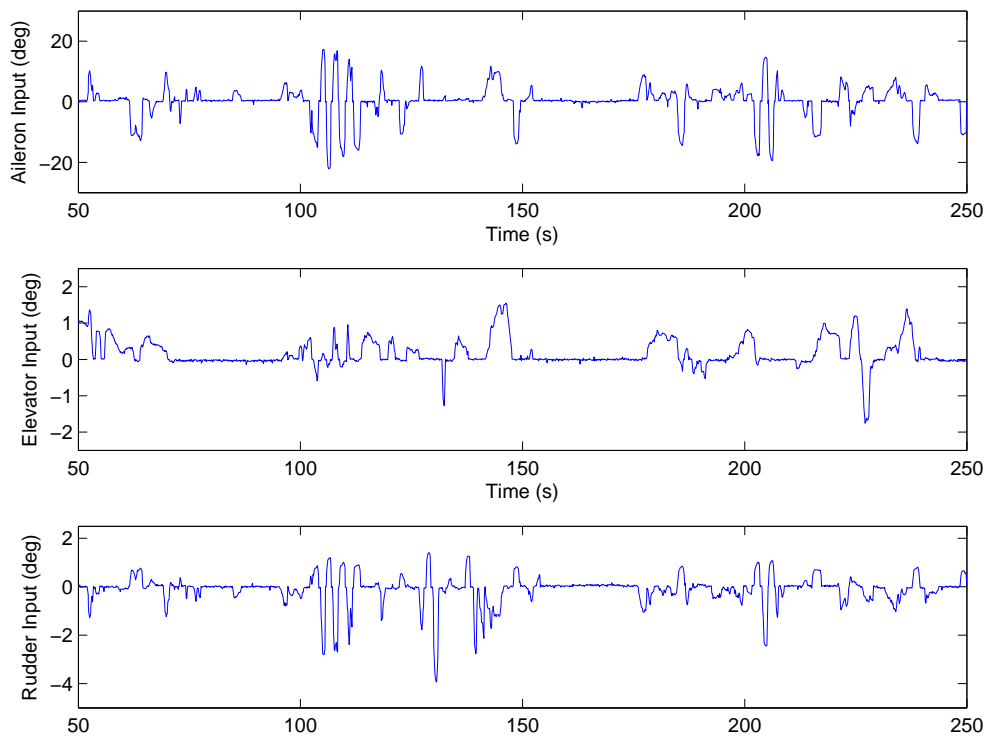


Figure 6.8: Control inputs to a K70 mini-UAV.

6.4.3 Cycle Slip Correction

In this section the suitability of the models for use in cycle slip correction will be investigated. The metric used is the difference between the IMU derived attitude change and the modelled attitude change over the time between GNSS epochs.

While the IMU output is far from perfect it is used as a ‘truth’ solution over the short time spans involved. It is expected, and observed in the datasets, that the gyro errors integrated over short periods will result in small attitude errors.

For 5Hz data as output from the uBlox LEA-5T the time between epochs is 0.2s. Other low cost receivers are limited to 1Hz data output and so for completeness the models will be examined over both 0.2s and 1s intervals.

In Section 6.3 a value of 5.3° was derived as the greatest total angular error for successful cycle slip detection over a 1m baseline.

Two possible baselines are now considered, one to measure roll and heading with antennas on the wingtips, the other with antennas near the nose and tail to measure pitch and heading.

In Table 6.7 the 95% confidence limit for the two baseline orientations is given. It can be seen that the best model (lowest confidence limit) is the dynamic model in both cases. In fact the dynamic model met the criteria in 94.7% of the cases for the Roll / Heading baseline and 97.4% of estimates for Pitch / Heading.

Table 6.7: *Modelled total attitude error 95% confidence limits (5Hz data rate).*

	Roll / Heading	Pitch / Heading
Constant Attitude Rate Model	5.95°	5.58°
Constant Attitude Acceleration Model	15.1°	8.39°
Dynamic Model	5.44°	4.72°

Table 6.8 shows the same limits for a 1Hz data rate. As expected all of the models perform significantly worse over the longer time between measurements. This time the dynamic model met the criteria in 50.0% of the cases for the Roll / Heading baseline and 47.7% of estimates for Pitch / Heading.

Table 6.8: *Modelled total attitude error 95% confidence limits (1Hz data rate).*

	Roll / Heading	Pitch / Heading
Constant Attitude Rate Model	22.8°	12.2°
Constant Attitude Acceleration Model	74.5°	45.2°
Dynamic Model	18.6°	17.2°

In practice the models will all show better performance for cycle slip detection than

indicated since the double difference observation vector will rarely be parallel to the error vector $\Delta(\delta\nabla\Delta\rho)$ and the worst case condition will not often be met.

6.4.4 Bridging GNSS Signal Outages

The second application for the kinematic and dynamic models is bridging GNSS signal outages. In this section their performance over time will be examined.

Inaccuracies in the rotation rates predicted by the models will result in a drift in the attitude solution when they are integrated over time. For the purposes of comparison the rotation rates output by the IMU440 will be taken as truth, and the attitudes obtained by integrating them over time will be the baseline against which the models will be tested.

Each of the models have been used to predict the change in attitude over time (the ‘integration period’) and their outputs at the end of the period compared to that given by the IMU. The ‘integration period’ corresponds to the length of data gap which can be covered.

The dynamic model is updated at each control input whereas the kinematic models use the same angular rate or angular acceleration throughout the integration period. For this test a new ‘integration period’ is started at each control input to give an error value for each model at each control measurement epoch.

Figures 6.9, 6.10 and 6.11 show the mean error over the entire dataset for each model and for integration periods of up to 10 seconds.

The errors are plotted on a \log_{10} scale to emphasise the differences at low integration periods. The errors for all models have been observed to increase in a linear fashion with integration time.

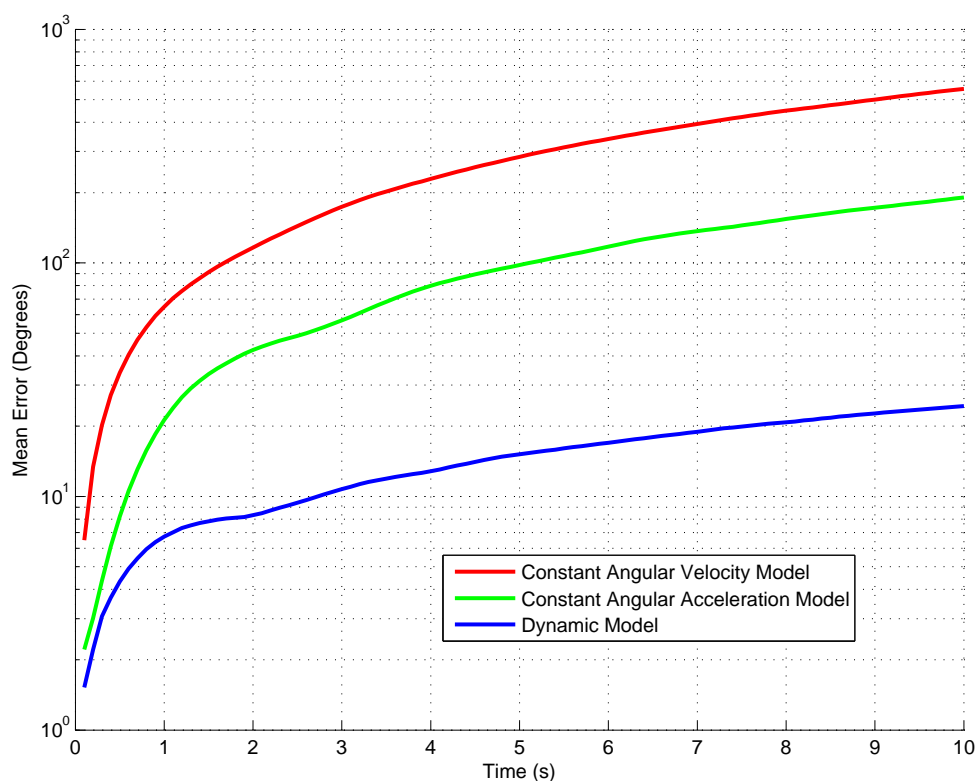


Figure 6.9: Relationship between model roll output and IMU for integration times up to 10seconds.

In the body roll axis the dynamic model is significantly better than either of the kinematic models over all integration periods. As seen in the cycle slip detection application, for low integration periods the constant rate model closely matches the performance of the dynamic model.

After 10 seconds the dynamic model has drifted from the IMU prediction by an average of 24° compared to 190° and 555° for the constant rate and constant acceleration kinematic models. After a more typical signal outage of 2 seconds duration the models have drifted by 8° , 42° and 116° respectively.

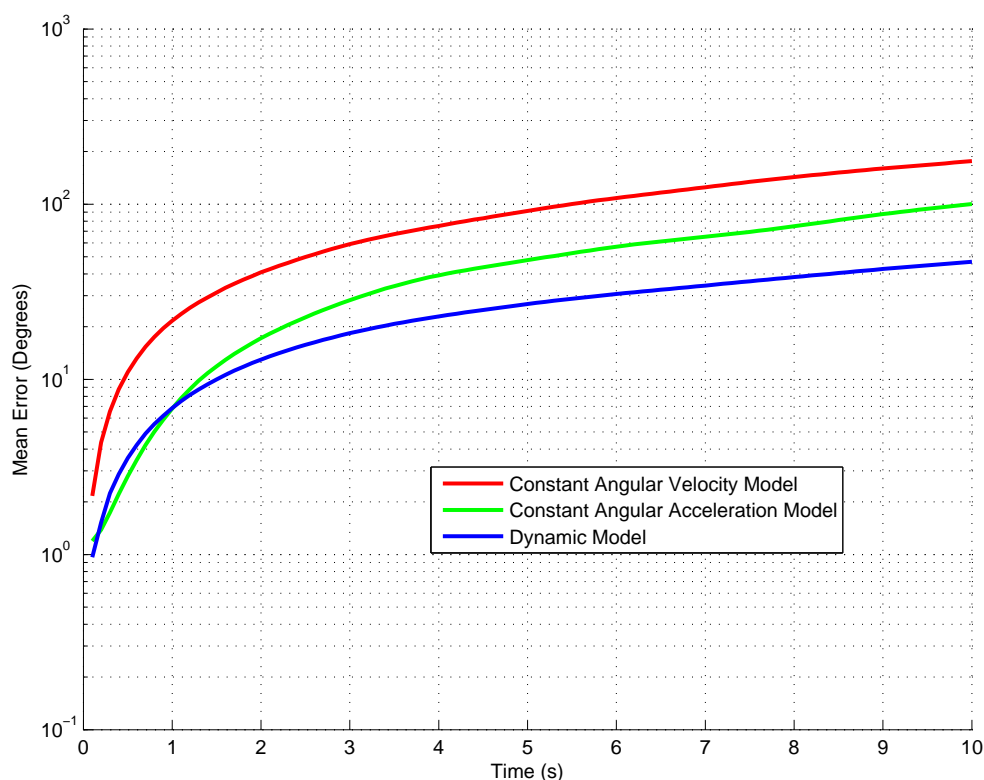


Figure 6.10: Relationship between model pitch output and IMU for integration times up to 10seconds.

In the body pitch axis the dynamic model is again better than the kinematic models for most integration periods. This is not true for very short integration periods where it is slightly outperformed by the constant rate kinematic model.

After 10 seconds the dynamic model has drifted from the IMU pitch prediction by an average of 47° compared to 100° and 176° for the constant rate and constant acceleration kinematic models. After a more typical signal outage of 2 seconds duration the models have drifted by 13° , 17° and 41° respectively.

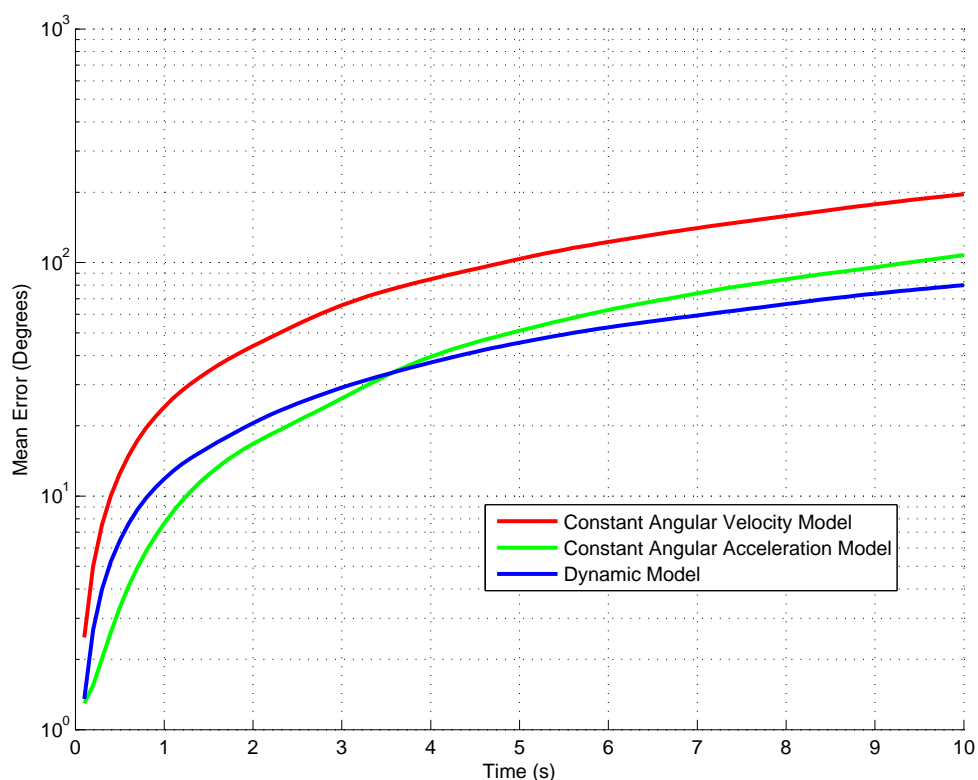


Figure 6.11: Relationship between model yaw output and IMU for integration times up to 10seconds.

In the body roll axis the dynamic model is again better than the constant acceleration kinematic model for all examined integration periods. The constant yaw rate kinematic model outperforms the dynamic model up to integration periods of 3.5 seconds.

After 10 seconds the dynamic model has drifted from the IMU yaw prediction by an average of 80° compared to 108° and 196° for the constant rate and constant acceleration kinematic models. After a more typical signal outage of 2 seconds duration the models have drifted by 21° , 17° and 43° respectively.

6.4.5 Special Cases

Large Rotation Rates

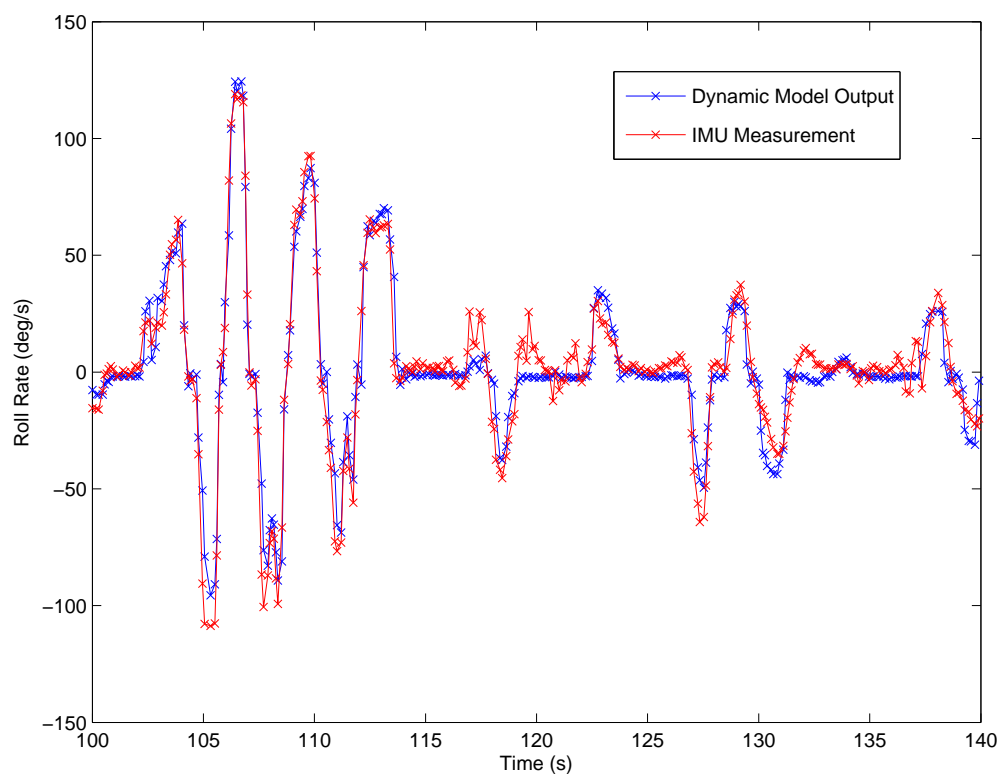


Figure 6.12: Measured and modelled roll rate during rapid turns.

The approximations used when deriving the dynamic model could be expected to cause a decrease in the model accuracy when large rotation rates occur. In the present research this has not been observed. The dynamic model and IMU roll outputs for the sequence of turns described in Section 6.4.2 are shown in Figure 6.12.

No significant decorrelation of model and IMU output is seen at the high rotation rates between 100 and 115 seconds when compared to the small turns later in the example.

Yaw Drift

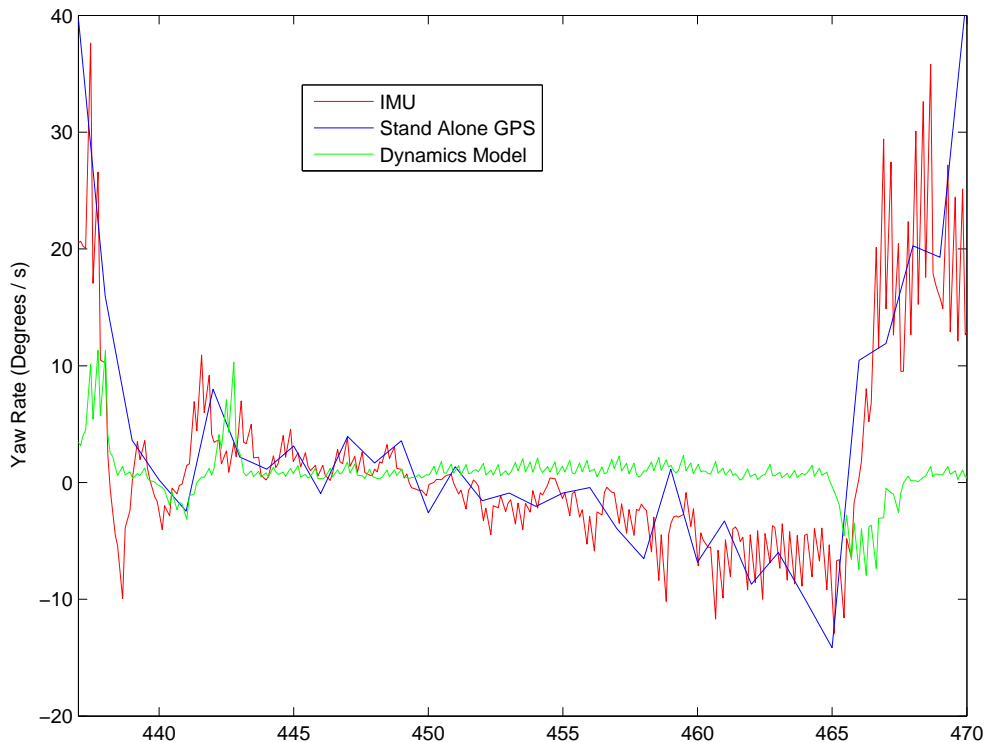


Figure 6.13: Measured and modelled yaw rates during level flight.

In Figure 6.13 the modelled and measured yaw rate during a period of level flight is shown.

A change in the yaw rate measured by the IMU can be seen between 445 and 465 seconds. This change is not due to a control input and is not modelled by the dynamic model which gives a nearly constant output.

For comparison the heading estimated from the position track at 1Hz is shown in blue. It indicates that the change in yaw rate measured by the IMU reflects reality and is not due to unexpectedly large drifts in the IMU output.

It is likely that this change in yaw rate is due to the wind acting to turn the UAV. In the same fashion as a ‘weather-vane’ the UAV will naturally tend to turn into wind. This is

not modelled by the dynamic model since it would require an estimate of the wind vector at the UAV flying altitude.

Since the UAV is being flown by a human pilot with a poor perspective from the ground, errors and drifts will inevitably appear between the intended and actual flight paths. This yaw drift is likely to have escaped the pilot's notice and remained uncorrected.

Control inputs from an autopilot would act to keep the yaw rate zero and keep the UAV on a constant heading. This control input would then appear as a yaw rate through the dynamic model. The dynamic model would therefore still not reflect the real yaw rate.

Low Airspeeds

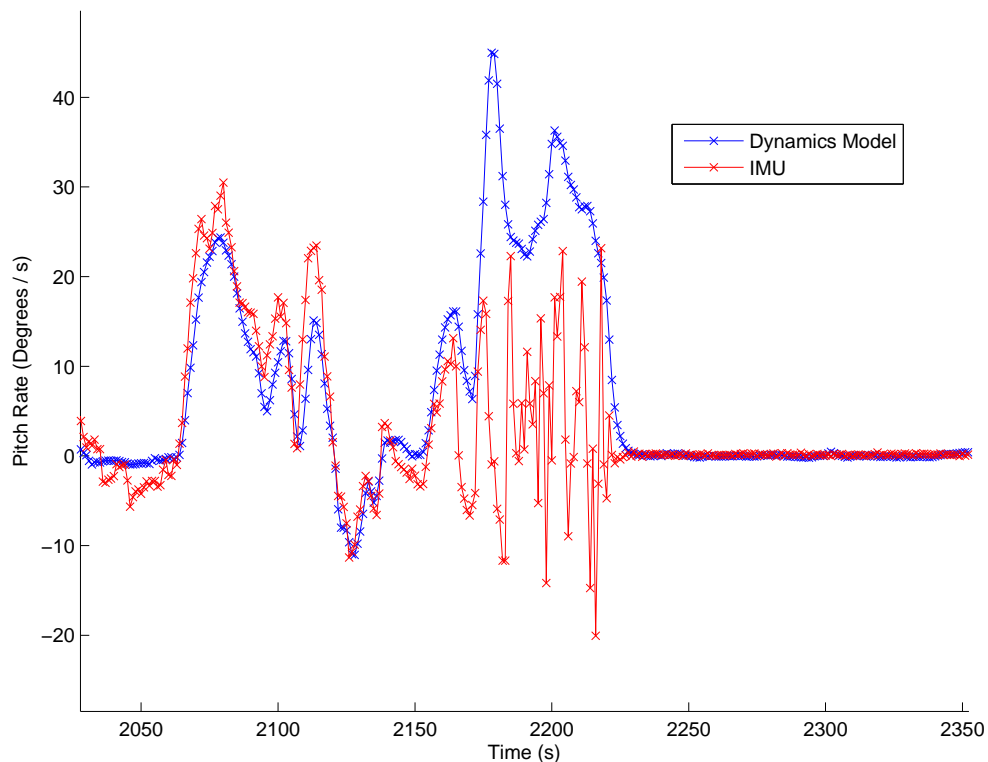


Figure 6.14: Measured and modelled pitch during landing.

Figure 6.14 shows the dynamic model output and measured pitch rate during landing. The UAV's airspeed is reduced throughout this example until touchdown at 2175 seconds.

After touchdown positive input is maintained on the elevators leading to large positive pitch rates being predicted by the dynamic model. Large accelerations and jerk produced by the touchdown itself and rolling over rough terrain produce large amounts of noise in the IMU gyro output. A similar sequence is seen at takeoff.

The dynamic model diverges from the measured pitch rate only when the velocity closely approaches the stall speed, just before landing. For a well setup and flown UAV this will not occur during the survey flight itself.

6.4.6 Discussion

As expected the performance of all types of model degrades over time. For a 1m baseline and 5Hz data rate the constant angular rate and dynamic models met the criteria for successful slip detection more than 95% of the time. This decreased to around 50% when the data rate was lowered to 1Hz. For reliable half cycle slip detection the receiver used should be chosen to have an appropriate output rate for the baseline length.

The constant angular acceleration model showed very poor performance in roll, pitch and yaw, even for short integration times. In part this reflects the rapidly changing dynamics of the mini-UAV.

The estimates of angular acceleration are also corrupted by noisy rate measurements from the IMU which is in a high vibration and acceleration environment. Filtering these measurements over more IMU samples would provide a better angular acceleration estimate but one which wouldn't reflect the rapidly changing angular accelerations.

Noise in the GNSS attitude measurements will result in the same problem but with the added problems of a lower data rate and the need to integrate twice over time as opposed

to once for the IMU measurements.

The constant rate model showed better performance because the rapid changes in angular acceleration produce a small net change in the angular rate.

Over longer integration times the dynamic model significantly outperformed the kinematic models. In pitch and roll the dynamic model matched the rate output by the IMU well, resulting in an attitude drift of around 10 degrees over the period of a typical signal outage compared to tens and even hundreds of degrees for the kinematic models.

All of the models showed poor performance when estimating yaw rate. In the case of the dynamic model this can be attributed to unmodelled torques resulting from the wind. The yaw rate and acceleration was rarely constant for this reason, explaining the poor performance of the kinematic models.

For longer integration times a better heading estimate might be obtained from the UAV velocity vector. This can be estimated through a separate positioning process, likely to be GNSS based. For example the platform velocity is available using a triple difference observable calculated between one of the UAV's onboard GNSS receivers and a stationary receiver on the ground. This approach would allow the half cycle ambiguous carrier phase data to be used.

The platform velocity will give the true heading in a trimmed, straight flight mode with no wind acting on the UAV. In all other cases it will be in error.

The results presented here assume that a GNSS signal outage can happen at any time in the flight. It has been seen that this is more likely to occur at times when the UAV is undergoing large rotational accelerations.

To keep well within visual range the UAV in this dataset was rarely truly straight and level. These results therefore closely reflect the portions of a survey flight in which the UAV is turning rather than the idealised long straight survey lines.

The turns performed in the present flight were also inconsistent due to human pilot error. A UAV which is piloted by an autopilot and able to go beyond visual range of the pilot would allow a more repeatable flight path to be flown with accurate turns. This in turn would allow better analysis of the model performance in the various flight modes and for various rotation rates.

A UAV capable of longer flights would also necessarily have a larger fuel tank and the change in the inertia matrix over the course of the flight would therefore be greater. The change in the K70s inertia matrix due to fuel usage is insignificantly small and the effects were not observed in this flight test.

6.5 Half Cycle Ambiguity Resolution

Finally the resolution of half cycle ambiguities is tested with the data obtained using the GNSS hardware simulator.

6.5.1 Forwards Processing

The aim of this section is to examine the success rate of half cycle ambiguity resolution using float ambiguities adjusted using the dynamic model output after a short signal outage.

When processing forwards in time the half cycle ambiguity resolution process will follow a GNSS signal outage. The estimated attitude will therefore be from a kinematic or dynamic model. Since the dynamic model has been shown to give the most accurate and precise estimates it will be used in this section.

Method

In Section 6.4 the drift of the attitudes estimated by the dynamic model were investigated. After a 2 second integration time the mean drift was found to be 8° , 13° , 21° in roll, pitch and yaw. The dynamic model roll, pitch and yaw estimates also had standard deviations of 11.4° , 17.2° and 28.3° .

To investigate the probability of success at each GNSS measurement epoch, a set of 1000 baselines was generated. The set was generated from a normal distribution of attitudes with mean and standard deviation from the model test results. The number of baselines which lead to ambiguities being correctly resolved was then used to determine a success rate at each measurement epoch.

To allow simple recovery of ambiguities, the static, short baseline data from the GNSS hardware simulator was used.

For each of the generated baselines an attempt was made to resolve ambiguities to half integers using the bootstrap with Z transform and LAMBDA methods. With this dataset these techniques gave success rates of better than 95% for whole integer ambiguity resolution using the code based, constrained, float solution (Chapter 4).

Result

In Table 6.9 the mean success rate over 3000 measurement epochs is given for two baseline orientations and the two ambiguity resolution methods.

Table 6.9: Half Cycle Ambiguity Resolution Using the Dynamic Model

Ambiguity Fixing Method	Yaw / Roll Success %	Yaw / Pitch Success %
Bootstrap with Z transform	22.2	18.3
LAMBDA	25.1	21.4

6.5.2 Backwards Processing

The aim of this section is to examine the success rate of half cycle ambiguity resolution using float ambiguities estimated using the triple difference observable.

When processing backwards in time, the half cycle ambiguity resolution process will follow an ambiguity fixed epoch, working backwards towards a signal outage. The estimated attitude will therefore be of high precision, coming from an ambiguity fixed solution and a triple difference attitude rate solution over one epoch.

Method

For this section the UAV flight simulated on the GNSS hardware simulator was used. The zero baseline data was chosen in particular to allow simple recovery of the half integer and integer ambiguities.

At each GNSS measurement epoch a baseline estimate was obtained using the fixed solution from the subsequent epoch and a change in attitude estimated using the triple difference observable. The ambiguities were adjusted using this baseline and half integer ambiguity resolution attempted.

Results

In table 6.10 the success rate of half integer ambiguity resolution is given. The integer ambiguity estimators used in Section 6.5.1 are employed for the same reasons.

Where full cycle ambiguous measurements were available they were resolved to half cycles for direct comparison with the half cycle data success rates.

The sample size used to determine the success rate for half cycle ambiguous measurements is smaller than that used to determine the success rate for full cycle ambiguous

measurements. Of the 3000 measurements processed, around 2000 were full cycle ambiguous and 1000 were half cycle ambiguous.

Table 6.10: Half Cycle Ambiguity Resolution Using the Triple Difference

Ambiguity Estimation Method	Full Cycle Ambiguous Meas.	Half Cycle Ambiguous Meas.
Bootstrap with Z transform	99.6%	91.8%
LAMBDA	99.6%	91.8%

6.5.3 Discussion

These results show that half integer ambiguity resolution using the dynamic model output after a signal outage is unreliable, having a low success rate. In contrast using the triple difference observable to estimate attitude yields a high probability of success. Working backwards after full cycle measurements are regained is therefore preferable where the latency introduced is acceptable.

The ambiguity estimators used in this section both yield very high success rates (99.6% and 91.8%) when the triple difference observable is employed. The lower success rate when using half cycle ambiguous data reflects the lower precision of these measurements.

These success rates could be further improved by using a modified version of the constrained LAMBDA method. However this would introduce an unacceptably large number of candidates to be searched and lead to an unacceptably large computational overhead.

Small improvements may be gained by identifying double difference measurements which remain integer cycle ambiguous throughout signal tracking problems. In the present data very few integer ambiguous double difference measurements were found to be available after tracking problems and the improvement would therefore be negligible.

6.6 Conclusion

In this chapter data has been used to show that the carrier phase triple difference observable can be used to estimate the angular velocity of a GNSS attitude system. The velocity estimates obtained using half cycle ambiguous carrier phase data are no less precise than those obtained using carrier phase data which has been resolved to full cycle by the receiver.

Integration of this angular velocity estimate with respect to time results in an attitude estimate which is more precise than the code dominated 'float' solution but suffers from biases which accumulate over time in addition to any bias in the initial attitude estimate. Data collected using low cost GPS receivers and antennas has shown that the accumulated biases are insignificant when the triple difference is used for short periods (<30s).

The noise level of the carrier phase triple difference carrier phase observations is low enough to allow reliable identification of half cycle slips. Using low cost receivers and a hardware GNSS simulator the noise level of the geometry free triple difference observables in a moving baseline test was found to be 0.015 cycles (standard deviation).

The effect of error in the estimated triple difference geometry on the ability to resolve cycle slips has been shown to depend on the angle between the error vector and the double difference observation vector. For GNSS attitude determination the length and direction of the error vector is constrained by the baseline length and depends only on error in the predicted attitude.

In the worst case the error vector and the double difference observation vector are parallel. Using this knowledge, the maximum allowable error in the estimated attitude can be derived. For a baseline length of 1m the error in the predicted attitude must be less than 5.3° to resolve half cycle slips.

Next the models used to predict the change in attitude over time were examined. Us-

ing data from an Inertial Measurement Unit on a real mini-UAV flight the accuracy and precision of the kinematic models and dynamic model were derived. Their ability to aid cycle slip detection and bridge GNSS signal outages was then analysed.

In all rotation axes the constant acceleration model was found to have poor performance due to unavoidable noise in the attitude rate measurements.

The constant angular rate kinematic model showed better performance, especially over short periods. It was seen to be suitable for cycle slip detection in the 1m baseline case when the GNSS data rate was 5Hz or above.

For longer integration periods the dynamic model showed superior performance to both the kinematic models. It was particularly effective in the pitch and roll axes where its mean deviation from the IMU predicted attitude was less than 13° over a typical GNSS signal outage.

In the yaw axis unmodelled torques due to the wind meant that the dynamics model failed to accurately match the true rotation rates, drifting by a mean of 21° over two seconds. In the yaw axes the constant rate model actually outperformed the dynamics model for short integration times, up to 3.5 seconds. A better estimate of the platforms heading after a signal outage may be obtained using the velocity vector derived from the platform positioning process, particularly in low wind conditions.

Finally the success rate of half integer ambiguity resolution was examined. As might be expected, the success rate of half integer ambiguity resolution was higher when using the triple difference estimates (based on carrier phase data) than when using the dynamic model. Working backwards after full cycle measurements are regained is therefore preferable where the latency introduced (up to 10 seconds) is acceptable.

The data analysed in this chapter has proven the ability of the developed algorithms to utilise half cycle ambiguous carrier phase data, detect and correct cycle slips and provide a graceful degradation of the attitude solution during signal outages without adding

hardware, cost or weight to the UAV.

Chapter 7

Conclusions & Future Work

7.1 Conclusion

In Chapter 1 the problem to be investigated was introduced. Small Unmanned Aerial Vehicles (UAVs) offer a very low cost means of flying miniaturised sensors for geospatial data capture. These sensors (for example cameras and laser distance meters) can in turn provide high accuracy, high resolution geospatial products.

To obtain a useful product from these remote sensing systems their data must be aligned with a global or regional reference system, 'georeferenced'. To achieve this without the use of an extensive ground survey, high accuracy knowledge of the sensor trajectory is required. The sensors position can be estimated using established Global Positioning Satellite System (GNSS) techniques. Estimating the sensor attitude is an open problem.

The traditional inertial methods used on larger aircraft fail on the mini-UAV. Cost, weight, size and performance requirements make the inertial sensors impractical and their output is easily corrupted by the vibration and jerk inherent in mini-UAV operation.

The purpose of this research is to identify, test and develop an alternative to inertial techniques.

The GNSS attitude method is identified as a potential alternative. The equipment required

is low cost, low mass and small. Indeed one GNSS receiver and antenna will already be in the UAV payload for use in positioning, re-utilising its output increases the efficiency of the payload.

The performance and reliability which can be achieved using modern low cost GNSS equipment and the inter-antenna distances available on a mini-UAV is unclear from the literature. The first task therefore was to implement and test the state of the art algorithms with suitable equipment.

In chapters 2 and 3 state of the art GNSS attitude techniques were introduced. The algorithms were implemented using MATLAB and tested using measurements from a typical low cost GPS receiver. In Chapter 4 the results of this testing were presented.

The accuracy and precision of the attitude estimates depend on the inter-antenna baseline length as well as the equipment used and processing strategy. In this research a 1m baseline length with low cost antennas and single frequency GPS receivers yielded a heading precision of 0.3 degrees. The precision of the pitch or roll estimates was found to be 1.3 degrees, worse than the heading due to the satellite - receiver geometry.

It is impossible to put an absolute value on the maximum allowable attitude error for georeferencing. It depends on the flying height, system design and survey data requirements. The relationship between attitude error and georeferencing error is discussed in Appendix B. The figures obtained in this work over a 1m baseline are adequate for a UAV flying with typical sensors at 400ft (120m) above ground level.

During static tests it was found that using the constrained LAMBDA method, an integer ambiguity fixed attitude estimate was available at every measurement epoch in the absence of multipath.

The disadvantage of the constrained LAMBDA method is its requirement for large numbers of integer ambiguity candidates to be examined, making the process slow and computationally expensive. Excellent success rates (93.4% and 96.3%) were also achieved

using the bootstrap with Z-transform and ordinary LAMBDA methods when the float input was constrained using *a priori* baseline length information. These methods are very computationally efficient and so make a better choice for use with low cost hardware in real time or low latency applications.

Testing of the integer ambiguity validation methods revealed that the traditional ratio test was ineffective when used with constrained float inputs and the constrained LAMBDA estimator. The validation technique developed by the author showed excellent performance, especially for the bootstrap and LAMBDA method. When used with the constrained LAMBDA method a significant number of candidates were accepted when they were in fact false (5.6%). For this reason, as well as computation simplicity, the bootstrap and LAMBDA method with constrained float input offer the best choice for a combination of reliability and success rate.

This is the first work to test and compare the integer bootstrap, LAMBDA and constrained LAMBDA techniques for GNSS attitude determination using low cost equipment and 'real world' static data.

GPS data from a mini-UAV platform showed variations in the quality of the GPS measurements over the course of the flight. Numerous 'loss of lock' indicators were observed, the number of carrier phase measurements available varied rapidly and for portions of the flight only half cycle ambiguous carrier phase measurements were available.

A GNSS hardware simulator was used to generate a trajectory which replicated these problems. Banked turns at rates typical of mini-UAV flight caused the GPS receiver to lose lock on the code and carrier phase signals. After loss of lock the carrier phase output was only resolved to half integers until full code tracking resumed. A period of around 10 seconds stable flight was required to fully regain tracking. This is the first work in which problems caused by real mini-UAV flight have been identified and reproduced.

To overcome these measurement outages and make use of the half cycle ambiguous car-

rier phase data three algorithms were developed in Chapter 5.

- The first algorithm uses mathematical modelling to estimate the UAV rotation rate during signal outages. This novel method allows an estimate of the UAV attitude over time to be made almost entirely in software, incurring little extra cost or weight.

Three potentially suitable models are introduced - two kinematic models which use a history of the UAV rotation to make predictions and one dynamic model. The dynamic model uses an aerodynamic model to estimate the torques acting to rotate the UAV. These torques are converted to rotational accelerations through application of Newton's second law.

An innovative set of assumptions are made to sacrifice aerodynamic model fidelity for the ability to use the model without extra airspeed sensors on the UAV and with simple estimation of the model coefficients.

- The second algorithm uses the output from the attitude models to identify and correct cycle slips in the GPS carrier phase measurements. This is the first time this has been done using a GNSS attitude system and attitude models.

By correcting the GNSS triple difference carrier phase observation with the change in attitude predicted by a model, cycle slips above a threshold can be identified and corrected. A more accurate model allows a lower threshold. Slips as small as one half cycle need to be identified to make use of the GNSS triple difference observable in algorithm three.

- Algorithm three uses the (cycle slip corrected) GNSS triple difference observable to estimate the UAV rotation rate. With an initial attitude estimate this can be used to estimate the UAV attitude over time. The triple difference observable can be used with full or half cycle ambiguous measurements and so is capable of making use of the half cycle ambiguous data observed in this work.

The use of the triple difference observable to estimate rotation rate with full and half cycle ambiguous measurements is another innovation in this research.

The UAV attitude estimated using the carrier phase triple difference observable is more precise than that available from the GPS code based ‘float’ estimate. Its accuracy depends largely on the accuracy of the initial attitude estimate from an ambiguity fixed GNSS attitude solution or the prediction from a model. If the initial attitude estimate is sufficiently accurate the triple difference based attitude estimate will provide a good starting point for integer, or even half integer ambiguity resolution.

When used in combination the algorithms developed in this thesis;

- Make an attitude estimate available even when no GNSS signals are being tracked.
- Identify and correct cycle slips down to the half cycle level.
- Give an accurate and precise attitude estimate using half cycle ambiguous carrier phase measurements.

Being able to make use of half cycle ambiguous data for georeferencing greatly increases the efficiency of a survey. For example to obtain aerial photography of a 1km^2 area from a mini-UAV, 20 lines must be flown. If each turn causes a loss of signal tracking followed by 10 seconds of half cycle ambiguous data, around 4km will be flown at 20ms^{-1} with half cycle ambiguous tracking. The ability to use that half cycle ambiguous data means that the 4km of flying will be usable saving 17% of the flight time & cost.

In Chapter 6 the algorithms were tested, again with GNSS measurements from low cost GPS equipment and real flight data.

To examine the drift of the kinematic and dynamic models measurements from an Inertial Measurement Unit (IMU) onboard a mini-UAV were obtained. A comparison of

the IMU output with that from the models shows that the dynamics model significantly outperforms the simpler kinematic models in the pitch and roll axis. The dynamic model drifted from the IMU by a mean of 4 degrees per second in roll and 6 degrees per second in pitch. This compares favourably to 21 degrees per second in roll and 7.5 degrees per second in pitch for the best kinematic model.

In the yaw axis, unmodelled torques due to the wind increase the drift of the dynamic model. This reduces its performance to match that of the constant angular rate kinematic model.

Drift in the dynamic model output makes it unsuitable for use in georeferencing. However the success rate of half integer ambiguity estimation after using the model for 2 seconds (the duration of a typical signal outage) was around 50% using the bootstrap or LAMBDA methods. Half cycle ambiguity resolution has a success rate approaching zero when using the code pseudorange GPS observation soon after a signal outage and so use of the model gives significant benefits in real time applications.

Both the dynamics model and constant angular rate kinematic model were found to be capable of reliable half cycle ambiguity resolution with the triple difference observable if the output rate of the GNSS receiver is high (at least 5Hz). A lower output rate increases the drift in the models between measurements and therefore increases the threshold of cycle slips which can be detected.

The carrier phase triple difference observable yielded an attitude estimate with negligible drift over periods of less than 30 seconds. It gave an attitude rate estimate with a precision of 1 degree per second over a 1m baseline under 'real world' conditions. While this is not precise enough for georeferencing, even over short periods, it does give good full and half cycle ambiguity resolution results.

A final test was carried out using the cycle slip corrected triple difference observation to estimate the change in attitude from an ambiguity fixed solution at an adjacent epoch.

This gave half cycle ambiguity resolution success rates of 91.8% when using half cycle ambiguous data and 99.6% success rates when using full cycle ambiguous data. As a result, for low latency applications the half cycle ambiguous carrier phase measurements can be used to provide an attitude solution suitable for use in georeferencing by using the triple difference observation to ‘work backwards’ from an ambiguity fixed measurement epoch.

In Chapter 1 the overall aim of this research was stated as “to develop methods which will provide a robust attitude solution using low cost GNSS attitude hardware onboard a mini-UAV”.

Using the algorithms developed in this work low cost GPS hardware can be used to provide an accurate, precise, drift free estimate of the mini-UAV attitude. The solution is robust to real world problems including complete signal outages caused by rapid changes in trajectory. As a result of this work substandard GNSS observations can be used to give an attitude solution suitable for continued georeferencing. The aim has therefore been met.

This work has enabled practical use of GNSS attitude determination on the mini-UAV. This in turn will significantly contribute to the mini-UAV becoming a commonplace survey tool.

7.2 Future Work

This thesis has identified GNSS attitude determination as a suitable technique for use on the mini-UAV. Through testing with commercially available low cost equipment it has identified problems with GNSS signal tracking onboard the mini-UAV and has developed methods to overcome this. There is a great interest in both civilian mini-UAVs and GNSS attitude determination at present. To continue this research and make further advancements in these fields recommendations are made here for future work.

Most importantly the algorithms developed in this work should be tested with a full GNSS attitude system on a real mini-UAV survey flight. In this work legal and technical constraints meant that the mini-UAV test flights needed to be flown within visual range of a human pilot directly controlling the UAV. In consequence this meant that the flights featured many turns, short periods of straight flight and a very imprecise trajectory. When the GNSS receiver showed difficulties in tracking the GNSS signals it rarely had time to fully recover. Use of a UAV with autopilot and extended range would allow examination of the kinematic and dynamic models through specific flight phases and allow the receiver to fully recover from signal outages. This in turn would allow crucial testing of the full GNSS attitude system on a real mini-UAV.

In chapter 4 multipath was identified as an error source which will reduce the success rate of integer ambiguity resolution and reduce the precision of the attitude estimates. In static tests at 1m above ground level reflection of the GPS signals from the ground caused the success rate of integer ambiguity resolution to drop to 86% from 100%. Low cost hardware, and in particular antennas, do little to mitigate multipath and traditional antenna groundplane solutions are not suitable for mini-UAV use. Work is required to quantify the effect of multipath on a UAV at various flying heights. In this work multipath from ground reflections was observed at 1m above ground level. This effect will change with distance from the primary reflector (the ground) and may be reduced or even eliminated by increasing the flying height.

In recent research more efficient integer ambiguity resolution methods have been developed, for example (*Giorgi et al.*, 2008), (*Giorgi*, 2010) and (*Giorgi and Teunissen*, 2010). While these methods reduce the computational burden they are not capable of using half cycle ambiguous measurements and rely solely on the code based float solution. Further work is required to adapt these, and the constrained LAMBDA approach used in this work, for half integer ambiguity resolution. If this were to be done, the success rate of half integer ambiguity resolution could be further improved without adding an unacceptable computational burden.

The aerodynamic model developed in this work was seen to give poor heading performance in the presence of unmodelled wind. Future work could focus on improving the fidelity of this model, perhaps including a wind vector estimated from the UAV trajectory. Alternatively the aiding of the heading output with the measured UAV trajectory could be investigated.

Eventual integration and testing of the complete GNSS attitude, positioning, remote sensing and mini-UAV system will fulfill the goal of this research. At this point a commercially viable system will be created, enabled in part by the GNSS attitude research in this thesis.

Appendices

Appendix A

Civilian UAV Operations & The K70 System

A.1 Civilian Regulation of Unmanned Aerial Systems

The purpose of this section is to give a brief overview of the regulatory context in which this UAV based research was undertaken. The regulation of unmanned aircraft is rapidly evolving as technology develops and civilian market pressures increase.

Regulation of civil aircraft (including unmanned aircraft) in national airspace is usually delegated to a government agency. In New Zealand it is undertaken by the Civil Aviation Authority of New Zealand. Each national body has developed its own rules for unmanned aircraft certification and operation. International & regional regulation is currently concerned with larger unmanned systems which are not of concern to this work.

Common to most civilian regulatory environments is the philosophy that unmanned systems should 'do no harm'. It is generally accepted that unmanned aircraft should pose no greater risk to a third party than a manned aircraft of similar size.

At present the major technological barrier to unmanned aircraft operation alongside manned aircraft is reliable 'sense and avoid' technology. Until the unmanned aircraft can detect and avoid other airspace users as reliably and effectively as manned aircraft they will not be permitted to operate in unrestricted airspace.

In New Zealand strict limits are placed on the operation of unmanned aerial vehicles. Until autonomous 'sense and avoid' technology matures, an unmanned aerial vehicle cannot operate beyond the visual range of its human controller or above 400ft (120m) above ground level. If these limits are to be violated segregated airspace is required to separate manned and unmanned aircraft. It is costly and time consuming to arrange this airspace and so operations beyond these limits are not practically possible for a small system developer.

A.1.1 Certification

The terms Unmanned Aircraft System (UAS) and Unmanned Aerial Vehicle (UAV) are sometimes used interchangeably. In this work the former is defined as the entire hardware system including the aircraft, ground control station and ground to air communications. The UAV is the airborne component of the UAS.

Most regulatory frameworks separate the concepts of UAV and UAS. They recognise that for safe operation all components of the UAS must have equally high integrity and standards of operation. For this reason unmanned systems are usually certified to operate as a whole.

Unmanned pilot certification is a developing field. Unmanned aerial systems vary greatly from type to type. Some simple systems have a single human pilot who directly controls the UAV and operates the payload. More complex systems may have multiple crew and payload operators. In some systems takeoff and landing (launch and recovery) is undertaken by one team while the majority of the flight is undertaken by another team who may be on another continent to the unmanned aircraft.

In New Zealand no pilot certification is currently required for operators of unmanned aircraft which weigh less than 15kg.

A.2 The K70 System

The K70 is a small bespoke UAV developed by the Geospatial Research Centre (NZ) Ltd for preliminary research into the use of UAVs for aerial surveying.

It is designed to carry a payload of up to 1.5kg and have a net weight of less than 5kg. It is intended for research concerning survey payloads, control systems and navigation systems.

All of the UAV components are modular including the payload, control system, engine and wings. This allows the straightforward integration and testing of payloads in a laboratory environment before they are flown. It also allows the system to be tested with a variety of engine types (petrol, electric, etc) and control systems.

The low mass of the K70 means that it can legally be flown in the fashion of a remote control model aircraft. It is flown by a pilot experienced in model flying but without needing formal certification. The K70 UAS therefore consists of the UAV, a controller for the pilot and a communications link from controller to UAV.

When flown for this research, the K70 was operated without an autopilot or automated stability system. These systems are still under development and the financial risk was too great to operate them alongside a relatively expensive survey payload.

The K70 payload is described further in Appendix B. Its primary purpose is to allow the examination of the survey images available from low mass cameras operating at visible and thermal wavelengths.

Appendix B

Aerial Survey Using UAVs

This appendix gives a brief overview of generalised mini-UAV survey payload components. The specific payload components used on the K70 mini-UAV are also described

The process of georeferencing is examined in more detail and the navigation accuracy requirements are considered.

B.1 Payload Design

All UAV survey payloads have a set of elements in common. Besides the survey sensors and navigation sensors, subsystems are required to power the hardware and handle the data produced.

The integration of payload elements with the UAV power and control system varies with each UAV design. In the K70 UAV used for this work the payload and UAV systems were separated, besides a data link to log the control inputs.

A generalised UAV payload architecture is depicted in Figure B.1.

In some systems the datalogging element is removed and the data is transmitted direct to the ground for storage or processing. This has been avoided in the design of the K70 payload to eliminate loss of data in transmission.

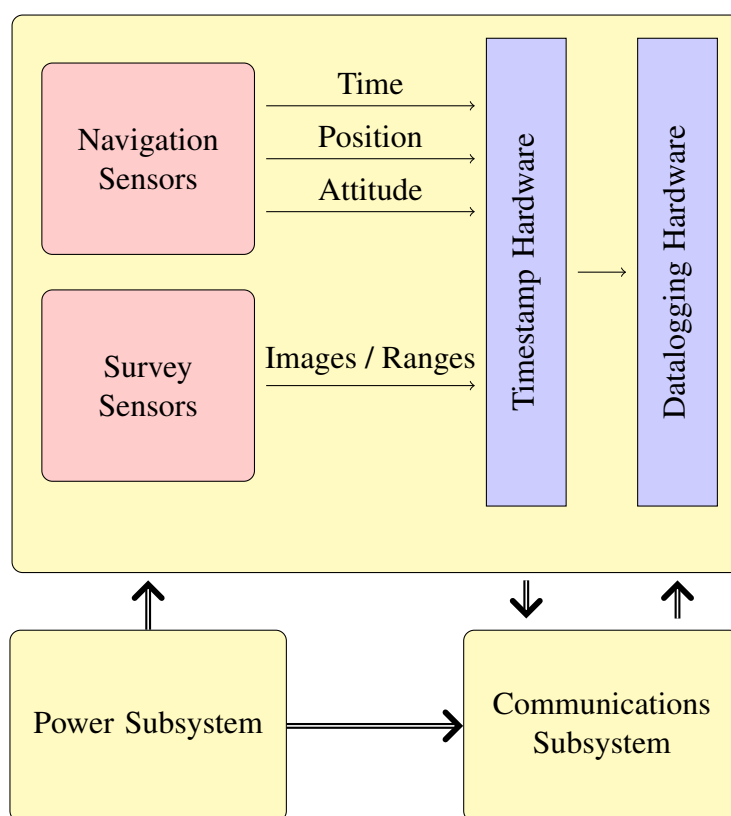


Figure B.1: Generalised Survey Payload Components

In other payload designs, particularly those intended for real time operations, a computational element must be included. Raw navigation and remote sensing data is processed onboard and the survey product is logged or transmitted to the ground. The power subsystem generally consists of a power source and regulation equipment. The power may be obtained from batteries, solar cells, or generated using the UAV motor. The power subsystem will also contain a monitoring element to provide warnings when insufficient power is being generated or remains in the batteries.

The communications subsystem allows the human operator an interface with the payload. Commands may be issued from the ground to operate the payload while monitoring information and raw or processed survey data is relayed to the operator. Communications are expensive and can be unreliable, particularly over long distances and where large

bandwidths are required to send imagery or other survey data. For this work all data was post processed and so the communications requirement was minimal and not critical.

B.1.1 The K70 Payload

The payload flow for this work is shown in Figure B.2. For the dynamics modelling research, a data stream containing the control inputs was also timestamped and logged.

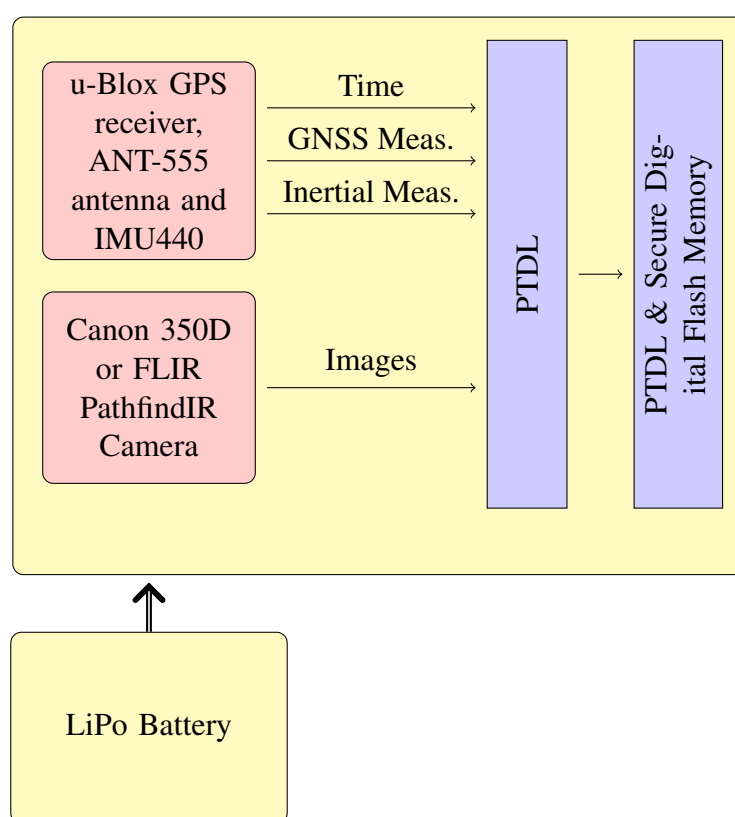


Figure B.2: K70 Survey Payload Components, the PTDL is bespoke logging hardware designed by the Geospatial Research Centre (NZ) Ltd, it is described further in the text.

The Precise Time Data Logger ‘PTDL’ is bespoke hardware designed to timestamp and log data inputs. It uses the precise 1 pulse per second output of the uBlox GPS receiver to steer its internal clock to GPS time. Time stamp markers are then added to specified

bytes of an RS232 data stream or to the leading edge or trailing edge of pulse inputs. The ability to timestamp pulses means the PTDL can be used to timestamp frames of video data or synchronisation pulses from other sensors.

The integrated K70 payload has also been tested onboard manned light aircraft to allow data from high altitudes and large areas to be collected.

B.2 Georeferencing

Georeferencing aerial survey data has been the subject of research for many years. A complete review is not given here, instead the reader is directed to work such as *Kasser and Egels (2002)* or *Mostafa and Schwarz (2001)*.

Of particular concern to this work is a technique known as ‘direct georeferencing’. Whereas traditional georeferencing of imagery requires extensive ground survey of features identifiable in images, pure direct georeferencing only uses the position and orientation of the sensor at the time of image exposure. As a result, access to the areas being surveyed is not required and an expensive ground survey campaign is not required.

Direct georeferencing is the only option for ranging sensors such as a laser scanner or nadir pointing laser distance meter.

B.2.1 Imagery

An image sensor can be thought of as an array of sensors (pixels) which measure the intensity of a part of the light spectrum. Light reflected from a point on the ground will travel through a lens, through a focal point and onto a pixel. The resulting image will be distorted by the lens, ground height variation and the sensor orientation.

The lens distortions are removed through calibration and the ground height variations

through the use of *a priori* information or through the use of stereo images. Removing the distortions due to sensor rotation is the purpose of the attitude determination in this work.

To examine the effect of a rotation error on the direct georeferencing process an imaginary scenario is created in which the image suffers from no lens distortion, the ground is level and the position of the focal point is precisely known.

This is depicted in Figure B.3.

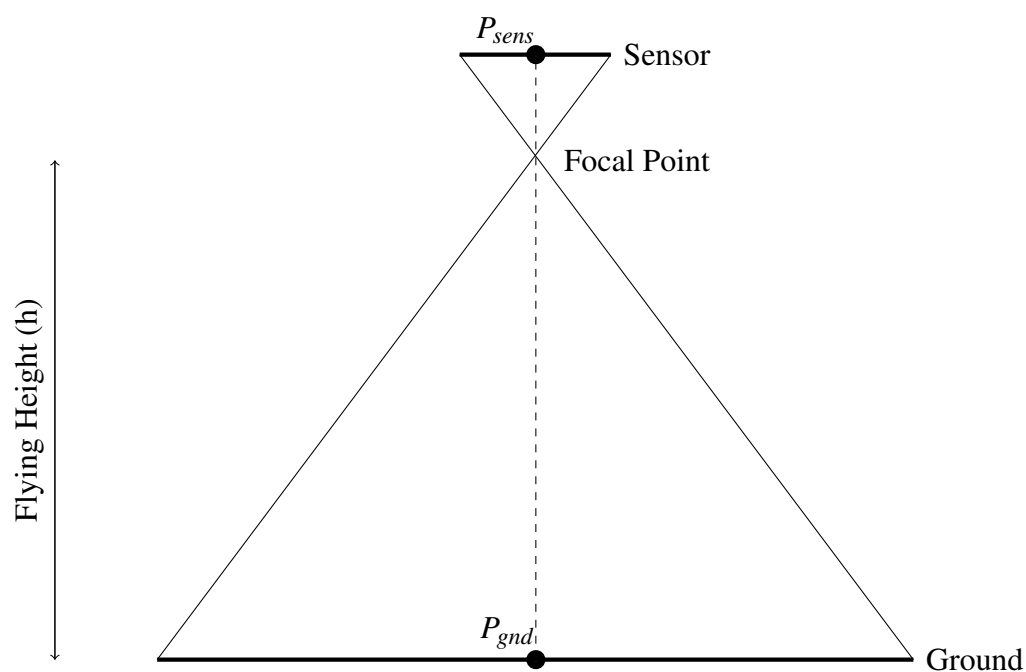


Figure B.3: Level imaging sensor with lens and ground distortions removed.

In Figure B.4 the effect of an attitude error in pitch or roll is depicted. The small attitude error $\Delta\theta$ results in an error ΔP_{gnd}^{pr} on the ground.

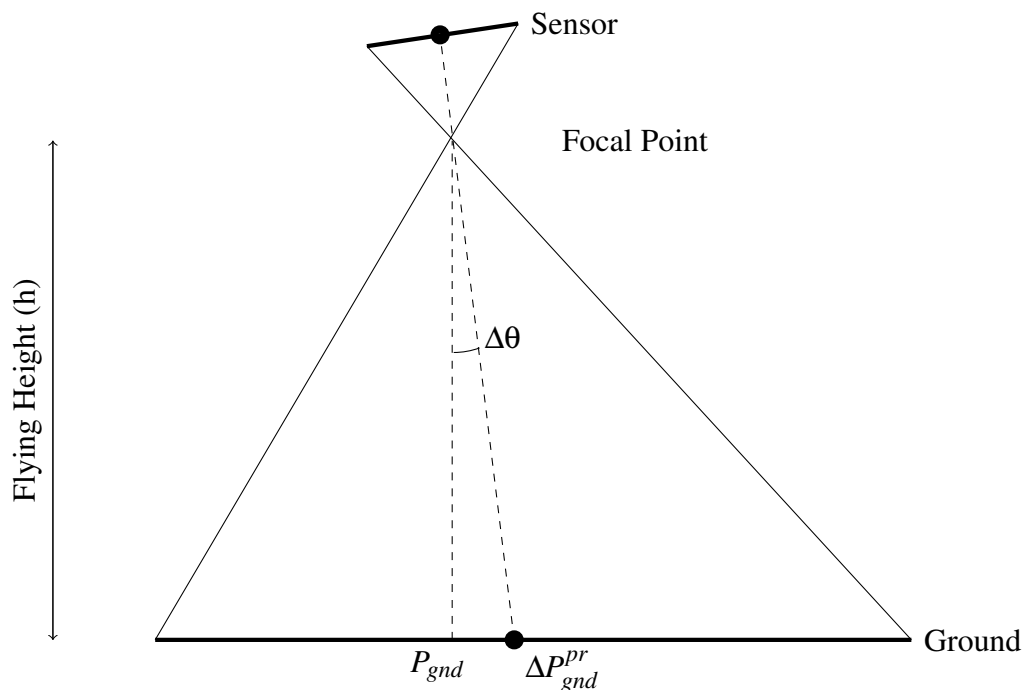


Figure B.4: Error in georeferencing due to an attitude error in pitch or roll ($\Delta\theta$).

It can be seen from Figure B.4 that the distance ΔP_{gnd}^{pr} , the georeferencing error, is a function of the flying height (h) and the attitude error ($\Delta\theta$).

For small $\Delta\theta$ and for a point P_{gnd} near the point directly below the sensor we can say;

$$\Delta P_{gnd}^{pr} = h \tan(\Delta\theta) \quad (\text{B.1})$$

More generally, for sensors which are not level and pixels which are not in the centre of the sensor we have;

$$\Delta P_{gnd}^{pr} = h \tan(\psi + \Delta\theta) - h \tan(\psi) \quad (\text{B.2})$$

Where ψ is the angle between a line from the focal point to a point directly below the sensor and the line joining the focal point and P_{gnd} . The angle ψ will depend on the sensor attitude and the pixel location on the imaging sensor.

Figure B.5 depicts the variation in the magnitude of georeferencing error over an image for a given pitch or roll error.

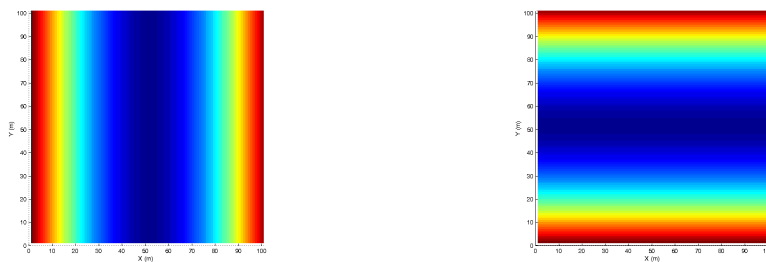


Figure B.5: *The variation of georeferencing error over an image for roll error (left) and pitch error (right). Warm colours indicate a larger error (towards the outside of the image).*

The effect of an error in heading is more complex to determine. If pitch and roll errors are zero then it depends on the distance (d) of point P_{gnd} from a point directly below the camera. The point directly below the sensor will not be affected by heading error.

As the heading angle changes the point P_{gnd} will describe a circle around the point directly below the sensor. A heading error will cause a georeferencing error ΔP_{gnd}^h which is equal to the chord length between the point P_{gnd} and the rotated point.

$$\Delta P_{gnd}^h = 2d \sin\left(\frac{1}{2}\Delta\theta\right) \quad (\text{B.3})$$

Figure B.6 depicts the variation in the magnitude of georeferencing error over an image for a given heading error.

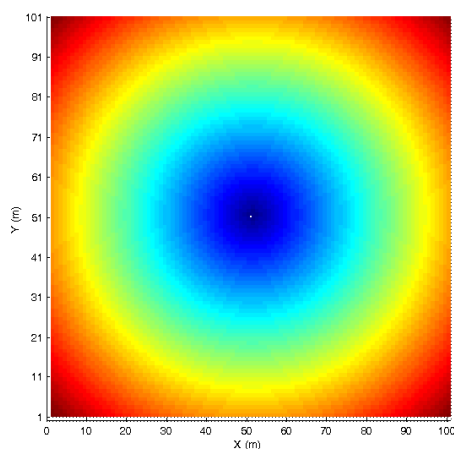


Figure B.6: The variation of georeferencing error over an image for heading error. Warm colours indicate a larger error (towards the outside of the image).

B.2.2 Ranging Measurements

A ranging measurement, such as that from a nadir pointing laser distance meter, can be thought of as a measurement from one pixel of an imaging array. The error equations for the imaging sensor therefore apply equally to the ranging sensor.

B.2.3 Attitude Error Limits

The attitude error acceptable will be determined by the surveyor and system in use. It requires knowledge of the flying height, imaging sensor dimensions and overall georeferencing error budget.

The requirements can be relaxed by flying at a lower altitude, which also has the benefit of increasing the image ground resolution or reducing atmospheric effects on a laser signal. This is done at the expense of requiring more images to cover a given area. The attitude determination requirement can also be relaxed if the sensor is kept near level and

a smaller imaging sensor (or longer focal length) is used.

To give some representative values, Figure B.7 shows the results of using Equation B.1 to calculate the effect of a pitch attitude error at the centre of an image for a variety of flying heights.

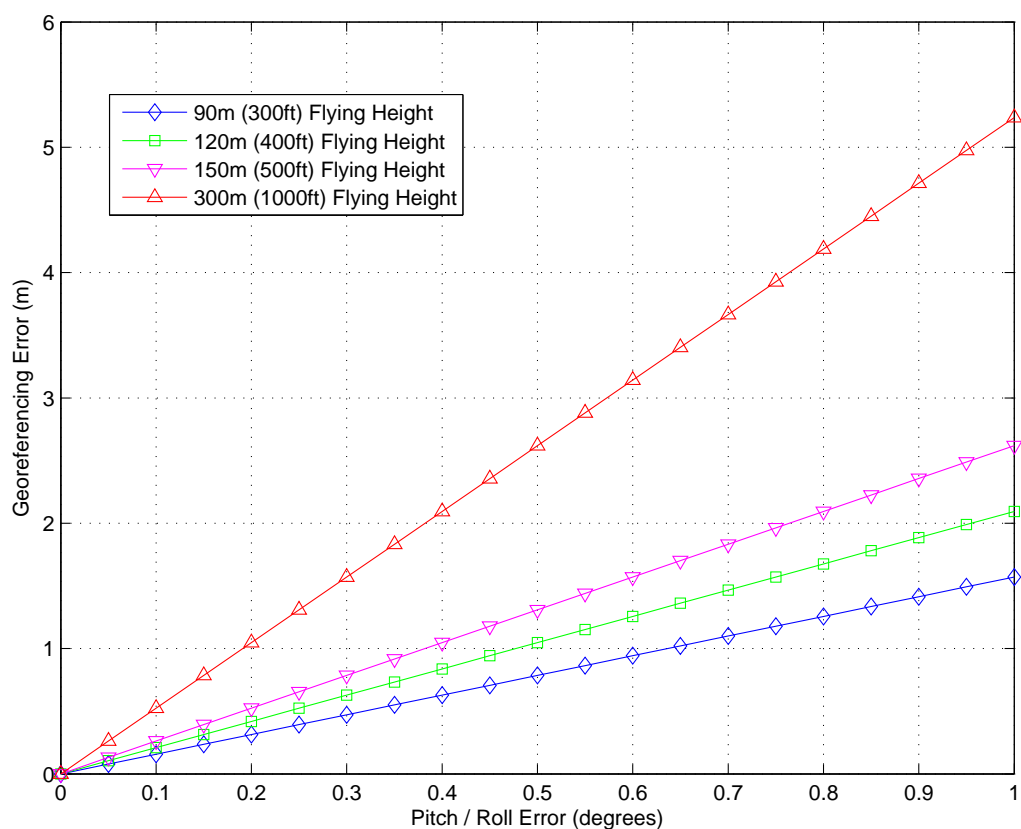


Figure B.7: Representative georeferencing errors for a pitch or roll error.

References

- Akrour, R., B. Santerre, and A. Geiger (2005), Calibrating antenna phase centres - a tale of two methods, *GPS World*, <http://www.gpsworld.com/gpsworld/article/articleDetail.jsp?id=146691>.
- Blewitt, G. (1997), Basics of the GPS technique: observation equations, *Geodetic Applications of GPS*, pp. 10–54.
- Borre, K., D. Akos, N. Bertelsen, P. Rinder, and S. Jensen (2007), *A software-defined GPS and Galileo receiver: a single-frequency approach*, Birkhauser, ISBN 0817643907.
- Bottasso, C., D. Leonello, A. Maffezzoli, and F. Riccardi (2009), A Procedure for the Identification the Inertial Properties of Small Size UAVs., *XX AIDAA Congress, Milano, Italy*.
- Brunner, F., H. Hartinger, and L. Troyer (1999), GPS signal diffraction modelling: the stochastic SIGMA-D model, *Journal of Geodesy*, 73(5), 259–267.
- Calhoun, S. (2006), Six degree-of-freedom modelling of an uninhabited aerial vehicle, Master's thesis, Ohio University, Electrical Engineering.

-
- Cannon, M., and J. Ray (2000), Attitude determination using multipath mitigation on multiple closely spaced antennas, in *ION GPS 2000*, Salt Lake City.
- Cohen, C. (1993), Attitude determination using GPS, Ph.D. thesis, Stanford University.
- Cohen, C., E. Lightsey, W. Feess, and B. Parkinson (1993), Space flight tests of attitude determination using GPS, *ION GPS-93*, pp. 625–632.
- Crossbow (2010), *Crossbow IMU440 Datasheet*, Crossbow Technology Inc., <http://www.xbow.com/>.
- De Jonge, P., and C. Tiberius (1996), The LAMBDA method for integer ambiguity estimation: implementation aspects, *Publications of the Delft Computing Centre, LGR-Series No. 12*.
- Duke, E., R. Antoniewicz, and K. Krambeer (1988), Derivation and Definition of a Linear Aircraft Model, *Reference Publication 1207*, NASA.
- Euler, H. J., and B. Schaffrin (1991), On a measure for the discernibility between different ambiguity solutions in the static-kinematic GPS-mode., *IAG Symposia no.107, Kinematic Systems in Geodesy, Surveying, and Remote Sensing*, Springer-Verlag, New York, p. 285 to 295.
- Evans, J., W. Hodge, J. Liebman, C. Tomlin, and B. Parkinson (1999), Flight Tests of an Unmanned Air Vehicle with Integrated Multi-Antenna GPS Receiver and IMU: Towards a Testbed for Distributed Control and Formation Flight, in *Proceedings of ION GPS 1999*.
- Farrell, J., and M. Barth (1999), *The global positioning system and inertial navigation*, McGraw-Hill Professional, ISBN 007022045X.
- Giorgi, G. (2010), The multivariate constrained LAMBDA method for single-epoch, single-frequency GNSS-based full attitude determination, *Proceedings of ION GNSS 2010*.
- Giorgi, G., and P. Teunissen (2010), Carrier phase GNSS attitude determination with the Multivariate Constrained LAMBDA method, *Proceedings of the IEEE Aerospace Conference*.
- Giorgi, G., P. Teunissen, and P. Buist (2008), A search and shrink approach for the baseline constrained LAMBDA: experimental results, *Proceedings of the International Symposium on GPS/GNSS*, pp. 797–806.

-
- Gursul, I. (2004), Vortex flows on UAVs: Issues and challenges, *Aeronautical Journal*, 108(1090), 597–610.
- Hall, J. K., N. Knoebel, and T. McLain (2008), Quaternion attitude estimation for miniature air vehicles using a multiplicative extended kalman filter, in *IEEE/ION PLANS 2008*.
- Hide, C., and T. Botterill (2010), Development of an integrated IMU, image recognition and orientation sensor for pedestrian navigation, *Proceedings of ION GNSS 2010*.
- Hide, C., T. Moore, and M. Smith (2004), Multiple Model Kalman Filtering for GPS and Low-cost INS integration, *Proceedings of ION GNSS 2004*, pp. 21–24.
- Hide, C., J. Pinchin, and D. Park (2007), Development of a low cost multiple GPS antenna attitude system, *Proceedings of ION GNSS 2007*.
- Hofmann-Wellenhof, B., H. Lichtenegger, and J. Collins (2001), *GPS Theory and Practice*, Springer-Verlag, ISBN 3211008284.
- Hofmann-Wellenhof, B., K. Legat, and M. Wieser (2003), *Navigation: Principles of Positioning and Guidance*, 1st ed., Springer, ISBN 3211008284.
- Isaacs, A. (Ed.) (2000), *Oxford Dictionary of Physics*, Oxford University Press, ISBN 0192801031.
- Jardin, M., and E. Mueller (2007), Optimized measurements of UAV mass moment of inertia with a bifilar pendulum, *AIAA Guidance, Navigation and Control Conference and Exhibit, Hilton Head, SC, USA*.
- JPO, G. (2000), Interface control document ICD-GPS-200, revision IRN-200C-004, *Tech. rep.*, GPS Joint Programs Office.
- Kannemans, H. (2005), Static and dynamic GNSS attitude function testing of airborne equipment, *Tech. Rep. NLR-TP-2005-230*, National Aerospace Laboratory NLR.
- Kaplan, E., and C. Hegarty (2006), *Understanding GPS: Principles and Applications*, 2nd ed., Artech House Publishers, ISBN 1580538940.

-
- Kasser, M., and Y. Egels (2002), *Digital photogrammetry*, CRC, ISBN 0748409459.
- Keong, J. (2001), Determining Heading and Pitch Using a Single Difference GPS/GLONASS Approach, Ph.D. thesis, Department of Geomatics Engineering, University of Calgary.
- Kim, D., and R. Langley (2003), Instantaneous real-time cycle-slip correction for quality control of GPS carrier-phase measurements, *Navigation*, 49(4), 205–222.
- Langley, R. (1997), GPS Receiver System Noise, *GPS World*, 8(6), 40–45.
- Lee, G., C. Park, H. Lee, S. Son, D. Hwang, and S. Lee (2004), UAV flight test of GPS attitude determination system, in *GNSS 2004*, Sydney, Australia.
- Lievens, K., J. Mulder, and P. Chu (2005), Single GPS antenna attitude determination of a fixed wing aircraft aided with aircraft aerodynamics, *2005 AIAA Guidance, Navigation, and Control Conference and Exhibit*, pp. 1–14.
- Lightsey, E., and J. Madsen (2003), Three-axis attitude determination using global positioning system signal strength measurements, *Journal of Guidance, Control, and Dynamics*, 26, 304–310.
- Lovren, N., and J. Pieper (1998), Error analysis of direction cosines and quaternion parameters techniques for aircraft attitude determination, *Aerospace and Electronic Systems, IEEE Transactions on*, 34(3), 983–989.
- Lu, G. (1995), Development of a GPS Multi-antenna System for Attitude Determination, Ph.D. thesis, Department of Geomatics Engineering, University of Calgary.
- Lu, G., M. Cannon, G. Lachapelle, and P. Kielland (1993), Attitude Determination in a Survey Launch Using Multi-Antenna GPS Technologies, in *Proceedings of National Technical Meeting*, pp. 251–260, The Institute of Navigation, Alexandria, VA.
- Meerbergen, K., and F. Tisseur (2001), The quadratic eigenvalue problem, *SIAM Review*, 43, 235–286.
- Misra, P., and P. Enge (2006), *Global Positioning System: Signals, Measurements and Performance*, 2nd ed., Lincoln, MA: Ganga-Jamuna Press, ISBN 0970954417.

-
- Monikes, R., J. Wendel, and G. Trommer (2005), A modified LAMBDA method for ambiguity resolution in the presence of position domain constraints, *Prococeedings of ION GNSS 2005*.
- Mostafa, M., and K. Schwarz (2001), Digital image georeferencing from a multiple camera system by GPS/INS, *ISPRS Journal of Photogrammetry and Remote Sensing*, 56(1), 1–12.
- Onshine (2007), *ANT-555 GPS Active Antenna*, Onshine Enterprise Co. Ltd., <http://www.onshine.com.tw/>.
- Ou, Q., X. Chen, D. Park, A. Marburg, and J. Pinchin (2008), Integrated Flight Dynamics Modelling for Unmanned Aerial Vehicles, *IEEE/ASME International Conference on Mechtronic and Embedded Systems and Applications*, pp. 570–575.
- Ozludemir, M. (2004), The Stochastic Modeling of GPS Observations, *Turkish J. Eng. Env. Sci*, 28, 223–231.
- Park, S., and C. Kee (2006), Enhanced method for single-antenna GPS-based attitude determination, *Aircraft Engineering and Aerospace Technology: An International Journal*, 78(3), 236–243.
- Parkinson, B., and J. Spilker (1996), *The global positioning system: theory and applications*, AIAA, ISBN 1563471078.
- Phillips, W., C. Hailey, and G. Gebert (2001), Review of attitude representations used for aircraft kinematics, *Journal of Aircraft*, 38(4), 718–737.
- Pinchin, J. (2008), Enhanced Integer Bootstrapping for Single Frequency GPS Attitude Determination, *Proceedings of ION GNSS 2008*.
- Pinchin, J., C. Hide, D. Park, and X. Chen (2008), Precise kinematic positioning using single frequency GPS receivers and an integer ambiguity constraint, *Position, Location and Navigation Symposium, 2008 IEEE/ION*, pp. 600–605.
- Rothacher, M., T. Springer, S. Schaer, and G. Beutler (1998), Processing strategies for regional GPS networks, *Advances in positioning and reference frames: IAG Scientific Assembly, Rio de Janeiro, Brazil, September 3-9, 1997*, p. 93.

-
- Salman, S., A. Sreenatha, and J. Choi (2006), Attitude dynamics identification of unmanned aircraft vehicle, *International Journal of Control, Automation, and Systems*, 4 no.6, 782–787.
- Schleppe, J. (1997), Development of a real-time attitude system using a quaternion parameterization and non-dedicated GPS receivers., Ph.D. thesis, Department of Geomatics Engineering, University of Calgary.
- Spinney, V. (1976), Application of the Global Positioning System as an attitude reference for near-earth users, *New frontiers in aerospace navigation*, pp. 132–136.
- Stevens, B., and F. Lewis (1992), *Aircraft Control and Simulation*, Wiley, ISBN 0471613975.
- Teal (2010), 2010 world UAV market profile and forecast, *Tech. rep.*, Teal Group, <http://www.tealgroup.com/>.
- Teunissen, P. (1993), Least-squares estimation of the integer GPS ambiguities, *Invited lecture, Section IV theory and methodology, IAG general meeting, Beijing, China, August*.
- Teunissen, P. (1995), The least-squares ambiguity decorrelation adjustment: a method for fast GPS integer ambiguity estimation, *Journal of Geodesy*, 70(1), 65–82.
- Teunissen, P. (1998), Success probability of integer GPS ambiguity rounding and bootstrapping, *Journal of Geodesy*, 72(10), 606–612.
- Teunissen, P. (1999), An optimality property of the integer least-squares estimator, *Journal of Geodesy*, 73(11), 587–593.
- Teunissen, P. (2000), *Adjustment theory: an introduction*, Delft Univ. Press, ISBN 9040719748.
- Teunissen, P. (2002), Integer least-squares, *Proc. V Hotine-Marussi Symposium on Mathematical Geodesy, Matera, Italy*.
- Teunissen, P. (2006), The Lambda Method for the GNSS Compass, *Artificial Satellites*, 41(3), 89–103.
- Teunissen, P., and S. Verhagen (2004), On the foundation of the popular ratio test for GNSS ambiguity resolution, *ION GNSS 2004, Long Beach, California*, pp. 2529–2540.

-
- Teunissen, P., P. de Jonge, and C. Tiberius (1996), Volume of the GPS ambiguity search space and its relevance for integer ambiguity resolution, in *ION GPS 1996*, pp. 889–898.
- u-blox AG (2009), *LEA-5T Datasheet, u-blox 5 GPS receiver with Precision Timing*, u-Blox, <http://www.u-blox.com/en/lea-5t.html>.
- USDoD (2005), Unmanned aircraft systems roadmap 2005-2030, www.fas.org/irp/program/collect/uav_roadmap2005.pdf.
- Vaniček, P., and R. Steeves (1996), Transformation of coordinates between two horizontal geodetic datums, *Journal of Geodesy*, 70(11), 740–745.
- Verhagen, S. (2004), Integer ambiguity validation: an open problem?, *GPS Solutions*, 8(1), 36–43.
- Wieser, A. (2007), How important is GNSS observation weighting, *Inside GNSS*, 2(1), 26–28.
- Wieser, A., H. Hartinger, and M. Gaggl (2005), Improved positioning accuracy with high-sensitivity GNSS receivers and SNR aided integrity monitoring of pseudo-range observations, *Proc. ION GNSS*, pp. 13–16.